THE MICROWAVE OPACITY OF AMMONIA AND WATER VAPOR: APPLICATION TO REMOTE SENSING OF THE ATMOSPHERE OF JUPITER

A Dissertation
Presented to
The Academic Faculty

By

Thomas Ryan Hanley

In Partial Fulfillment
of the Requirements for the Degree
Doctor of Philosophy in
Electrical and Computer Engineering

Georgia Institute of Technology

August 2008

THE MICROWAVE OPACITY OF AMMONIA AND WATER VAPOR: APPLICATION TO REMOTE SENSING OF THE ATMOSPHERE OF JUPITER

Approved By

Dr. Paul G. Steffes
School of Electrical and Computer Engineering
Georgia Institute of Technology

Dr. Thomas K. Gaylord
School of Electrical and Computer Engineering
Georgia Institute of Technology

Dr. Gregory D. Durgin
School of Electrical and Computer Engineering
Georgia Institute of Technology

Dr. Robert D. Braun
Guggenheim School of Aerospace Engineering
Georgia Institute of Technology

Dr. Waymond R. Scott
School of Electrical and Computer Engineering
Georgia Institute of Technology

Date Approved: June 18, 2008

To Grandpa

ACKNOWLEDGEMENTS

This thesis is the culmination of the last five years of late nights and long hours in the lab. It would not have been possible without the guidance and support of several people to whom I am deeply indebted. I would like to first thank my advisor, Dr. Paul G. Steffes, whose vast knowledge of the fields of microwave spectroscopy and planetary remote sensing, endless patience, and ability to obtain the support of sponsors allowed me to make the strides necessary to complete this work. Despite us working seemingly different shifts, he never doubted I was making progress even though he did not always see me in the lab. I would also like to thank the members of my dissertation committee for their time and effort in thoughtfully reviewing this work: Drs. G. D. Durgin, W. R. Scott, T. K. Gaylord and R. D. Braun.

I owe a multitude of thanks to my future wife Casey Korecki whose love, friendship and understanding kept me going throughout all my graduate work. The knowledge that we would be united after completing our degrees in separate parts of the country helped keep me on schedule. I am also forever indebted to my parents, Dennis and Peggy Hanley, who not only supported me financially, but never stopped believing in me and encouraging me to do my best. I thank my late maternal grandfather, Jerome Gruber, whose tutelage in my early years undoubtedly solidified my decision to study engineering. He taught me to always look for the best, most efficient way to do something and that almost anything broken can be fixed. I thank my brother Jim and sister Kerry and all my friends and family who never lost touch with me throughout my time away at school.

I would also like to thank my past and present companions of the Planetary Atmospheres Lab who were great sources of knowledge, conversation, and encouragement: Dr. Priscilla Mohammed, Dr. Allen Petrin, Dr. William Barott, Bryan Karpowicz and Kiruthika Devaraj. Thanks also to my fellow officers and members of Eta Kappa Nu who provided me with activities outside of research and plenty of free meals. Thanks to all the staff of the Georgia Tech School of Electrical and Computer Engineering, especially Sharon Fennell, who keep the department operational.

Lastly, thanks to the NASA Planetary Atmospheres Program and the NASA Juno Mission, especially Principal Investigator Dr. Scott Bolton and the entire MWR Science Team, for their financial support of this work. This work was supported by NASA Contract NNM06AA75C from the Marshall Space Flight Center supporting the Juno Mission Science Team, under Subcontract 699054X from the Southwest Research Institute and by the NASA Planetary Atmospheres Program under Grant NNG06GF34G .

TABLE OF CONTENTS

LIST OF TABLES

LIST OF FIGURES

SUMMARY

The object of this research program has been to provide a baseline for microwave remote sensing of ammonia and water vapor in the atmosphere of Jupiter through laboratory measurements of their microwave absorption properties. Jupiter is not only the largest planet in our solar system, but one of the most interesting and complex. Despite a handful of spacecraft missions and many astronomical measurements, much of Jupiter's atmospheric dynamics and composition remain a mystery. Although constraints have been formed on the amount of certain gases present, the global abundances and distributions of water vapor (H_2O) and ammonia (NH_3) are relatively unknown. Measurements of H_2O and NH_3 in the Jovian atmosphere to hundreds of bars of pressure are best accomplished via passive microwave emission measurements. For these measurements to be accurately interpreted, however, the hydrogen and helium pressure-broadened microwave opacities of H_2O and NH_3 must be well characterized, a task that is very difficult if based solely on theory and limited laboratory measurements. Therefore, accurate laboratory measurements have been taken under a broad range of conditions that mimic those of the Jovian atmosphere. These measurements, performed using a newly redesigned high-accuracy system, and the corresponding models of microwave opacity that have been developed from them comprise the majority of this work. The models allow more accurate retrievals of H_2O and NH_3 abundances from previous as well as future missions to Jupiter and the outer planets, such as the NASA New Frontiers class Juno mission scheduled for launch in 2011. This information will enable a greater understanding of the concentration and distribution of H_2O and NH_3 in the Jovian atmosphere, which will reveal much about how Jupiter and our solar system formed and

how similar planets could form in other solar systems, even planets that may be hospitable to life.

CHAPTER 1: INTRODUCTION

1.1 Background and Research Objectives

When studying the celestial bodies of the universe, researchers most often ask two questions: “What is their composition?” and “What are the processes governing their behavior?” Answering these questions provides additional information as to the past, present and future state of the universe and that of our own solar system and planet Earth.

The solar system is comprised of the sun, eight planets and their moons, and smaller solar orbiting bodies such as dwarf planets, asteroids and comets. Planets can be further divided into two groups, terrestrial planets and gas giants. Mercury, Venus, Earth and Mars, the four planets closest to the sun, are known as terrestrial, leaving the outer planets of Jupiter, Saturn, Uranus and Neptune as the gas giants. The gas giants are aptly named, because unlike the terrestrial planets, they do not have a surface. Rather, the gas giants are conglomerations of gases, held together by gravity, that become denser approaching the center of the planet. The gas giants, like the sun and the majority of the universe, consist of mostly hydrogen and helium. Heavier elements such as carbon and oxygen are formed throughout the universe by the fusion of helium nuclei in the cores of giant stars. Further fusion processes produce more massive atoms such as sulfur, silicon, iron, and other metals. These materials account for the majority of the masses of the terrestrial planets.

The large disparity between the composition of the terrestrial planets and the gas giants has led to numerous theories for the formation of the solar system. Most theories assume some form of the nebular hypothesis whereby the solar system formed from the collapse of a large cloud of matter roughly 4.6 billion years ago. This gravitational

collapse forced most of the matter to form the sun with the remainder lying in a spinning protoplanetary disk. Eventually, many of the particles in the disk coalesced locally due to collisions and gravity, forming planetesimals and eventually planets in a process known as accretion. The terrestrial planets received too much heat and radiation from the sun for molecules such as ammonia and methane to condense and the lighter hydrogen and helium were stripped away by the solar wind. The gas giants, on the other hand, were able to accumulate hydrogen and helium along with oxygen in the form of water (H_2O), carbon in the form of methane (CH_4), nitrogen in the form of ammonia (NH_3) and various other molecules. The order in which the planets formed, the time scales of the accretion, and their location relative to the sun all resulted in variations in the amount of these "volatiles" that exist in the outer planets. If the planetesimals formed at a higher temperature, they would be less likely to trap noble gases and molecules with very low melting points. If, however, they formed at colder temperatures, before the fusion furnace of the sun was fully ignited or at a distance far from the sun, their concentrations would mirror that of the sun.

A more unconventional hypothesis known as the capture theory, first proposed by Woolfson (1960), suggests that a large body 100 times more massive than the sun passed by the sun within ten solar radii. This caused gravitational tides that pulled material out of the molten sun in waves, which then formed the planets. This would suggest that the outer planets, which are less affected by the solar wind, should have molecular compositions identical to that of the sun.

To test these and other theories the compositions of the planets need to be measured, a task that is quite difficult given their distance from Earth. Additionally, the

processes that transport molecules throughout the atmospheres and cores of the planets must be understood to explain localized variations in molecular concentration. Jupiter is a perfect candidate for mapping the evolution of our solar system since its large gravity and strong magnetosphere have allowed it to maintain most of its original composition. Additionally, dozens of Jupiter-like exoplanets (planets orbiting other stars) have been located in the past 13 years (Butler *et al.* 2006). By studying Jupiter and its formation, much can be learned about the formation of not only our own solar system, but other planetary systems, many of which could contain planets hospitable to life.

Jupiter accounts for roughly 70% of the planetary mass of our solar system, about 318 times as much as Earth. Apart from hydrogen and helium, other major constituents detected at Jupiter include methane (CH_4) and lesser amounts of various other hydrocarbons, water vapor (H_2O), ammonia (NH_3), hydrogen sulfide (H_2S), and phosphine (PH_3) along with the noble gases neon (Ne), argon (Ar), krypton (Kr), and xenon (Xe) (Kunde *et al.* 1982; Niemann *et al.* 1996). To study Jupiter, researchers employ a variety of remote sensing techniques and even some limited *in situ* space probe measurements. These techniques, however, require accurate knowledge of the spectral properties of the molecular species being studied. One species of particular interest is water. Not only is water an essential component of habitable planets, but it can also be found in all three phases (solid, liquid and gas/vapor) throughout the solar system. In the case of Jupiter, the pressures and temperatures in its deeper atmosphere favor the presence of water vapor. As will be explained in Chapter 2, the spectrum of ammonia at Jupiter can obscure the spectrum of water vapor. Measuring water vapor in Jupiter's deep atmosphere is a very difficult task unless the properties of both H_2O and NH_3 are

well understood. To better measure these properties, a high-accuracy laboratory system and experimental protocol have been developed. Completed measurements of H_2O and NH_3 along with numerical models that predict their behavior under a wide range of conditions will be described in depth herein. These models represent a key component necessary to processing the data from Earth-based and spacecraft-based studies that will provide a greater physical understanding of the universe we inhabit.

1.2 Organization

This dissertation is comprised of essentially four main areas: theoretical discussion of the microwave absorbing properties of ammonia and water vapor, experimental measurements of the microwave properties of ammonia and water vapor under Jovian conditions, development of empirically derived models for NH_3 and H_2O opacity under Jovian conditions, and application of these models to past and hypothetical future spacecraft data from Jupiter. Each of these topics is discussed within its own chapter.

In Chapter 2 a cursory description of various remote sensing techniques is presented along with a more in-depth description of the NASA Juno mission. The theory regarding absorption of microwave energy by molecules is also discussed in addition to previous measurements and models from other researchers in the case of NH_3 and H_2O.

Chapter 3 begins with a discussion of the theory behind measuring the absorption and refraction of gases in the microwave regime. From there, the specifics of the measurement system used for this work are presented. Lastly, a description of the procedure leads into the method of processing the raw data and the uncertainties involved.

Chapter 4 describes the method of fitting models to the data and presents the results of the new model for ammonia opacity compared to the previous state of the art. The experimental configurations and measurement limitations are discussed. Chapter 5 shows the usage of the new NH_3 model in reprocessing the data from the Galileo Entry Probe radio signal absorption measurements. The new results are compared and contrasted to the previous ones. The current and previous models are also compared in the context of hypothetical retrievals from the Juno mission via radiative transfer modeling. The effect of the rotational spectrum of ammonia on its properties at microwaves is also discussed.

Chapter 6 summarizes the findings of this work and presents suggestions for future work. The contributions of this author to the field of laboratory measurements of the microwave properties of NH_3 and H_2O are subsequently listed and a list of publications is included.

CHAPTER 2: MICROWAVE REMOTE SENSING TECHNIQUES AND THEORY

The most familiar astronomical remote sensing technique involves viewing planets through optical telescopes. While this can provide insight to some of a planet's atmospheric dynamics, it is not very effective in determining composition as many molecules do not have strong absorption bands in the optical region of the electromagnetic spectrum. The ultraviolet (UV) and infrared (IR) bands contain many absorption features unique to each molecule and allow telescopes operating in those regions to more accurately determine planetary composition. However, the opacity from these absorption bands also limits the depths to which these methods can sense. This is especially an issue in the dense, clouded atmospheres of the gas giants. To delve deeper, longer wavelength (microwave and radio wave) emissions must be measured.

Microwave remote sensing measurements can be performed in a variety of ways. Active sensing requires both a transmitter and receiver and includes such methods as radar, radio occultations and entry probe radio signal absorption measurements. Passive sensing relies on the measurement of background or blackbody radiation coming from a planet using only a receiver, otherwise known as a radiometer. Each method has its advantages and disadvantages as to the spatial resolution, power requirements and the depths to which each can measure. Radars require the reflection of microwave energy and work best for measuring dense, reflective surfaces and larger objects that scatter radiation back to the receiver. While they can provide great spatial resolution, they are not very effective at measuring gases unless those gases are condensed into large cloud particles. In the case of radio occultations (e.g. the Cassini or Voyager missions), a carrier wave signal is transmitted through various altitudes of a planet's atmosphere in

either an uplink or downlink configuration. This transmission occurs between the spacecraft and earth as the spacecraft moves behind the planet and usually involves multiple frequency bands. As the signals pass through the planet's atmosphere, they are gradually bent due to the index of refraction of the gases. For gas giants, the path through the atmosphere eventually becomes too opaque for the signals to be detected as shown in Figure 2.1. This limits the depths that can be measured to only a few bars of pressure. For entry probe radio links (e.g. the Galileo mission) the signal loss through the atmosphere is measured in the radio transmission between an entry probe and a nearby orbiting spacecraft. Unless the entry probe has the ability to maneuver and overcome the gravitational pull of the planet, most entry probe measurements are limited to only one location on the planet. In contrast, passive thermal emission measurements use the planet's blackbody radiation as a full-band transmitter at all locations on the planetary disk.

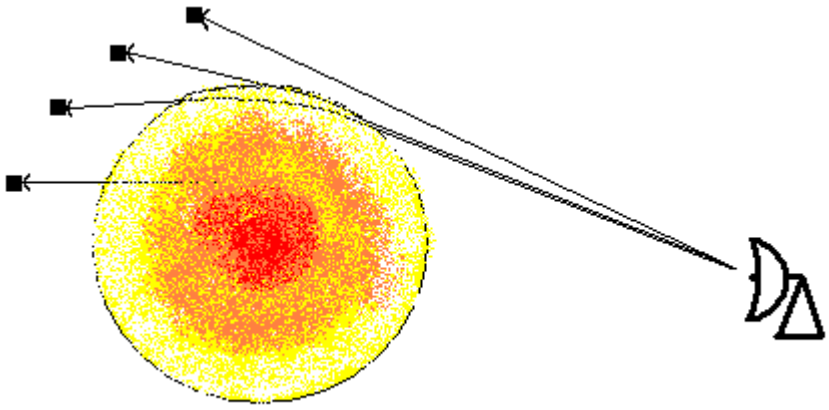

Figure 2.1: Diagram of a radio occultation experiment

After precisely measuring the drop in signal intensity and phase shift (in the case of radio occultation and entry probe experiments) caused by atmospheric attenuation and refraction, researchers can compare the results with the known properties of gases and retrieve temperature-pressure profiles and the abundance of microwave-absorbing constituents. The accuracy of these retrievals not only depends on the measurement abilities of the spacecraft and earth stations, but also on the knowledge of the microwave and millimeter-wave properties of the gases present. Being able to more accurately measure those properties in a laboratory setting allows for more accurate scientific retrievals and knowledge of the composition, function, and formation of our solar system.

Radio emissions (22.2 MHz) from Jupiter were first detected in 1955 (Burke and Franklin 1955). These strong emissions, however, were due primarily to the noisy synchrotron radiation from fields surrounding the planet and not from thermal radiation from the atmosphere itself. The first thermal emission measurements were made during the following two years at a frequency of 9.53 GHz by Mayer *et al*. (1958). The ammonia resonant structure at microwave frequencies in Jupiter's atmosphere was first measured by Law and Staelin (1968) at five frequencies between 19.0 and 25.4 GHz and later by Wrixon *et al*. (1971) at eight frequencies between 20.5 and 35.5 GHz, although Wildt (1932) had detected the presence of ammonia four decades earlier using infrared observations. Water was not detected until much later, and also in the infrared (Larson *et al.* 1975). Since that time numerous other Earth and space-based measurements have been made throughout the microwave and millimeter-wave bands, but the accuracy of the interpretations of them are subject to the knowledge of the microwave absorption coefficients of the constituents found there.

Many of the known Jovian molecular species were detected though data from the Galileo Probe mission's Mass Spectrometer (Niemann *et al.* 1996), which in December of 1995 took *in situ* measurements of Jupiter's atmosphere at one location down to a pressure of 22 bars before the probe disintegrated from the intense temperature and pressure. This one data point is presently the deepest measurement of the Jovian atmosphere, and was deep enough to sense beneath the various cloud layers. Also, sensing *in situ* with a mass spectrometer provided greater accuracy than other remote sensing methods. Unfortunately, the probe entered what is known as a hot spot, the Earth equivalent of a desert, where it detected much less water than was believed to be present "on average" throughout the planet. The Galileo Probe results raised more questions than provided answers, which became one of the motivating factors for the future NASA Juno mission.

2.1 The Juno Mission

The NASA Juno Mission is a solar-powered spin-stabilized robotic spacecraft that is scheduled for launch in 2011. It will make 32 highly elliptical polar orbits around Jupiter studying the dynamics of its atmosphere, radiation belts, gravity field, and magnetosphere. The orbital path has been selected to allow the spacecraft to pass within the planet's strong radiation and synchrotron belts to optimize the sensitivity of its measurements while minimizing the amount of high-energy radiation doses it receives. Juno's Microwave Radiometer instrument or MWR will measure the atmospheric composition beneath the cloud layers, down to hundreds of bars of pressure. MWR is an optimal instrument for Juno since it will measure a wider range of altitudes throughout the Jovian atmosphere than instruments operating at shorter wavelengths and will not be

subject to the interference from the synchrotron radiation that plagues Earth-based measurements.

The MWR will employ six radiometer channels ranging in wavelength from 50 cm (600 MHz) to 1.3 cm (23 GHz) (Janssen *et al.* 2005). The channels will passively measure Jupiter's microwave emission, commonly characterized by brightness temperature, or the physical temperature of a black body producing the equivalent radiation at a particular wavelength. The antennas for the channels will be placed on the side of the spacecraft so that as it rotates, the antennas will scan across the planet along the track of the spacecraft taking brightness temperature measurements of the same location, but at different look angles. This allows for better calibration of the radiometers and lessens the effect of horizontal variations in the atmosphere. These brightness temperature measurements, with the aid of a radiative transfer model, will be able to determine the concentrations of water vapor and ammonia at various depths and locations covering the planet, assuming that the radiative transfer model uses accurate microwave absorption coefficients for H_2O and NH_3.

2.2 Electromagnetic Absorption by Molecules in the Gaseous State

Any gaseous molecule with a temperature above absolute zero has kinetic energy associated with it. This energy, represented by the motions of the molecule, is quantized. A molecule with more than one atom has moments of inertia about the molecule's center of mass that give rise to various rotational states of the molecule. The distances between the bound atoms in a molecule may also vary in an oscillatory pattern known as a vibrational state due to small changes of the attractive and repulsive forces between the negatively charged electrons and positively charged nuclei. Additionally, the electrons in

each atom can inhabit higher ordered orbitals with increased molecular energy. These three states allow many molecules to absorb and emit electromagnetic energy over a wide portion of the spectrum. Since the energy levels of each of the modes in these states are quantized, the frequencies of electromagnetic radiation that a molecule may absorb or emit are limited to those which satisfy

$$\nu_0 = \frac{E_u - E_l}{h} \qquad (2.1)$$

where ν_0 represents the frequency of the transition[1], E_u and E_l represent upper and lower energy states of the molecule and h is Planck's constant. When a molecule absorbs energy it transitions from a lower energy state to a higher one and when it emits energy, the opposite occurs. For changes in electron states, the energies required typically occupy the optical and ultraviolet parts of the spectrum. For vibrational energy transitions the frequencies are most often found in the infrared, whereas rotational transitions can occur anywhere from the terahertz (THz) regime down to microwave frequencies. The frequencies that cause transitions are called absorption lines and each absorption line has a line strength related to the proportion of molecules normally inhabiting the upper and lower states of that transition.

If a molecule has a structure where its atomic bonding has allowed for greater positive charges to accumulate on one side of the molecule and negative charges on the other, that molecule is said to possess a permanent dipole moment. A molecule with a permanent dipole moment is often referred to as polar. A polar molecule is similar to a magnet with its oppositely charged north and south poles. Just like the needle of a

[1] In this chapter, the Greek letter nu (ν) will be used to design frequency, keeping with the context of the cited literature. In subsequent chapters frequency will be designated (f).

compass aligns itself with the magnetic field of the Earth, a polar molecule has a tendency to align itself with the varying electromagnetic fields incident upon it. When these fields oscillate with particular microwave and millimeter-wave frequencies, polar molecules can receive the angular momentum necessary to transition into different rotational modes. Even non-polar molecules can have temporary dipole moments induced from collisions with other polar and non-polar molecules.

2.2.1 Linewidths and Lineshapes

Although the energy and corresponding frequency of a particular molecular energy transition are quantized, they are not limited to precisely one frequency. Frequencies that are close to the transition frequency can be absorbed or emitted by a proportion of the molecules. The range of frequencies about an absorption line that cause transitions in at least half of the molecules of a particular species are referred to as the spectral width of an absorption line. Half of this total width corresponds to the half width at half maximum (*HWHM*) of the absorption line and is known as the linewidth or linebreadth. The spectral shape of the line as a function of frequency is known as the lineshape.

This line-broadening phenomenon has several causes, each of which take precedence under different conditions. Zero-point ambient electromagnetic radiation, present everywhere in space, causes absorption lines to have a "natural breadth" (Townes and Schawlow 1955). While this effect is noticeable for electronic transitions, its effect at microwaves is much less than 1 Hz. This effect can also be prevented in an experimental setting, such as a resonator where only certain frequencies modes are excited. Additionally, collisions with the walls of a test cell in a laboratory setting can cause line broadening. While this effect must be considered when using small waveguide

absorption cells (Johnson and Strandberg 1952), it is negligible for the relatively large resonators used in this work.

The motion of a molecule relative to applied electromagnetic radiation causes the frequency encountered by the molecule to shift according to the Doppler effect. This effect, known as Doppler broadening, creates a linewidth that varies as

$$\Delta\nu_{Doppler} = 3.581\times10^{-7}\nu\sqrt{\frac{T}{M}} \qquad (2.2)$$

where ν is the center frequency of the line, T is the temperature of the gas in Kelvin and M is its molecular mass (Townes and Schawlow 1955). In very low density gas mixtures, Doppler broadening is considerable, however, for the temperatures and pressures at Jupiter studied in this work, its effect is negligible.

For most planetary conditions, including those at Jupiter sensed by the Juno mission, the greatest source of line broadening results from molecular collisions. These collisions allow for the transfer of kinetic energy and interactions between the molecules due to van der Waals forces. Commonly referred to as pressure broadening, this process is very difficult to accurately characterize.

Lorentz (1906) was the first to attempt to model the pressure broadening of gases, with his work focusing on optical wavelengths. His work gave rise to a spectral line shape still in widespread use today known as the Lorentz lineshape (Lorentz 1915), presented by Van Vleck and Weisskopf (1945) as

$$F_L(\nu_{ij},\nu) = \frac{1}{\pi}\left[\frac{\Delta\nu}{(\nu_{ij}-\nu)^2+\Delta\nu^2} - \frac{\Delta\nu}{(\nu_{ij}+\nu)^2+\Delta\nu^2}\right], \qquad (2.3)$$

where $\Delta\nu$ is the linewidth at half-maximum, ν_{ij} is the frequency of the transition between states i and j, and ν is the frequency of the incident electromagnetic wave. The linewidth

can also be written as $\Delta\nu=1/(2\pi\tau)$ where τ is the mean time between collisions. Debye (1929) described the absorption and refraction in polar molecules with a theory that did not agree with the Lorentz shape at zero resonant frequency. This led to the work of Van Vleck and Weisskopf (1945), who combined the theories of Lorentz and Debye to derive the Van Vleck-Weisskopf lineshape:

$$F_{VVW}(\nu_{ij},\nu)=\frac{1}{\pi}\frac{\nu}{\nu_{ij}}\left[\frac{\Delta\nu}{(\nu_{ij}-\nu)^2+\Delta\nu^2}+\frac{\Delta\nu}{(\nu_{ij}+\nu)^2+\Delta\nu^2}\right], \qquad (2.4)$$

which was later verified by Fröhlich (1946). Gross (1955) assumed a Maxwellian distribution of molecular velocities, instead of the Boltzmann one used by Lorentz and Van Vleck and Weisskopf, which gave a lineshape of

$$F_G(\nu_{ij},\nu)=\frac{1}{\pi}\left[\frac{4\nu\nu_{ij}\Delta\nu}{\left(\nu_{ij}^2-\nu^2\right)^2+4\nu^2\Delta\nu^2}\right]. \qquad (2.5)$$

Both the Van Vleck-Weisskopf and Gross lineshapes converge at the line centers. Neither of these lineshapes, however, was able to match the microwave spectral data of ammonia measured by Bleaney and Loubser (1950). Therefore, Ben-Reuven (1966) derived a lineshape that included two additional factors, a line shift parameter (δ) proportional to gas density and a line-to-line coupling element (ζ). The Ben-Reuven lineshape takes the form:

$$F_{BR}=\frac{2}{\pi}\left(\frac{\nu}{\nu_0}\right)\frac{(\gamma-\zeta)\nu^2+(\gamma+\zeta)\left[(\nu_0+\delta)^2+\gamma^2-\zeta^2\right]}{\left[\nu^2-(\nu_0+\delta)^2-\gamma^2+\zeta^2\right]^2+4\nu^2\gamma^2}, \qquad (2.6)$$

where Ben-Reuven uses γ to represent the linewidth instead of $\Delta\nu$.

All of these lineshapes rely on the knowledge of the linewidth of the gas being studied. The most common approach to modeling linewidths of a gas species involves a

statistical approach, whereby all the possible states of the molecule are considered. These states are weighted by their populations (the percentage of the molecules of the species that occupy that state), which are directly proportional to the inverse exponential of their energy level. Collisions between two molecules can assume a number of possible outcomes due to the probability of each molecule being in a particular state, the velocities of the molecules relative to each other, and the duration of the collision. A collision does not necessarily refer to direct physical contact between the molecules, but implies that the molecules were proximate enough to affect each other's motion. This is especially true for molecules with strong dipoles that can influence other molecules many molecular radii away. Almost every pressure-broadening theory assumes only binary collisions, or collisions involving only two molecules at once. Most also assume that the duration of the collisions is short relative to the frequency of collisions. Both of these assumptions are adequate for air pressures found on Earth, but are invalid for the high-pressure environments of the outer planets. Also, no one theory has been shown to accurately characterize the measured behavior of ammonia or water vapor at microwaves over a wide range of conditions and energy states. Since these pressure-broadening theories have little applicability to the Jovian conditions presented in this work, the discussion of them will be limited to the few instances where they provide insight into the behaviors of the gases studied here. For more through discussions of pressure broadening, see, e.g., Anderson (1949) and (1950), Baranger (1958), Birnbaum (1966), Fano (1981), Herbauts and Dunstan (2007), Margenau (1951), McMahon and McLaughlin (1974), Mizushima (1951), Murphy and Boggs (1967), Tsao and Curnutte (1962) and VanVleck and Margenau (1949).

2.2.2 Theoretical Microwave Absorption by Ammonia

Ammonia is a symmetric top molecule and has a pyramidal form with a nitrogen atom at the apex and three hydrogen atoms at the base as shown in Figure 2.2. The hydrogen atoms are bonded to the nitrogen atom leaving one unbonded pair of electrons atop the nitrogen atom. These negatively charged electrons and those shared by the hydrogen atoms combined with the positively charged protons in the hydrogen nuclei create a dipole, the strength of which depends on the molecule's temperature (Debye 1929). This dipole makes ammonia much more susceptible to absorbing electromagnetic radiation.

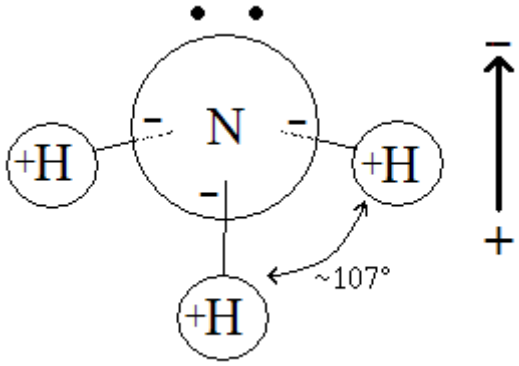

Figure 2.2: Schematic diagram of an ammonia molecule showing the orientation of the dipole and the H-N-H bond angle. The two black dots atop the nitrogen atom represent unbonded electrons.

Like many molecules, ammonia has a number of rotational and vibrational absorption lines in the terahertz and infrared bands. These lines represent wavelengths of the appropriate quantized energy to induce modes of vibration in the lengths of the N-H bonds and rotation in any direction about the molecule's center of mass. Additionally, special modes of vibration exist where the nitrogen atom tunnels through the potential

barrier of the dipole and oscillates through the plane of the hydrogen atoms, essentially turning itself inside-out. This is referred to as inversion and the frequencies corresponding to the energy levels at which it occurs are throughout the microwave region.

Due to the symmetry of the ammonia molecule, two quantum numbers are commonly used to describe the rotation of the molecule. The first number, *J*, represents the total angular momentum vector of the molecule, extending from the center of mass of the molecule normal to the plane of rotation and the second, *K*, is the projection of *J* onto the axis of symmetry that passes from the center of the nitrogen atom through the point of equidistance in the hydrogen plane. Each rotational state has two split energy levels (Dennison and Uhlenbeck 1932) corresponding to different spins of the nitrogen nucleus that are recognized through molecular inversion, giving rise to a third quantum number S that can have a value of either 1 or 0. The difference in the energy levels of these states corresponds to the electromagnetic energy necessary to cause inversion. Therefore it is common to refer to a particular inversion by the two quantum numbers *J* and *K* of the corresponding rotation, with the state transition S occurring from a 1 to a 0 state. Since *K* is a vector projection and one of the components of *J*, it can never be greater than *J*, and due to the symmetry of the coordinate system negative values are not used. Also, because energy is quantized, *J* and *K* must have integer values. Due to the uncertainty principle, it is not possible to have a molecule with zero angular momentum, therefore *J* cannot be equal to zero. In the pure rotational state, however, *K* can have a zero value, but this state does not have a corresponding inversion. Hence when considering inversion modes, ammonia's quantum numbers count up from 1 with $J \geq K$ and the

inversion modes are usually represented as (J,K). The (1,1) inversion occurs at 23.6945 GHz, however the strongest inversion is the (3,3) transition at 23.8701 GHz (Poynter and Kakar 1975). A more complete description of the theoretical quantum mechanical structure of ammonia and its spectrum can be found in Townes and Schawlow (1955).

Unlike excitation of electrons into higher energy states as in semiconductors, when an ammonia molecule absorbs microwave energy it develops rotational and vibrational motion that is transferred to other molecules and is eventually thermally dissipated. Therefore energy absorbed at one particular frequency is not directly reemitted at the same frequency, so this effect can be considered true absorption.

The coupling of each inversion frequency to a rotational mode can be considered in a classical sense. If the molecule is close to rotating around its axis of symmetry, the molecule resembles a planar configuration due to centrifugal force, which spreads the hydrogen atoms apart, increasing the H-N-H bond angle, thus making inversion easier and more frequent. This corresponds to the case when $J = K$. If the opposite is true and J is much greater than K, the molecule becomes elongated, moving the nitrogen atom farther from the plane of the hydrogen atoms, causing inversion to occur less frequently as more energy is required.

Apart from the frequencies of ammonia's inversion lines, the shapes of the lines have a major effect on its absorption spectrum and one that can be difficult to constrain over a wide range of conditions. The lineshapes vary with the linewidth of each individual NH_3 absorption line. Additionally, collisions of an ammonia molecule with other gas molecules cause slight distortions in the structure of the molecule, induce shifts in the center frequencies of the individual absorption lines, and cause them to broaden.

Each molecular species has a different broadening cross-section based primarily on its size and polarity that characterizes how frequently it collides with other molecules of a given cross-section. These broadening cross-sections are critical in calculating the effect various gases, at their respective number densities, have on each other's microwave absorption. If the pressure of any mixture containing ammonia is greater than a few tens of mbar, its individual absorption lines begin to merge into a single line feature that extends from 1 to 50 GHz. Broadening from one molecule colliding with another of the same species is known as self-broadening, whereas broadening from two different species of gas molecules colliding is known as foreign-gas-broadening. This occurs even when the foreign gases themselves have no microwave absorption lines, as in the case of hydrogen and helium.

While having a strong dipole makes ammonia a good microwave absorber, it also makes ammonia very susceptible to adsorption to instrumental surfaces. This requires extra considerations when attempting to measure ammonia in a laboratory setting. A more thorough discussion of the process of adsorption is presented in Appendix A. Even the accuracy of the retrieval of the *in situ* abundance of NH_3 from the Galileo mass spectrometer was compromised by adsorption to instrumental surfaces (Atreya *et al.* 2003).

2.2.3 Theoretical Microwave Absorption by Water Vapor

The water molecule consists of an oxygen atom bonded to two hydrogen atoms in a bent, triangular formation, also known as an asymmetric-top molecule as shown in Figure 2.3. This results in three independent principal moments of inertia. The structure of a water

molecule can be thought of as a tetrahedron with the oxygen nucleus at the center, the two hydrogen nuclei at two of the vertices, and two pairs of valence electrons from the oxygen atom occupying the other two vertices. This is not completely accurate, however, as the valence electrons have a greater repulsion force since they are not shared with the hydrogen atoms. This results in the unbonded electron pairs repelling the two bonded hydrogen atoms so that the bond angle is approximately 105° rather than the 109.5° that would result from an ideal tetrahedral configuration. This gives water an even greater dipole moment than ammonia, which makes it a good absorber of electromagnetic energy.

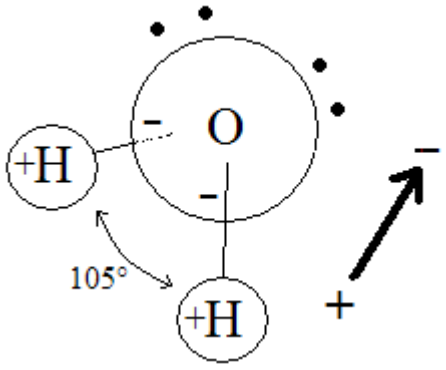

Figure 2.3: Schematic diagram of a water molecule showing the orientation of the dipole and the H-O-H bond angle. The two sets of black dots atop the oxygen atom represent unbonded electrons.

Like ammonia, water's total angular momentum is represented by a quantum number, J. However, because water does not have an axis of symmetry, the projection onto K has no meaning. Therefore it is common to assign two new quantum numbers K_{-1} and K_1 that represent the axes of rotation that give rise to the greatest prolate and oblate deformations, respectively, of the molecule and to project J onto those axes. Rotation about the prolate axis makes the H-O-H bond angle decrease, whereas rotation about the

oblate axis makes the bond angle increase. These rotational modes are usually written as J_{K_{-1},K_1}, but can also be written as J_τ, where $\tau = K_{-1} - K_1$. Unlike NH_3, H_2O does not undergo inversion and therefore has a very limited number of absorption lines in the microwave region, with the lowest measured frequency being the rotational transition between $5_{2,3}$ and $6_{1,6}$ at 22.235 GHz. Other transitions do occur at lower frequencies, such as $21_{7,15} \rightarrow 22_{4,18}$ at 8.2745 GHz and the $16_{4,12} \rightarrow 15_{7,9}$ at 12.48 GHz, but these states have such high energies that they are statistically rare and are only known based on extension of an equation fit to lower energy state data (Pickett *et al.* 2005). Other more commonly found transitions occur at 183.3, 325.2 and 380.2 GHz. Since these lines are relatively widely spaced and not as strong, water vapor has significantly less opacity than ammonia at frequencies below 50 GHz.

The strong polarity of the water molecule makes it a good candidate for adsorption, but its lack of an axis of symmetry makes the bonding geometry more complicated. Of greatest concern when trying to measure water vapor in a laboratory setting is condensation occurring due to temperature gradients, especially in experiments performed at room temperature or nearer the triple point of 273.15 K.

2.2.4 Microwave Absorption from Other Major Jovian Constituents

While ammonia and water vapor contribute the most to microwave absorption in the Jovian atmosphere, there are some other microwave-absorbing components present. Hydrogen sulfide (H_2S) and phosphine (PH_3) have similar atomic structures to water and ammonia respectively although with lesser dipole moments. Sulfur and phosphorus, both being larger, heavier molecules are less common in our solar system than oxygen and nitrogen. The solar compositions of sulfur and phosphorus are 25.895 ppm and 429.75

ppb respectively, compared to 857.4 ppm for oxygen and 113.04 for nitrogen (Grevesse *et al.* 2005). The hydrogen and helium broadened opacities of phosphine (Hoffman *et al.* 2001) and hydrogen sulfide (DeBoer and Steffes 1994) have been measured and modeled at microwave frequencies, albeit with lesser accuracies than presently attainable. For a solar abundance of each constituent, the predicted opacity of PH_3 below 30 GHz at 10 bars, 338 K is on the average 1.5 orders of magnitude lower than that from H_2O, calculated using the DeBoer model (de Pater *et al.* 2005), and at least 3 orders of magnitude below that of NH_3, calculated via Joiner and Steffes (1991). Under those conditions the opacity of H_2S is another half order of magnitude lower than PH_3.

Of the other major components of the Jovian atmosphere, the monatomic molecules of helium and the other noble gases are essentially lossless at microwave frequencies since they cannot have a dipole moment. Hydrogen, however, can possess a collisionally-induced dipole, but under the Jovian conditions probed by Juno its opacity is orders of magnitude lower than that of NH_3 or H_2O. (See, e.g., Borysow *et al.* 1985; Orton *et al.* 2007; Trafton 1973). Other various forms of NH_3 and H_2O exist at Jupiter where one or more hydrogen atoms is replaced with a deuterium atom (hydrogen with a neutron in its nucleus), but these are far less common and are not considered in this work.

2.3 Previous Measurements and Models

2.3.1 Ammonia

The microwave properties of gaseous ammonia were first measured in the laboratory by Cleeton and Williams (1934) from 7.5 – 30 GHz. They measured pure ammonia at a pressure near 1 bar, whereupon they detected a broad single line feature, because of

pressure-broadening and did not detect any individual NH_3 lines. Subsequent work was performed by Bleaney and Penrose (1946a) who were able to resolve 18 lines between 20 and 26 GHz by measuring at pressures of ammonia as low as 0.27 mbar and devised a formula for calculating NH_3 line frequencies based on quantum numbers. They concluded that NH_3, due to the strength of its dipole, exerts pressure broadening even at distances that do not correspond to direct collisions. Around the same time Good (1946a), in a cursory publication, was able to resolve 28 lines and later that year expanded that to 30 lines, along with a revised line frequency formula (Good 1946b). However, those results were subsequently dismissed as attempting to create a false sense of improved accuracy (Bleaney and Penrose 1946b; Bleaney and Penrose 1947). By 1949 pure ammonia had been measured from 3.7 to 37 GHz and up to 6 atm of pressure (Bleaney and Loubser 1950). One atmosphere of NH_3 was even measured up to 260 GHz by Nethercot *et al.* (1952). Many more measurements of pure ammonia were performed throughout the following decades by various researchers, culminating in the most extensive measurement to date of ammonia's inversion lines by Poynter and Kakar (1975). They measured the center frequencies of 119 lines up to $J = K = 16$ near 40 GHz for ammonia pressures of a few millitorr and devised a 15-term exponential polynomial for calculating the center frequencies of other lines. These measurements along with many others have been incorporated into the largest and most current collection of NH_3 microwave transitions, the JPL line catalog by Pickett *et al*. (1998) and more recently Chen *et al*. (2006).

It was not long before experimenters began to measure the broadening effects of various foreign gases on the microwave lines of ammonia. Bleaney and Penrose (1948)

measured the broadening effects of six gases, including H_2 and He by measuring the broadening of a single line ($J = 3$, $K = 3$), but did not make any acknowledgement of the adsorptive tendency of ammonia, leading the reader to believe they were either not aware of it, or did not properly account for it in their measurements. Smith and Howard (1950) measured 15 different broadening gases and described how strongly ammonia adsorbed in their system. Unfortunately, they do not mention the desorption process of ammonia and how that could have affected their measurements. Potter *et al*. (1951) obtained results that differed significantly with those of Smith and Howard and the theory proposed by Anderson (1949), but did not present any hypothesis as to the discrepancy. Legan *et al*. (1965) performed a more thorough examination of both ammonia self-broadening and foreign gas broadening on 25 NH_3 resonant lines. The aforementioned measurements of the various broadening parameters fall over a fairly wide range and are well outside their respective stated uncertainties, hinting at the difficulty in accurately measuring them.

Most of the early ammonia pressure-broadening experiments were limited to the pressures that could be produced in the laboratory, usually on the order of a few bars. Morris and Parsons (1970), however, were able to measure the broadening effects of H_2, He, N_2, and Ar on NH_3 up to pressures of nearly 700 bars by using a high-pressure vessel and gas compressor. Their measurements were only performed at room temperature and at one frequency (9.58 GHz) in a tunable resonant cavity. To date, the pressures at which these measurements of NH_3 were performed exceed those measured by other experimenters by nearly two orders of magnitude. Other measurements up to 6 bars by Steffes and Jenkins (1987) and an extensive set by Spilker (1990) up to 8 bars all suffer

from improper characterization of the adsorption of ammonia in the test chambers. Adsorption, however, had no effect on the measurements of pure ammonia by Spilker (1993). Measurements of the hydrogen and helium broadening of the K_a-band (32 – 40 GHz) and W-band (94 GHz) opacities of ammonia have been made up to 2 bars of pressure and temperatures from 188 to 300 K (Joiner 1991; Mohammed 2005), but those too have large uncertainties due to adsorption. Recently, more accurate measurements of the full W-band (75 – 110 GHz) opacity of H_2/He-broadened NH_3 have been performed (Devaraj and Steffes 2007).

The predominant lineshape used to describe experimental results for the ammonia spectrum of Good and Bleaney and Penrose was that of Van Vleck and Weisskopf (1945). The Van Vleck-Weisskopf lineshape was shown to fit the ammonia spectrum well at low pressures where the individual lines had little overlap. Although the accuracy of the Van Vleck-Weisskopf lineshape had been questioned in the lower frequency tail of the spectrum, it was not until 1953 that it was measured and found to be too low by 40% at 2.8 GHz in 133 mbar of pure NH_3 (Birnbaum and Maryott 1953). This led to the creation of new lineshapes (Anderson 1949; Gross 1955) with various modifications of the Van Vleck-Weisskopf theory. However, one that included the effects of increasing pressure on the molecular forces and resonant lineshapes of ammonia was not developed for over a decade (Ben-Reuven 1966). Despite the work of Ben-Reuven, Goodman (1969) devised the first model for calculating NH_3 opacity in a H_2/He atmosphere using the Van Vleck-Weisskopf lineshape. Berge and Gulkis (1976) used the Ben-Reuven lineshape to fit the measurements of Morris and Parsons (1970) to a model for NH_3 opacity in a H_2/He atmosphere using an empirical correction factor and only the NH_3

inversion lines from Poynter and Kakar (1975). The Berge and Gulkis model became the predominant way of calculating opacity from ammonia throughout the microwave regime until the models of Spilker (1990) and Joiner (1991). DePater and Massie (1985) recognized that the Berge and Gulkis model was inaccurate for millimeter waves due to the broadening effect of the rotational lines, namely those at 572, 1168, and 1215 GHz. This exposed the weakness of the Berge and Gulkis model's usable frequency range and further led to questions about the accuracy of its temperature dependence, both characteristics that were based on a single measurement. The Berge and Gulkis model was, however, shown to be accurate for pure ammonia at room temperature (Spilker 1993).

2.3.2 Water Vapor

Because of its prevalence on Earth, water vapor has been widely studied throughout the microwave regime mainly for its effects on weather, satellite and terrestrial communications. The first laboratory measurements of the microwave properties of water vapor were performed by Becker and Autler (1946) using a cubical copper resonator approximately 8 feet on a side. The gas measured in their massive resonator was essentially ambient air with additional amounts of H_2O. To prevent condensation and to allow greater amounts of water in vapor phase, the entire room housing the resonator had to be kept at 45° C! Like most early water vapor measurements, their focus was on the $5_{2,3} \rightarrow 6_{1,6}$ (22.2 GHz) line. Townes and Merritt (1946) were the first to measure this line in pure water vapor at low pressures to lessen the broadening and better constrain the center frequency and linewidth. Other early

measurements of the 22.2 GHz line consisted of characterizing attenuation in Earth's atmosphere with passive microwave radiometers (Dicke *et al.* 1946; Kyhl *et al.* 1946).

The $2_{2,0} \rightarrow 3_{1,3}$ (183.3 GHz) line was first observed by King and Gordy (1954) and measured in more detail, including self-broadening, and foreign gas broadening by Rusk (1965) and Frenkel and Woods (1966). Three additional lines up to 448 GHz were measured by Lichtenstein *et al*. (1966). Even more transitions up to 600 GHz were measured by Pearson *et al* (1991) and consolidated along with dozens of other measurements within the H_2O line catalog (Pickett *et al.* 1998).

Unfortunately, the majority of measurements of water vapor foreign gas broadening focus on gases normally found in the terrestrial atmosphere such as N_2, O_2, Ar, and CO_2, and not on those of the outer planets such as H_2 and He. The first measurement of the broadening of H_2 and He on H_2O was performed on the 22.2 GHz line by Liebe and Dillon (1969). Godon and Bauer (1988) examined the broadening by He on the 183.3 GHz and 380.2 GHz H_2O lines over the range of temperatures from 300 to 390 K, while Goyette and De Lucia (1990) studied He broadening of the 183.3 GHz line over the wider temperature range of 80 to 600 K. Dutta *et al*. (1993) measured the broadening by both H_2 and He on the lines at 183.3 GHz and 380.2 GHz. These measurements were repeated for He on the 183.3 GHz line at room temperature by Golubiatnikov (2005) and the results were in good agreement. All of these experiments, however, were performed with relatively low pressures (1-3 Torr) of broadening gases, which could lead to difficulties in extrapolating to higher pressures.

The first model for the microwave absorption of water vapor was created by Van Vleck (1947) using the Van Vleck-Weisskopf lineshape and only considering the line at

22.2 GHz along with attributing the contributions of all other lines to a single term. Goodman (1969) was the first to incorporate a hydrogen-helium atmosphere into a water vapor absorption model by following Van Vleck by also using only the 22.2 GHz line and combining the effects of the higher frequency lines into a single term. Hill (1986) later confirmed the correctness of the Van Vleck-Weisskopf lineshape for the 22.2 GHz line under lower pressures. Ho *et al*. (1966) measured H_2O in a N_2 atmosphere at high pressures and derived a model for H2O opacity under those conditions. Ulaby *et al*. (1981) created a model for H_2O absorption in Earth's atmosphere following the work of Waters (1976) by using ten rotational absorption lines up to 448 GHz and the kinetic/Gross lineshape. An additional term was added to represent the contributions of higher frequency lines per Gaut and Reifenstein (1971). Joiner and Steffes (1991) modified this model for a H_2/He atmosphere by replacing the term for Earth's atmospheric pressure P with ($0.81\ P_{H_2} + 0.25\ P_{He}$) where P_{H_2} and P_{He} represent the partial pressures of hydrogen and helium respectively. DeBoer (1995) further evolved this model by using the H_2 and He broadening parameters measured by Dutta *et al*. (1993). DeBoer's original formulation had multiple errors that were corrected (de Pater *et al.* 2005). The variation between the Goodman and DeBoer models is significant under the temperature and pressure extremes of the Jovian atmosphere. That discrepancy, along with the lack of measurements of the microwave properties of H_2O under high pressure, further motivated this work.

CHAPTER 3: LABORATORY MEASUREMENTS OF AMMONIA AND WATER VAPOR UNDER JOVIAN CONDITIONS

The current high-sensitivity microwave measurement system at the Planetary Atmospheres Lab of the Georgia Institute of Technology is based on that described previously by DeBoer and Steffes (1996), Kolodner and Steffes (1998), Hoffman *et al.* (2001), and more recently by Hanley and Steffes (2005; 2007). Several improvements to the system in the past few years have greatly improved its accuracy and precision. Most important among these is the recently added ability to characterize and compensate for molecules that selectively adsorb or adhere to the surfaces in the system. This laboratory system allows characterization of the refractive and absorptive microwave properties of various gases and gas mixtures under certain temperatures and pressures found in the atmospheres of our solar system's planets.

3.1 Measurement Theory

Electromagnetic fields of a uniform wave propagating in a gas mixture in the +z axis direction can be represented by

$$E(z) = E_o e^{-\alpha z} e^{-j\beta z} \tag{3.1}$$

$$H(z) = H_o e^{-\alpha z} e^{-j\beta z}, \tag{3.2}$$

where E_0 and H_0 are the amplitudes of the electric and magnetic fields and α and β are the attenuation and phase constants respectively. The phase constant is related to the wavelength (λ) of the propagation by

$$\lambda = \frac{2\pi}{\beta}. \tag{3.3}$$

The two properties that affect the transmission of electromagnetic waves through a medium are its permittivity (ε) and permeability (μ). For most cases the permeability is purely real, whereas the permittivity has both real and imaginary components $\varepsilon = \varepsilon' - j\varepsilon''$. These components are mutually dependent via the Kramers-Kronig relations (see, e.g., Ramo *et al*., 1994). In order to fully utilize these equations to calculate ε' one must have knowledge of the value of ε'' over all frequencies from zero to infinity and likewise to calculate ε'' one must also know ε' over all frequencies. While approximations can be used in some cases, such as a piecewise-linear model (Scott *et al.* 2005), their effectiveness is very limited in the bands near absorption lines where any uncertainties are compounded. Measuring these quantities in a laboratory setting most often provides more accurate results.

The attenuation and phase constants for a wave propagating at a frequency of ω can be written as

$$\alpha = \omega \sqrt{\left(\frac{\mu\varepsilon'}{2}\right)\left[\sqrt{1+\left(\frac{\varepsilon''}{\varepsilon'}\right)^2} - 1\right]} \tag{3.4}$$

$$\beta = \omega \sqrt{\left(\frac{\mu\varepsilon'}{2}\right)\left[\sqrt{1+\left(\frac{\varepsilon''}{\varepsilon'}\right)^2} + 1\right]}, \tag{3.5}$$

where α is in units of nepers/m and β is in units of radians/m (Ramo *et al.* 1994). Taking their ratio eliminates the dependence on ω and μ yielding

$$\frac{\alpha}{\beta} = \sqrt{\frac{\sqrt{1+\left(\frac{\varepsilon''}{\varepsilon'}\right)^2} - 1}{\sqrt{1+\left(\frac{\varepsilon''}{\varepsilon'}\right)^2} + 1}}. \tag{3.6}$$

The loss tangent of a gaseous medium is defined as

$$\tan\delta = \frac{\varepsilon''}{\varepsilon'} = \frac{1}{Q_{gas}}, \tag{3.7}$$

where Q_{gas} is the quality factor of the gas. For most gas mixtures at microwave frequencies, the loss tangent is much less than unity. This allows further simplification of equation 3.6 to

$$\frac{\alpha}{\beta} \cong \frac{\varepsilon''}{2\varepsilon'}. \tag{3.8}$$

Via equations 3.3 and 3.7, the attenuation constant, hereby referred to as the absorption coefficient or opacity, is calculated as

$$\alpha = \frac{\pi}{\lambda}\frac{1}{Q_{gas}}. \tag{3.9}$$

The method used to measure the microwave absorptivity of a gas is based on the lessening in the quality factor (Q) of a resonant mode of a cylindrical cavity in the presence of a lossy gas. This technique involves monitoring the changes in Q of different resonances of a cavity resonator in order to determine the refractive index and the absorption coefficient of an introduced gas or gas mixture (at those resonant frequencies). Described by Bleaney *et al*. (1947) it has been successfully utilized for over one half of a century. (See, e.g., Bleaney and Loubser 1950; Ho *et al.* 1966; Morris and Parsons 1970; Steffes and Eshleman 1981). The cavity resonator technique for measuring refractivity based on frequency shifts has had similar effectiveness. (See, e.g., Birnbaum 1950; Crain 1948; Essen 1953; Newell and Baird 1965).

The cylindrical cavity resonator consists of a section of cylindrical waveguide capped at both ends with resonant modes resulting from various standing-wave patterns. The Q of a resonance is a unitless quantity defined as

$$Q = \frac{2\pi f_0 \times \text{Energy Stored}}{\text{Average Power Loss}} \tag{3.10}$$

(Matthaei *et al.* 1980), where f_0 is the frequency of the resonance and can be measured directly as the frequency divided by its half-power bandwidth or full width at half maximum (*FWHM*)

$$Q = \frac{f_0}{BW} . \tag{3.11}$$

The quality factor of a resonator loaded or filled with a test gas can be represented by

$$\frac{1}{Q^m_{\text{loaded}}} = \frac{1}{Q_{\text{gas}}} + \frac{1}{Q_{\text{vac}}} + \frac{1}{Q_{\text{ext1}}} + \frac{1}{Q_{\text{ext2}}} \tag{3.12}$$

(Matthaei *et al.* 1980), where $Q^{\text{m}}_{\text{loaded}}$ is the measured quality factor of the gas filled resonator, Q_{gas} is the quality factor of the gas itself, Q_{vac} is the quality factor of the evacuated cavity resonator, and Q_{ext1} and Q_{ext2} represent the external coupling losses from the two coupling probes in the resonator. Since the resonators are essentially symmetric, we can assume $Q_{\text{ext1}} = Q_{\text{ext2}}$. The Q_{ext} value can be calculated by measuring the transmissivity of the system, $t=10^{-S/10}$ where S is the insertion loss of the resonator in decibels (dB) at the frequency of a particular resonance, and using the relations

$$t = \left[2\frac{Q^m}{Q_{ext}} \right]^2 \tag{3.13}$$

$$\frac{1}{Q_{ext}} = \frac{\sqrt{t}}{2Q^m} \tag{3.14}$$

(Matthaei *et al.* 1980), where Q^m represents a measured quality factor. The true Q_{vac} value is related to the measured value by

$$\frac{1}{Q_{vac}^m} = \frac{1}{Q_{vac}} + \frac{1}{Q_{ext1}} + \frac{1}{Q_{ext2}}. \tag{3.15}$$

Substitution of (3.14) into (3.12) and (3.15) yields

$$\frac{1}{Q_{gas}} = \frac{1-\sqrt{t_{loaded}}}{Q_{loaded}^m} - \frac{1-\sqrt{t_{vac}}}{Q_{vac}^m}, \tag{3.16}$$

with t_{loaded} and t_{vac} representing the transmissivities of the loaded and vacuum measurements respectively. Calculating Q_{gas} in this manner is slightly flawed, however, as this formula does not account for changes in the center frequency of a resonance when a gas is present. If measurements are conducted under relatively benign conditions, (e.g., 270 to 400 K), it is possible to construct a tunable resonator which can be retuned to the original resonant frequency when the test gas is present. (See, e.g., Ho *et al.* 1966; Morris and Parsons 1970). However, under conditions of extreme temperature and pressure it is very hard to construct reliable tunable resonators. If "fixed-tuned" resonators are used, the frequency shift, which accompanies the introduction of the gas under test, changes the coupling of the resonator and consequently the quality factor, even in the absence of opacity. Even if tunable resonators are used, the refractive effects of the gas under test can cause changes in coupling to the resonator, affecting the measured quality factor (Morris and Parsons 1970). Known as dielectric loading, described in greater detail in Spilker (1990), this effect requires additional measurements of the quality factor and transmissivity of a resonance to be made in the presence of a lossless gas exhibiting the same refractive index as that of the gas under test, as originally explained in Bussey and Birnbaum (1959). Using this measurement in place of that made under vacuum

conditions in (3.16), substituting into (3.9), and converting from nepers/km to dB/km (1 Np/km = 2 optical depths/km = 2*10 $\log_{10}$e (≈8.686) dB/km) gives the final formula for calculating absorptivity

$$\alpha = 8.686\frac{\pi}{\lambda}\left(\frac{1-\sqrt{t_{loaded}}}{Q_{loaded}^{m}} - \frac{1-\sqrt{t_{matched}}}{Q_{matched}^{m}}\right) \text{ (dB/km)} \tag{3.17}$$

(DeBoer and Steffes 1994), where the wavelength λ has units of km.

Like liquids and solids, gases also possess an index of refraction (n). Since n is relatively close to unity for most gases, it is more common to refer to the refractivity of a gas (N) defined as

$$N = 10^{6}\left(n-1\right). \tag{3.18}$$

Measuring refractivity is more direct than determining opacity and is calculated as

$$N = 10^{6}\frac{\left(f_{\text{vac}} - f_{\text{gas}}\right)}{f_{\text{gas}}}, \tag{3.19}$$

where f_{vac} and f_{gas} represent the center frequencies of a resonance measured with the system under vacuum and filled with the test gas mixture respectively (Tyler and Howard 1969). This represents the refractivity of the entire gas mixture, which is the sum of the constituents' refractivities weighted by their mole fractions. Refractivity is dependent on pressure and temperature and is often presented in a normalized form to exclude these dependencies. Normalized refractivity is calculated as

$$N' = \frac{NRT}{P} \text{ (cm}^3\cdot\text{molecule}^{-1}\text{)}, \tag{3.20}$$

where T is the temperature in Kelvin, P is the pressure in bars and R is the gas constant (=1.38065×10^{-22} bar·cm^3·molecule^{-1}·K^{-1}).

Although its value is not directly used in calculating absorption or refraction, knowing the asymmetry of a particular resonance is helpful in determining whether a resonance is corrupted by overlapping resonances of lower Q's and in calculating the corresponding measurement uncertainty. Asymmetry (A) can be defined as

$$A = 100\frac{(f_h - f_c) - (f_c - f_l)}{(f_h - f_l)}\% \tag{3.21}$$

(DeBoer and Steffes 1996), with f_h, f_l, and f_c, representing the higher frequency half power point, lower frequency half power point, and center frequency of the resonance respectively. Since two overlapping resonant modes might broaden disproportionately and give inaccurate results, only resonances with a low asymmetry (typically less than 5%) are used.

The center frequency of a TE or TM mode resonance in a cylindrical cavity can be calculated as:

$$f_{TE(N,M,L)} = \frac{c}{2\pi\sqrt{\mu_r \varepsilon_r}}\sqrt{\left(\frac{p_{NM}}{r}\right)^2 + \left(\frac{L\times\pi}{h}\right)^2} \tag{3.22}$$

$$f_{TM(N,M,L)} = \frac{c}{2\pi\sqrt{\mu_r \varepsilon_r}}\sqrt{\left(\frac{q_{NM}}{r}\right)^2 + \left(\frac{L\times\pi}{h}\right)^2}, \tag{3.23}$$

where μ_r and ε_r are the relative permeability and permittivity of the material inside the resonator, c is the speed of light in cm/s, r and h are the radius and height of the resonator in cm, q_{NM} is the M^{th} zero of the N^{th} order Bessel function of the first kind and p_{NM} is the M^{th} zero of the first derivative of the N^{th} order Bessel function of the first kind (Pozar 1998). A table of the Bessel function and its derivative zeros was calculated in Matlab® for the first 32 zeros up to the 50th order and can be found in the external electronic

references for this work[2]. The subscripts *N*, *M*, and *L* refer to the number of zeros in the standing wave patterns in the circumferential, radial and axial dimensions respectively. For both TE and TM modes, N can be any integer greater than or equal to zero, while M can be any integer greater than zero. For TE modes, L can be any integer greater than zero, while for TM modes, L can be any integer greater than or equal to zero. These formulas give rise to a large number of possible modes with increasing frequency. A plot of the measured spectra of the large cylindrical cavity resonator, described in the next section, along with the listing of modes can be seen in Figure 3.1. Only TE modes are measured in these experiments due to their higher quality factors (*Q*'s).

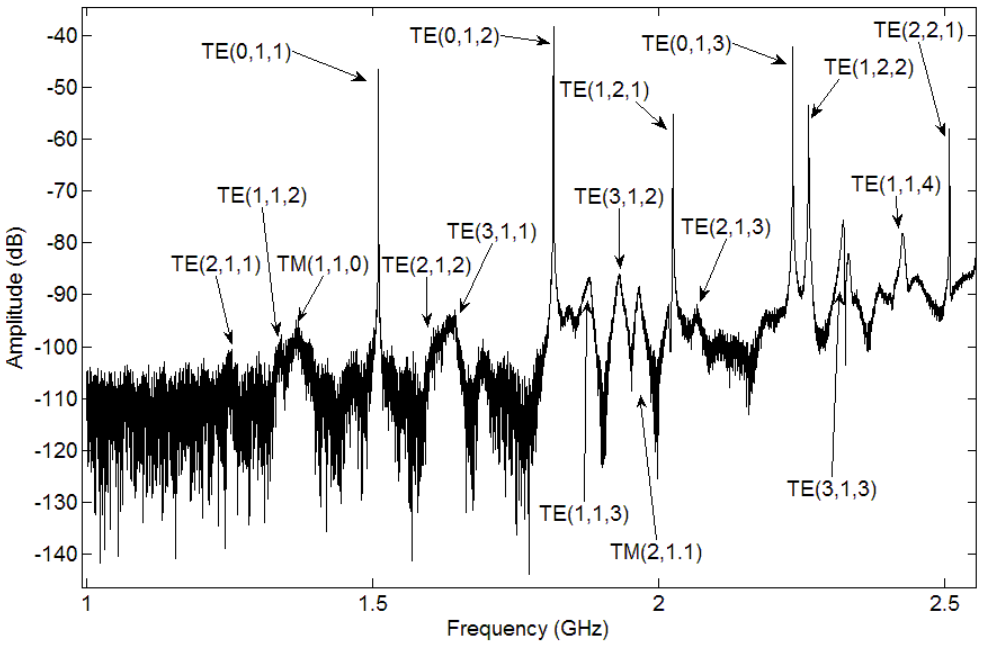

Figure 3.1: The measured spectrum of the large cylindrical cavity resonator. Many of the modes where $N \neq 0$ have been suppressed.

[2] Available online at *http://users.ece.gatech.edu/~psteffes/palpapers/hanley_data/bessel.xls*

3.2 System Description

The current measurement system configuration in use at Georgia Tech is shown in Figure 3.2. It is comprised of three major parts: the planetary atmospheric simulator, the microwave measurement subsystem, and the data handling subsystem.

3.2.1 Planetary Atmospheric Simulator

The planetary atmospheric simulator controls and monitors the environment experienced by the microwave resonators, including the temperature and pressure conditions for the gas under test. The main component of the atmospheric simulator is a pressure vessel capable of withstanding pressures from vacuum to 12 atm with a volume of approximately 31 liters. The vessel is cylindrical and made of type 304 stainless steel with a diameter approximately 15" and a detachable top plate sealed by a Viton® O-ring and vacuum grease. The O-ring rests in a groove on a flange connected to the cylinder. Both the groove and the top plate have been polished to increase the quality of the seal with the O-ring. The top plate is bolted to the rest of the vessel with eight 1" diameter bolts connected through unthreaded holes to washers and nuts and eight 3/8" bolts that are threaded into the bottom flange. The empty pressure vessel is shown next its inverted top plate in Figure 3.3.

Gases are fed into the vessel through a series of regulators and valves. All components in the gas handling subsystem are connected with seamless 3/8" outer diameter stainless steel tubing and Swagelok® fittings. The pressure vessel itself is contained in a temperature chamber. For temperatures between 173 K and 218 K, the temperature chamber is a Revco ultra-low temperature freezer. The freezer is not

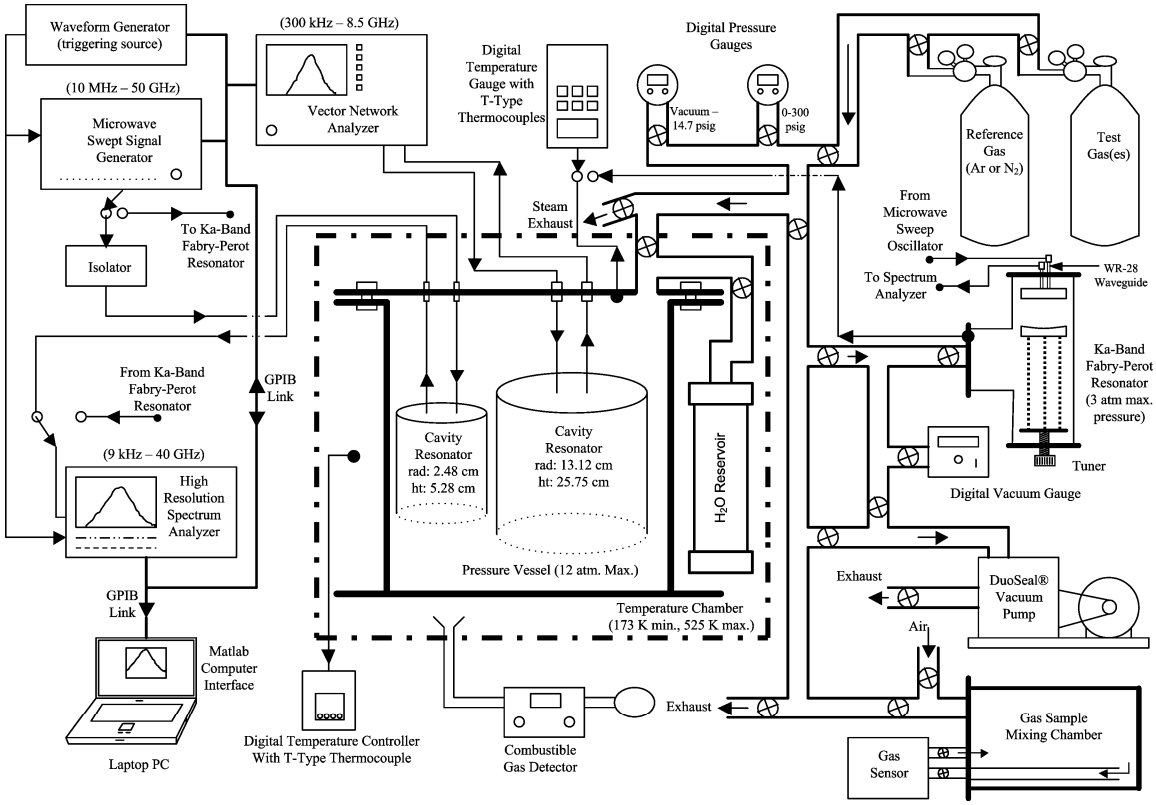

Figure 3.2: Block diagram of the gaseous microwave measurement system. Solid lines show electrical connections with arrows displaying the direction of signal propagation. Small crossed circles represent valves controlling the flow of gases.

programmed to operate any warmer than –55° C, which excludes performing measurements in the range of 218 to 290 K. At warmer temperatures between room temperature and 550 K, the vessel is placed in a digitally-controlled electric oven. The controller, an Omega® Series CN77000, operates with a relay in an on/off configuration with an adjustable differential. While this configuration is not as optimal at maintaining a constant temperature as a proportional–integral–derivative (PID) controller, the large thermal capacity of the system keeps temperature fluctuations inside the pressure vessel to below 0.1° C as verified by measurements. The temperature inside the pressure vessel is monitored by an Omega® Model HH21 Microprocessor Thermometer connected to a Type-T (copper/copper-nickel) pipe plug thermocouple probe threaded into a ¼ NPT fitting on the top of the vessel. This allows the probe to be in direct contact with the gases inside the vessel and provide a more accurate measurement of the temperature inside the vessel[3]. The thermometer has a resolution of 0.1º and a 3σ accuracy of 0.3% of the displayed value ±0.6º C at temperatures below 0º C and 0.1% ±0.6º C at temperatures above 0º C. The thermocouple itself has an accuracy of the greater of 1.0º C or 0.75% of the reading.

Positive pressures in the system are measured by an Omega® DPG7000 Digital Test Gauge with a resolution of 1 mbar and a 3σ accuracy of 10 mbar, capable of measuring pressures up to 300 psig, whereas pressures below ambient are measured by a Hastings Model 760 vacuum gauge with a resolution of 1 torr and a 3σ accuracy of 1 mbar. The vacuum gauge also has an analog voltage output, which when connected to a

[3] An earlier configuration used a Type-T thermocouple probe inserted into a sealed and capped inverted 3/8" outer diameter pipe protruding into the vessel, but not in direct contact with the gases inside. This configuration was prone to skewing the temperature reading toward that of the air outside the vessel and was replaced for experiments warmer than room temperature.

voltmeter can provide sub-millibar resolution which is accurate for differential measurements and monitoring leak rates. For cross-correlation, absolute pressures between two bars and vacuum are additionally measured by another DPG7000 Digital Test Gauge with a resolution of 0.1 mbar and a 3σ accuracy of 1.0 mbar. The reading on the vacuum gauge is temperature dependent and requires calibration with changes in room temperature to maintain its stated accuracy. The performance of the DPG7000 gauges is temperature independent within the operating temperature range[4] of -18º to 65º C, however, the gauges only display the differential pressure between the closed system and the room. This means that the gauge readouts can vary as the ambient pressure varies even for the same absolute pressure in the gas system. To correct for this effect, a digital barometer (Davis Weather Monitor II® 7440) with a 3σ accuracy of 1.7 mbar is used to measure the ambient pressure. Additionally, the pressure at the Atlanta, Fulton County Airport (approximately 7 miles from the laboratory) is monitored hourly via the National Weather Service website (*http://www.weather.gov*) for cross-correlation.

A Welch DuoSeal® vacuum pump Model 1376B-01 is used to evacuate the gases from the system from 1 bar absolute down to a level of 0.1 mbar. Gases at higher pressures are ventilated through an exhaust valve. This is especially useful when removing large amounts of water vapor from the system as it can condense and become trapped in the vacuum pump oil. This lowers the viscosity of the oil and lessens the strength of the vacuum in addition to causing the pump to heat up and possibly seize. The exhaust valve is located directly outside of the oven and positioned at a downward angle so that any condensed water will be forced out by the pressure of the expelled

[4] Note that the vacuum and pressure gauges are maintained at room temperature, external to the thermal chamber.

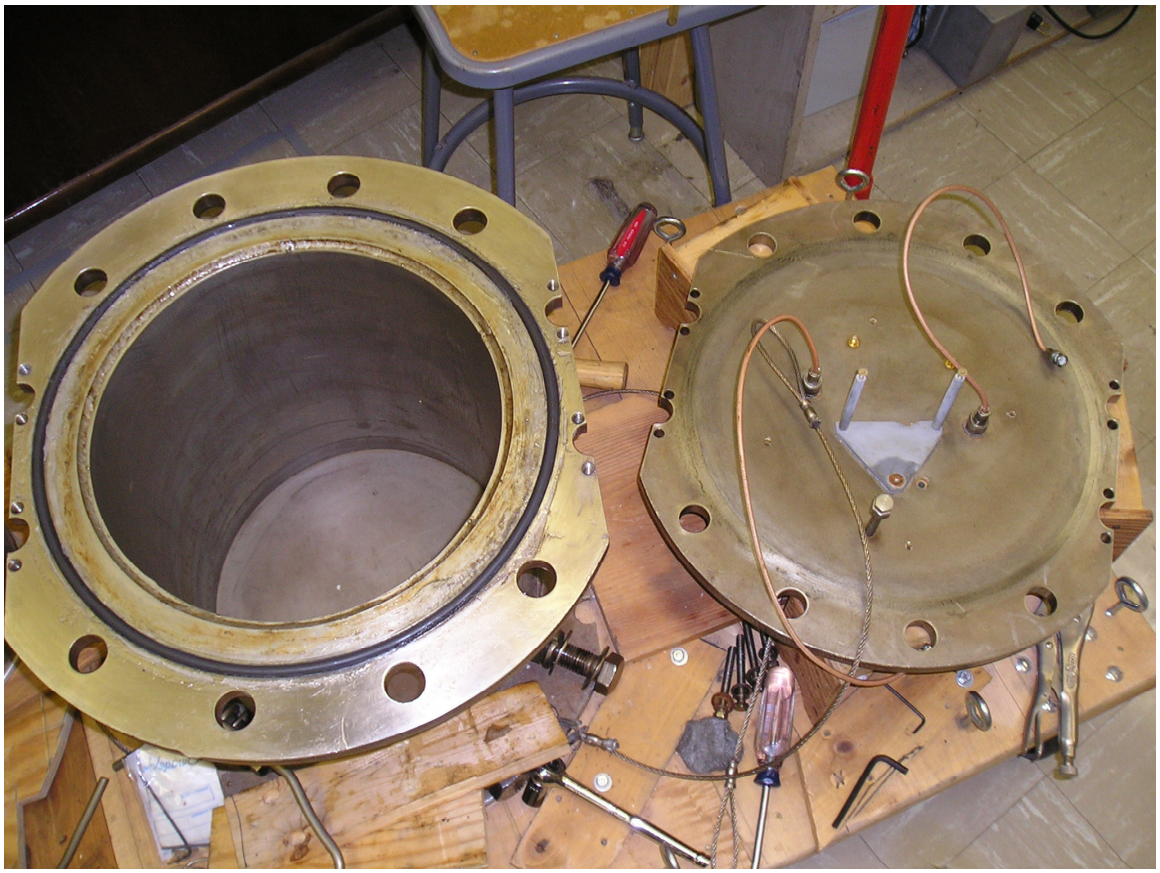

Figure 3.3: The empty pressure vessel next to its inverted top plate. Note the shelf that supports the small resonator and the thermocouple pipe on the top plate.

gases. This keeps the water contamination in the remainder of the connecting pipes and vacuum pump to a minimum.

For safety reasons, a combustible gas detector (GasTech model GP-204) can be used to detect leaks from the pressure vessel when the system contains hydrogen. A T-shaped glass tube with an inner diameter of 4" capable of withstanding 3 atm of pressure is also connected to the gas handling system for mixture sampling and characterization, but is maintained at room temperature. Additionally, a glass cylinder with a volume of approximately 7.2 L is connected to the system along with an Analytical Technology, Inc. PortaSens II portable gas leak detector capable of detecting trace amounts of gases through a series of interchangeable electrochemical cartridge sensors. The input of the detector is connected to a length of Tygon® tubing that samples the gas from the bottom of the cylinder, while the output of the detector is fed back into the top of the cylinder as can be seen in Figure 3.2.

For experiments involving the use of water vapor, a type 304 stainless steel pipe measuring 18" long and 1.5" in diameter with a volume just over 0.5 L is used as a reservoir for liquid water. It is sealed with a threaded cap on one end and two reducing couplings on the other to make it compatible with the 3/8" pipes used for the rest of the gas-handling system. The threaded joints are welded shut to completely seal the pipe and a valve is located on the end. Filling the reservoir involves evacuating the air inside and submerging the connecting pipe to siphon from a bottle of deionized, distilled water. The water reservoir can be positioned alongside the pressure vessel inside the digitally controlled oven.

3.2.2 Microwave Measurement Subsystem

The current microwave measurement subsystem has benefited greatly by continuous improvements in the speed, accuracy, and reliability of commercially available microwave measurement devices over the past twenty years. The basics of the measurements, however, remain unchanged. At the heart of this subsystem are two type 304 stainless steel cylindrical cavity resonators positioned inside the pressure vessel. These resonators have been plated with gold, so as to improve the quality factors of their resonances, and to prevent reactions with corrosive acid vapors that have been measured in previous experiments. (See, e.g., Hanley and Steffes 2005.) The two resonators with their top plates removed can be seen in Figure 3.4.

The interior dimensions of the larger of the two resonators range from 13.09 to 13.15 cm in radius and 25.38 to 25.82 cm in height. This makes it ideal for measurements from 1.5 to 8 GHz although higher frequency resonances have been measured up to 24 GHz, but with lesser accuracy. It rests at the bottom of the pressure vessel, whereas the smaller resonator, ranging from 2.479 to 2.497 cm in radius and 4.832 to 5.272 cm in height (internal dimensions), rests on a shelf suspended from the top of the pressure vessel. The small resonator is best used in measurements from 13 to 25GHz. Each resonator contains two closed-loop antenna probes mounted on their top plates and oriented to maximize the Q or quality factor of $TE_{(0,M,L)}$ modes. The Q's for most resonances in the large resonator range from 40,000 to 100,000 and in the small resonator they range from 10,000 to 30,000.

Both resonators are connected to hermetically-sealed bulkhead feedthrough connectors on the top plate of the pressure vessel, the large resonator using BNC type

Figure 3.4: The two cavity resonators with their top plates removed and inverted, showing the coupling probes

connectors converted to Type-N at the feedthrough and the small one using SMA connectors. Kings Microwave produced the SMA feedthroughs and CeramTec the Type-N feedthroughs[5]. The CeramTec feedthroughs, made of type 304 stainless steel, contain a ceramic-glass dielectric and are rated to 34 bars of pressure and temperatures between 73 – 498 K. They are welded to the pressure vessel lid whereas each SMA feedthrough is sealed with a Viton® O-ring compressed by a nut threaded on to the connector. The large resonator is connected internally using RG-142B coaxial cables and the small resonator is connected by two rigid coaxial cables with a silicon dioxide (SiO_2) dielectric designed to withstand extreme temperatures with minimal thermal expansion.

Each resonator has two horizontal slits on their circular sides near their top plates that act to suppress unwanted degenerate overlapping TM resonant modes, as well as allowing gases to enter their interiors. Additionally, the top and bottom plates of each resonator are isolated about 1.75 mm from the cylinder by a series of Teflon® or ceramic

[5] Originally, Type-N feedthroughs by Kings Microwave were used, but it was found that repeated thermal cycling caused pressure leaks through their Teflon® dielectric material.

(~99.8% Al_2O_3) washers around the connecting screws, which also increases the surface area through which gases can be exchanged between the resonator and the remainder of the vessel. This isolation or mode trap essentially eliminates TE and TM modes that require currents to be flowing between the top and bottom plates and the cylinder walls including the degenerate $TM_{(1,M,L)}$ modes, similar to the Teflon® rings used by Kumar *et al*. (1994). The added space between the cylinder and its end plates, however, allows more electromagnetic radiation to leak out of the resonator, even below the cutoff frequency of the slots. This leakage not only lowers the *Q*'s of the resonances, but can increase their asymmetry as the waves reflect off the inside of the pressure vessel and couple back into the resonators. The added interference of this phenomenon is damped out by wrapping the two resonators in a stainless steel mesh screen. Theory predicts that higher ordered modes at increasing frequencies should have greater *Q*'s than the lower ordered modes. While this is true for the resonators without any added spacers, the opposite occurs, according to equation 3.10, with the spacers in place as more energy escapes the resonators at higher frequencies. However, maintaining interference-free and high-sensitivity resonances is more important at lower frequencies to increase the detection threshold of the system, since the opacity of the test gases is proportional to frequency squared. Suppressing the degenerate TM modes greatly improves the accuracy and sensitivity of the measurements made on lower frequency $TE_{(0,M,L)}$ modes, therefore, the loss of sensitivity at higher frequencies is tolerated. This effect, shown in Figure 3.5, can be seen in the throughput and shape of $TE_{(0,1,1)}$ resonance in the large resonator before and after adding spacers. The assembled resonators with spacers can be seen in Figure 3.6.

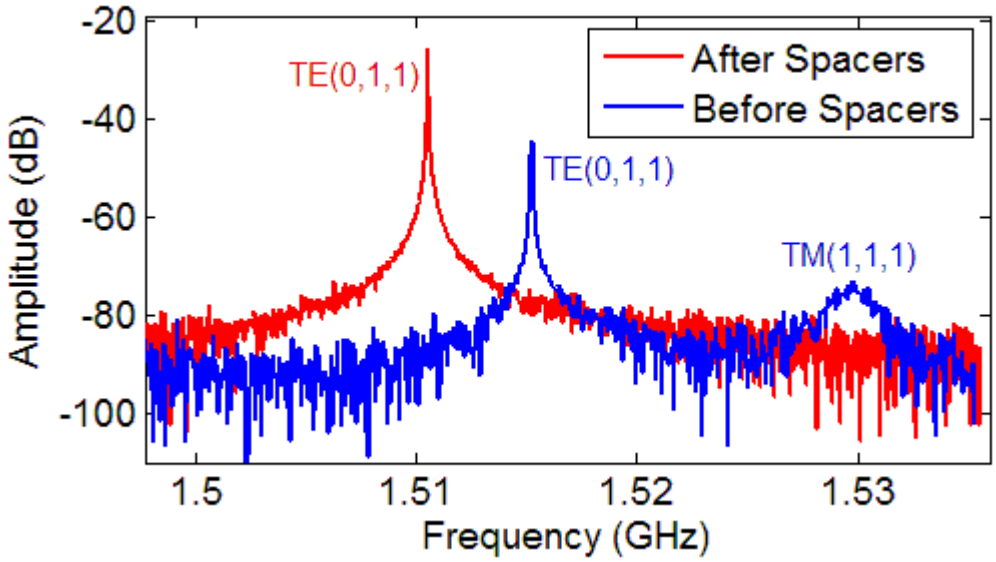

Figure 3.5: Spectra of the $TE_{(0,1,1)}$ resonance in the large resonator before and after adding spacers

The two ports for each resonator are essentially symmetric. The feed-through ports on the pressure vessel are connected internally to the large resonator and externally, via low-loss flexible coaxial cables, to a 2-port Agilent E5071C-ENA Vector Network Analyzer. The network analyzer operates from 300 kHz to 8.5 GHz with a high-stability timebase (Option 1E5). The feed-through ports connected internally to the small resonator have one port connected externally to the output from an HP 83650B Swept Signal Generator and the other to a high-resolution HP 8564E Spectrum Analyzer both via flexible, low-loss, high frequency coaxial cables. A number of ferrite isolators can be placed between the signal generator and the small resonator to provide a minimum of 10 dB of isolation for measurements up to 26.5 GHz. At higher frequencies, the cables themselves provide enough isolation from reflected signals due to their attenuation. Two isolators are primarily used, one operating from X-band through K_u-band (8 –17.5 GHz)

Figure 3.6: Large resonator (left) and small resonator (right) assembled with dielectric spacers

manufactured by Aertech and the other at K-band (18-26.5 GHz) by Pasternack[6]. All SMA connections are tightened with a calibrated 8 in-lb torque wrench to ensure reliable connections.

The detector within the spectrum analyzer operates in a positive peak mode, which displays the maximum power level received during the integration time of each point on each individual sweep. This mode is used primarily because it maximizes the data return to the computer. The normal mode detects both the high and low signal (noise floor) intensities at each frequency point, but when transferring to the computer,

[6] After repeated usage it was discovered that the Aertech isolator's insertion loss was overly sensitive to external magnetic fields, which varied with its orientation, so it was replaced with the better-shielded Pasternack isolator for use from X-band through K-band.

the spectrum analyzer is limited to 601 points in both the frequency and amplitude axes. In this mode, the peak level data becomes interspersed with the noise floor data, which would result in only half the data transferred being of practical use for these measurements and consequently would halve the frequency resolution. The network analyzer, on the other hand, offers variable and higher resolution (up to 1601 points) and does not suffer degradation due to its detection mode.

The signal generator and spectrum analyzer can also be connected to a Fabry-Perot resonator contained in the glass tube tee that operates at K/K_a-band from 22 to 40 GHz. The Fabry-Perot resonator is similar to that used by Mohammed and Steffes (2003) and Joiner *et al.* (1989) and consists of two gold-plated mirrors each 3.5" in diameter. One mirror is flat and contains two symmetric WR-28 waveguide ports and the other mirror is concave with a focal length around 20 cm. The position of the concave mirror is adjustable via a tuning screw and by adding standoffs between the mirror and the plate that supports it. The distance between the mirrors can be varied from 0 to 23 cm. However, additional resonances caused by reflections from the glass pressure-vessel endplates and scattering around the edges of the mirrors corrupt the spectrum when the mirrors are spaced farther apart. This places the optimum spacing somewhere between 5 and 6 cm, where the concave mirror acts as more of a flat mirror, and leads to resonances being spaced 2.5 – 3 GHz apart with Q's ranging from 5,700 to 13,300. The dramatic difference in the frequency response of the Fabry-Perot resonator with mirror position can be seen in Figure 3.7. By moving the mirrors closer together, the throughput at the resonant frequencies is increased by about 10 dB and the signal to noise increases by at least 20 dB for resonances below 30 GHz. The smaller amplitude higher frequency

"harmonic" resonant peaks for the 5.85 cm spacing are actually the result of the concave mirror being placed much closer than its focal distance. These peaks are far enough away from the main resonances, however, that any overlapping effects can be ignored.

The waveguides are connected to waveguide-to-coaxial SMA adapters, which are connected to 2'-long high-frequency flexible coaxial cables. As will be discussed, this resonator can be used to verify the mixing ratio of ammonia mixtures, which may have been modified by selective adsorption of polar constituents to the walls of the large pressure vessel and cylindrical cavity resonators. The Fabry-Perot resonator can be seen in Figure 3.8.

3.2.3 Data Handling Subsystem

The data acquisition subsystem consists of a laptop computer connected to the spectrum analyzer, network analyzer, and swept signal generator via a general purpose interface bus (GPIB) connected to a National Instruments NI-488.2 interface card. The suite of instruments is controlled via Matlab® and the Standard Commands for Programmable Instruments (SCPI) and HP BASIC languages. The primary function of the software is to control the instruments and retrieve resonance data from either the spectrum analyzer or network analyzer in the form of received power as a function of frequency. Each resonance is viewed with the amplitude axis extending over a 10 dB range and with the frequency axis being approximately twice the half-power bandwidth. This "zooming-in" on each resonance allows the best resolution without spreading the resonance over multiple screen widths. The resolution bandwidth (RB) of the spectrum analyzer is set to the value closest to $1/100^{th}$ of frequency span of a particular resonance under the

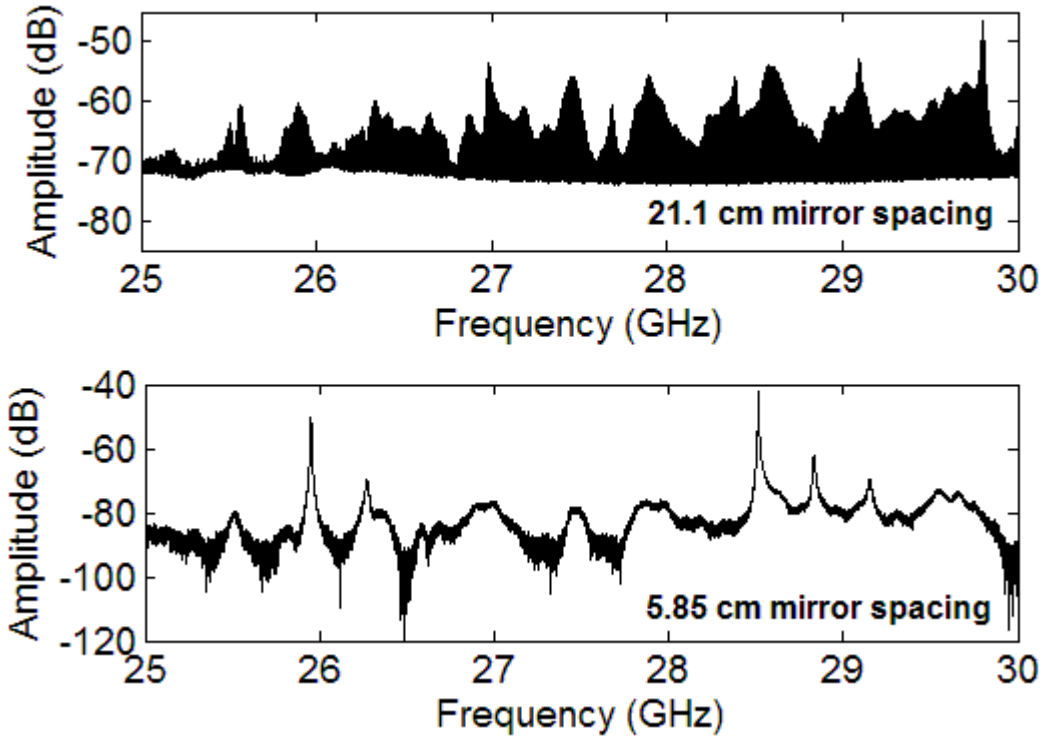

Figure 3.7: The spectra of the K/K_a-band Fabry-Perot resonator at vacuum at two different mirror distances. The 21.1 cm spacing appears colored-in because it was measured with the unsynchronized spectrum analyzer, whereas the 5.85 cm spacing was measured with a 40 GHz network analyzer.

Figure 3.8: The K/K_a-band Fabry-Perot resonator, with its mirrors spaced 5.85 cm apart, used for measuring NH3 concentrations. Note the flexible pipe used to limit the coupling of vibration from the vacuum pump to the resonator. The wire at the top of the resonator is a thermocouple probe and the cables at the bottom connect to the signal generator and spectrum analyzer.

resonance's broadest condition during the experiment. The value of RB is limited to 1 or 3 times any integer power of ten within the specifications of the device and is kept constant for all measurements of a specific resonance. The video bandwidth (VB) is set to $1/10^{th}$ of the resolution bandwidth, to provide some filtering of the signal. The software used is similar to the PCSA program created by DeBoer and Steffes (1996) but with the added flexibility of Matlab® and the ability to process the incoming data to directly calculate absorptivity and refractivity along with storing all raw data sets.

One problem that arises with the measurements taken using the spectrum analyzer is due to sweep-on-scan nulls. When it is not possible to synchronize the swept signal generator to the spectrum analyzer, the signal generator is set to sweep at a fast pace while the spectrum analyzer is set at a slower rate. The sweep rate for the signal generator is set to 75 ms at which the device can put out a stable power level at all frequencies used. It can be made to sweep as fast as 10ms, but the detected signal is noisier. Although the sweep time is 75 ms per sweep, there can be up to a 100ms delay between individual sweeps, depending on the frequency. In order for the spectrum analyzer to detect the signal in each measurement bin reliably, there must be a dwell time of at least ~175 ms during each of the 601 frequency measurement bins, which would require nearly two minutes per sweep. For each resonance measurement it is beneficial to take multiple sweeps to decrease variance, so it is optimal to have shorter, more frequent sweeps and to use the computer to average the results. If we limit the amount of time for each measurement to 200 seconds, the standard deviation of the set of measurements weighted by the statistical confidence coefficient seems to be minimized

for 5 sweeps of 40 seconds each. The data from each set of sweeps is saved in a unique file. An example plot of the raw data from one of these sweeps can be seen in Figure 3.9.

To utilize the data taken with the spectrum analyzer, the points where the input signal was not fully detected must be filtered out. Most of the time, the value of these points is equal to the baseline noise power of the measurement range and allows for easy filtering. However, because the input power is a swept Gaussian signal, there are times where the peak of the input signal is not detected within the resolution bandwidth of a data point, but some fraction of the signal is. These erroneous data points are more difficult to remove because their behavior is less predictable. To compensate for this, an algorithm is run to fill in all 601 data points as though they detected the peak of the swept input signal. The algorithm sets the value of each point equal to the average of the four nearest points (two higher and two lower) if it is less than that average. For the points within two of either end, the average is performed on fewer than four points to avoid the curve being leveled at the edges. This is done until an iteration is reached where the change at every point is less than 0.01% or a maximum number of 15 iterations has been reached. This corrects all the original null points but does not account for noisy spikes that stand above the good data. To compensate for these, the same algorithm is used, except that it only changes points that are greater than the average of the four nearest points until the change is less than 5% or a maximum of 10 iterations. Finally the data are smoothed once more with another four-point averaging filter where every point is set equal to the 4-point average until the change is less than 0.1% or a maximum of 5 iterations. This method, however, does not accurately measure the peak value of the resonance, especially in cases where the half power bandwidth is very narrow relative to

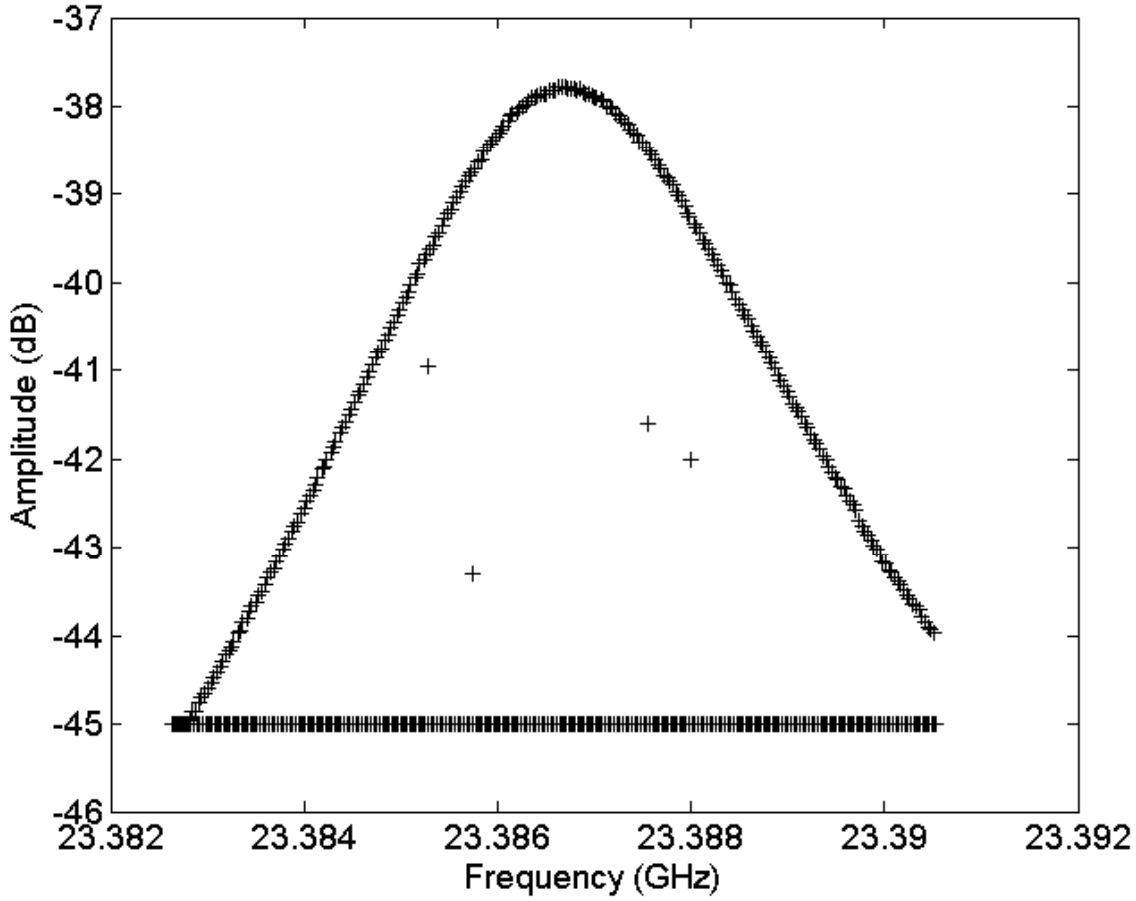

Figure 3.9: Spectrum analyzer output with a 40 second sweep time. The large number of data points at –45 dB result from sweep-on-scan nulls. The four intermediate valued points are the result of partial overlap of the swept signal with the spectrum analyzer's Gaussian detector.

the span, which occurs most often for dielectric matching of high opacity measurements. An averaging filter such as this would tend to level the data and if run through enough iterations, would eventually turn it into a horizontal line. Instead, this algorithm is merely used to detect which of the original 601 points received the peak power of the swept signal source. This is done by comparing the original data to the data from the algorithm and excluding the points where the difference between the two is greater than 0.1 dB. Note that the number of valid data points is typically between 200 and 250 of the 601 points returned by the spectrum analyzer in one sweep due to the sweep-on-scan effects.

A cubic smoothing spline, Matlab® function *csaps* or Fortran *SMOOTH* (de Boor 2001), with a relatively high smoothing factor is used to create a polynomial function to represent the valid data from spectrum analyzer, or any data taken by the network analyzer (which does not suffer from sweep-on-scan nulls). This allows a mathematically precise estimate of the peak value of the resonance and the corresponding half power or –3 dB points. A sample plot of the data fitted with smoothing splines using various smoothing parameters is shown in Figure 3.10. The software calculates the center frequency, half-power bandwidth, power level at the peak, asymmetry, and Q of each sweep and produces results for the mean and standard deviation of those values to another program which utilizes all the data taken during an experiment to calculate the measured absorptivities and refractivities and their corresponding uncertainties.

An effort was made to fit the spectrum of a resonance to its expected Lorentzian lineshape. A code was written to calculate the best fit of a Lorentz lineshape to the data. The scale parameters A and B along with the center frequency (f_{center}) and the bandwidth

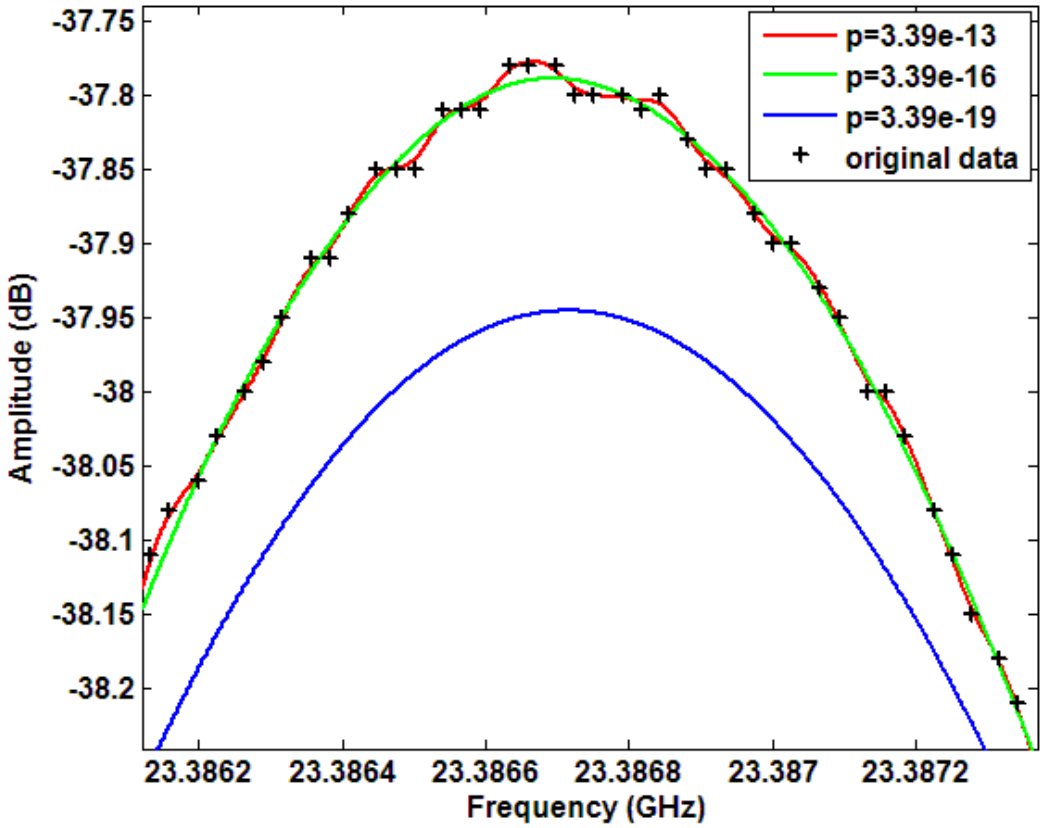

Figure 3.10: A close-up of the same data as Figure 3.9 fitted with the cubic smoothing spline using various smoothing parameters (p). As p goes to zero, the smoothed data become a straight line equivalent to a linear regression across the data set. The value of p used in the data processing is typically the default value calculated by Matlab (shown in red), divided by 10^3 or 10^4, as determined by limiting the overall average change in the peak amplitude to 0.02 dB.

at half-width, half-max (BW_{HWHF}) in equation 3.24 were optimized to minimize the difference between the data values and the fitted shape, summed for all sweeps:

$$\sum_{EachSweep}\left(Amplitude\_data(dB)-\left[A+B\log_{10}\left(\frac{{}^{1}\!/\!_{\pi}\times BW_{HWHM}}{\left(f_{center}-f_{data}\right)^{2}+BW_{HWHM}{}^{2}}\right)\right]\right). \tag{3.24}$$

While this approach worked quite well for resonances low in frequency such as the $TE_{(0,1,1)}$ mode in the large cylindrical resonator, the results were less accurate for higher frequency, more asymmetric resonances. This is primarily a result of the assumed perfect symmetry of the Lorentz lineshape. When fitting a Lorentzian lineshape to an asymmetric resonance, the calculated f_{center} value becomes skewed toward the broader side of the resonance along with lowering the amplitude of the resonance. Even in cases of relatively small asymmetry, this effect can significantly affect the calculated opacity values. In theory it could be possible to fit a Lorentz lineshape to every resonance in the spectrum of the resonator and subtract off the asymmetric overlapping effects from each resonance on each other. In reality, however, this task in computationally intensive and requires different BW_{HWHM} values for each resonance due to the frequency dependence of the opacity of the measured gas. This, combined with any potential defects in the shape of the resonator or energy leakage through the openings, makes the cubic smoothing spline a much more practical and effective method.

When it is possible to synchronize the swept signal generator with the spectrum analyzer, much greater resolution can be obtained, and much faster sweep times may be used. This is done with the use of an external waveform generator connected to the triggering inputs of the two devices. The waveform generator sends a square-wave signal to trigger the spectrum analyzer and signal generator to synchronously sweep. Merely

sending the trigger signal simultaneously is not sufficient for the devices to synchronize, since the processing delays internal to the devices are different. To compensate for this, the span of the signal generator is made 1.5% larger than the span of the spectrum analyzer. The sweep time of the swept signal generator is set to 1 s and the sweep time of the spectrum analyzer is set to 975 ms. These sweep times, when combined with processing delays on the order of 0.5 to 0.75 s, allow the triggering frequency to be set to 0.55 Hz, triggering the devices to sweep every 1.82 s. The resolution and video bandwidths of the spectrum analyzer are set to 10 times higher than their unsynchronized values to increase the ability of the spectrum analyzer to detect the swept signal. This method produces fairly accurate and much faster results, but is not always reliable. The amplitude of the detected signal has a greater variance than encountered using the unsynchronized mode and the wings of the resonance are not always consistent. This requires monitoring the data sweeps and disregarding those that did not completely synchronize. A measurement of the opacity of NH_3 at 184 K was performed using the spectrum analyzer and signal generator in synchronized and unsynchronized modes along with the network analyzer (for resonances below 8.5 GHz), and the results were consistent for all three methods. The measurement uncertainties of the network analyzer were the lowest, and the synchronized and unsynchronized uncertainties were essentially equal. The variability of the synchronized method, however, excluded its use for future high-accuracy measurements, although greater time savings have resulted from using the method for finding resonances and performing dielectric matching.

The measurements taken with the network analyzer are much quicker and require less processing. The network analyzer is capable of generating 60 synchronized data

sweeps in a single second at 1601 points of resolution. These 60 sweeps (30 each of S12 and S21) are saved to the laptop and then undergo the same processing to calculate the average and standard deviation of the center frequency, half-power bandwidth, power level, asymmetry, and *Q*.

3.3 Measurement Procedure

The first step of any experiment is to make sure the gas handling system is sufficiently leak-proof. Any major leaks will add to the uncertainty of the experiment and in the case of toxic or flammable gases present a health hazard. The most difficult component to seal is the pressure vessel. The top is tightened with up to 350 ft-lbs of torque on the large bolts at room temperature before it is placed in the temperature chamber. For warm experiments, the expansion of the metal creates a better seal, but the contrary is true at colder temperatures. For cold experiments the vessel is cooled to -55º C, the warmest temperature the freezer can maintain, and then it is removed from the freezer and immediately tightened again. Although the seal on the vessel is worse at experiments conducted as cold as -100º C any attempt to tighten the vessel at these temperatures could crack the Viton® O-ring. Additional tightening of the pressure vessel is performed with the vessel evacuated, which, given the approximately 200 square inches of surface area on its top plate, lends an additional 3000 lbs of compression force due to normal atmospheric pressure. Any leaky connections throughout the gas-handling system are detected at higher positive pressures using a soap-water solution to create bubbles.

With the system sealed, a series of experiments can be performed. A typical experiment consists of characterizing a gas or gas mixture at a fixed temperature across a

range of frequencies for various pressures. Due to the large thermal time constant of the system, changing temperatures during an experiment is too time consuming and impractical. However, this does provide smaller temperature fluctuations (typically no more than 1˚ C) throughout the duration of an experiment. Changes in pressure can cause slight changes in temperature as well as mixing ratio in the case of mixtures where some components adsorb and desorb more than others. This means that significantly changing pressures (more than +/- 100 mbar) requires allowing the system time to stabilize for anywhere from an hour to almost a day depending on the magnitude of the pressure change and the temperature of the experiment. The convenience of the network analyzer, signal generator, and spectrum analyzer make changing measurement frequencies almost instantaneous. Therefore, it becomes most efficient to measure a number of resonances once the system has stabilized at a specific temperature and pressure (TP). To ensure TP stabilization and thorough mixing of the gas(es) throughout the test chambers, the Q's of a number of resonances are monitored from the beginning of any pressure modification until the change in Q with respect to time (dQ/dt) is essentially zero or equivalent to a tolerable leak rate. This method is most accurate when small changes in temperature and mixing ratio measurably affect the microwave opacity, or in the pressure vessel where the mixing ratio of the gas in the large cylindrical cavity resonator is not yet equal to that in the small cylindrical cavity resonator.

When trying to characterize the pressure-broadening effects of one or more lossless gases on the opacity of a microwave absorbing gas, it is necessary to measure a mixture of the gases, since inter-molecular collisions cannot always be accurately theoretically characterized. Certified gas mixtures can be ordered to fairly accurate

specifications through most major gas suppliers, but if the goal of a series of experiments is to characterize the effects of different concentrations of the individual components, then it becomes more practical to use cylinders of pure gases and mix them in the measurement system using the pressure gauges to measure the amounts of each gas. When dealing with gases that have a strong tendency to adsorb to surfaces, such as molecules with a large dipole moment (i.e. H_2O and NH_3), certain precautions must be taken to ensure accurate production of a mixture. Since the abundances of typical microwave absorbers such as NH_3, H_2O, H_2S, SO_2 and PH_3 are usually much less than 1% in planetary atmospheres, realistic characterization (provided the opacity exceeds the sensitivity of the system) places the mole fraction of any one of these gases in the minority. This means that adsorption of these components can have drastic effects on the measurements if not properly accounted for.

For example, as a mixture of ammonia, hydrogen, and helium is added to the pressure vessel, it migrates through inlet gaps into the two cavity resonators. The surface-to-volume ratio of the pressure vessel and the two resonators are each different, as in Table 3.1. Thus, the time scales for reaching a stable mixing ratio throughout the two resonators *and* within the pressure vessel itself vary significantly. Since the large resonator has the smallest surface-to-volume ratio, it initially encounters less percentage ammonia adsorption (and therefore a higher ammonia mixing ratio, indicated by a lower quality factor of its resonances). By monitoring the quality factor of the resonator, it is possible to determine the time scale of the mixing process within the multi-resonator system whereby a uniform mixing ratio is reached. As shown in Figure 3.11, mixing ratio equilibration in the large resonator at 217 K for a mixture of ~1% NH_3 occurs over a

Table 3.1: Surface areas and volumes for the various regions inside the pressure vessel

	Volume (cm^3)	Surface Area (cm^2)	SA / V Ratio
Small resonator	102	117	1.14
Large resonator	13,919	3179	0.23
Remainder of vessel	~ 18,000	~ 9000	~ 0.50

period of approximately 15 hours. In the small resonator, the strong effect of the adsorption of ammonia is visible during the first hour after the gas mixture is introduced, as shown in Figure 3.12. However, once the sites on the metallic surface are occupied, no additional adsorption occurs. As equilibrium is reached with the gas contained in the remainder of the pressure vessel (where adsorption is less significant), the mixing ratio of ammonia rises (resulting in a lower quality factor).

The curves shown in Figures 3.11 and 3.12 represent the extreme case of the resonators without spacers/mode traps, operating at a cold temperature and high pressure. Typical equilibration times are on the order of 10 hours for room temperature measurements and even less for higher temperatures. For venting from higher pressures to lower pressures during an experiment, the equilibration times to allow for desorption are usually less than 5 hours.

The best way to create mixtures with small amounts of adsorbing constituents is to add those constituents to the system first and allow them to saturate the surfaces where they adsorb until equilibrium is reached between the amount of gas adsorbed, the surface coverage of the adsorption, and the partial pressure of the remaining adsorbate gas. At this point the rates of adsorption and desorption are equal. Although the majority of the adsorption occurs within the first few minutes, the gas can continue to adsorb up to 20

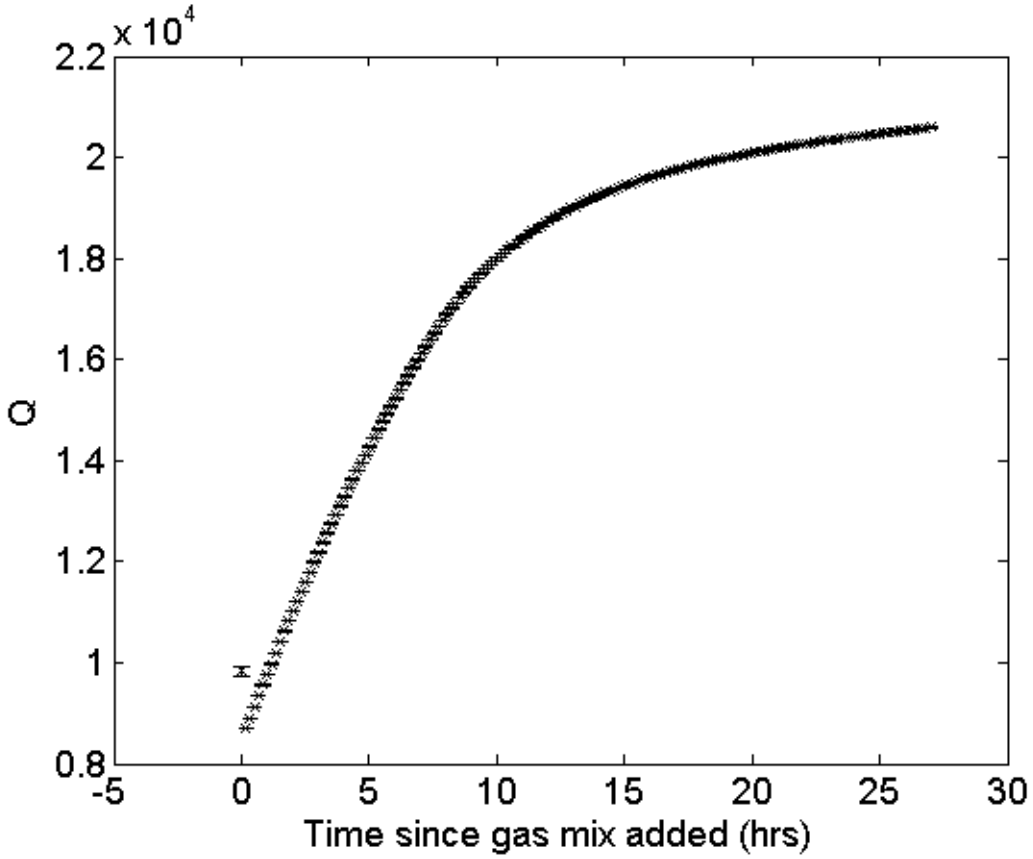

Figure 3.11: Measured *Q* of 4.151 GHz resonance in the large cylindrical cavity resonator as a function of time after a mixture of ~1% NH_3, 13.5% He, and 85.5% H_2 has been added to the pressure vessel at a temperature of 216 K and pressure of 6 bars. The increasing *Q* is due to the lessening of the opacity of the mixture caused mainly by two factors: the microwave absorber (NH_3) adsorbing or adhering to the sides of the test chambers and more thorough mixing of the gas between the two resonators and the remainder of the pressure vessel.

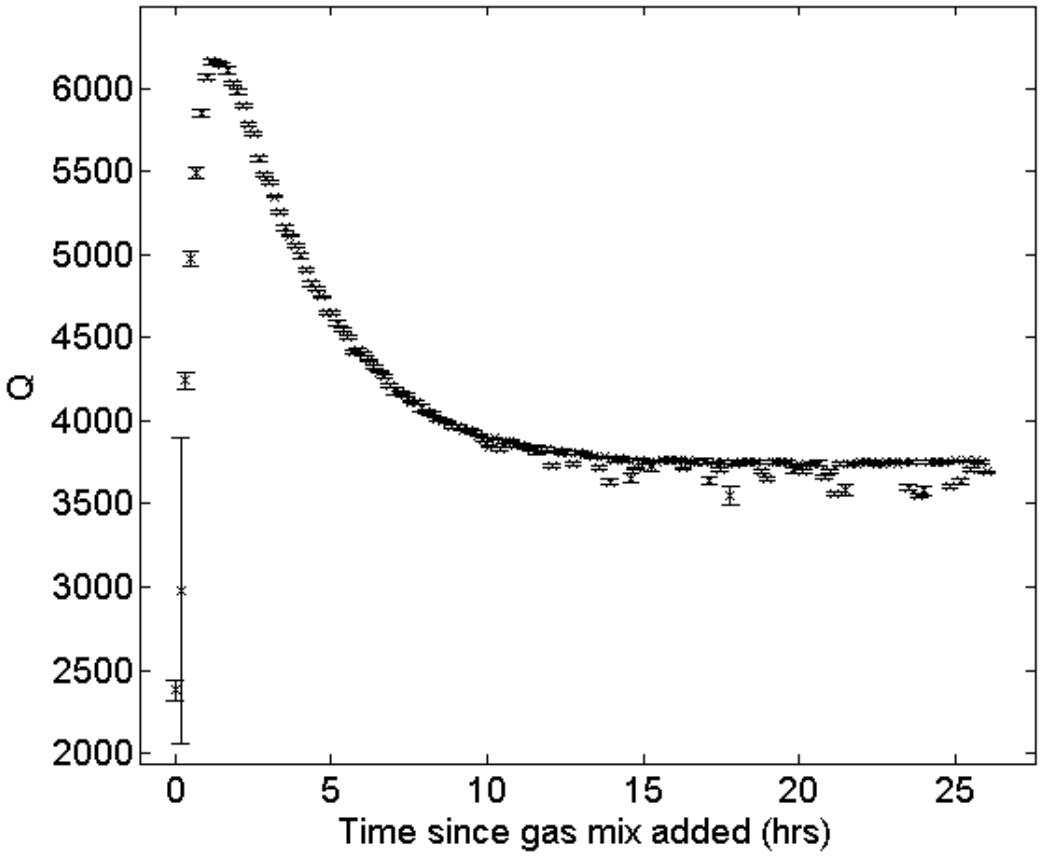

Figure 3.12: Measured Q of 17.53 GHz resonance in the small cylindrical cavity resonator as a function of time after a mixture of ~1% NH_3, 13.5% He, and 85.5% H_2 has been added to the pressure vessel at a temperature of 216 K and pressure of 6 bars. The sharp rise in Q results from NH_3 adsorption in the small resonator, whereas the accompanying decrease is caused by mixing throughout the vessel where the NH_3 concentration is greater.

hours after admission to the system depending on the pressure of the gas and the texture of the adsorbent surfaces. Once equilibrium is reached at the desired pressure of the adsorbing gas, additional gases are added until the maximum total pressure is reached (usually 3, 6, or 12 bars depending on the experiment). Additional lower pressures are achieved by venting or vacuuming the gas mixture from this point.

The uncertainty in knowledge of the mole fractions of each gas can be directly mapped to the uncertainty of the pressure or vacuum gauge used to measure each component. The greatest uncertainty usually lies in the mole fraction of the least abundant component, in this case NH_3 or H_2O. One way of reducing this is to create a mixture with a larger concentration of that component and then perform a series of dilutions. Unfortunately, if any of the constituents are strong adsorbers, which ammonia and water vapor are, diluting the mixture would cause a shift in the adsorption/desorption equilibrium since the partial pressure of that gas would decrease. This would lead to additional desorption and disproportionately increase the concentration of that gas. Therefore dilution can only be performed with non-polar gases. The desorption that occurs with a drop in partial pressure means that the measured mixing ratio at the original highest pressure will be less than that at lower pressures. To measure these mixing ratios in experiments performed in the pressure vessel, a small gas sample is drawn into the Fabry-Perot resonator and characterized from 22 – 40 GHz at 6 or 7 resonances. These data can be compared to that taken with known concentrations, or calculated using a model, provided an accurate one exists. Although the Fabry-Perot resonator is maintained at room temperature and is mostly glass, significant adsorption can still occur even there. This occurs not only on the metallic surfaces (mirrors, end plates, standoffs,

and waveguides), but also on the borosilicate (Pyrex®) glass, due to pairs of free unbonded electrons on the boron atoms. In order to compensate for this adsorption, a gas sample is introduced and allowed to equilibrate (adsorb), then half is removed and replaced with a fresh sample. This is repeated three or four times until the *dQ/dt* of the resonances in the Fabry-Perot resonator is no longer significant. At this point, the concentration of each gas in the pressure vessel is essentially equal to that in the Fabry-Perot resonator and the characterization from 22 – 40 GHz can be performed. A plot of the *Q* tracking for this procedure can be seen in Figure 3.13.

When an experiment is conducted using the Fabry-Perot resonator as the primary measurement tool, then a mixture is created at a higher pressure (6 – 12 bars) in the pressure vessel as previously described. This mixture can then be vented into the Fabry-Perot resonator and measured starting with the lower pressures and increasing, each time using the replace-half technique to compensate for adsorption in the Fabry-Perot system. This works without significant desorption in the pressure vessel because its volume is approximately 8 times that of the Fabry-Perot system, so the overall pressure change is relatively small. Nonetheless, it is best to measure samples at the lower pressures of an experiment in the Fabry-Perot resonator first and then the higher pressures.

After the gas or gas mixture has been measured at all the desired pressures of an experiment, a vacuum is drawn and the system is flushed a number of times with argon over a period of a few days. This ensures any adsorbed gases are removed so that when dielectric matching is performed, the gas present, argon, is lossless and does not contain any desorbed lossy gases. To double check that this is the case, argon is added to the system and allowed to stand for a number of hours. It is then drawn into the evacuated

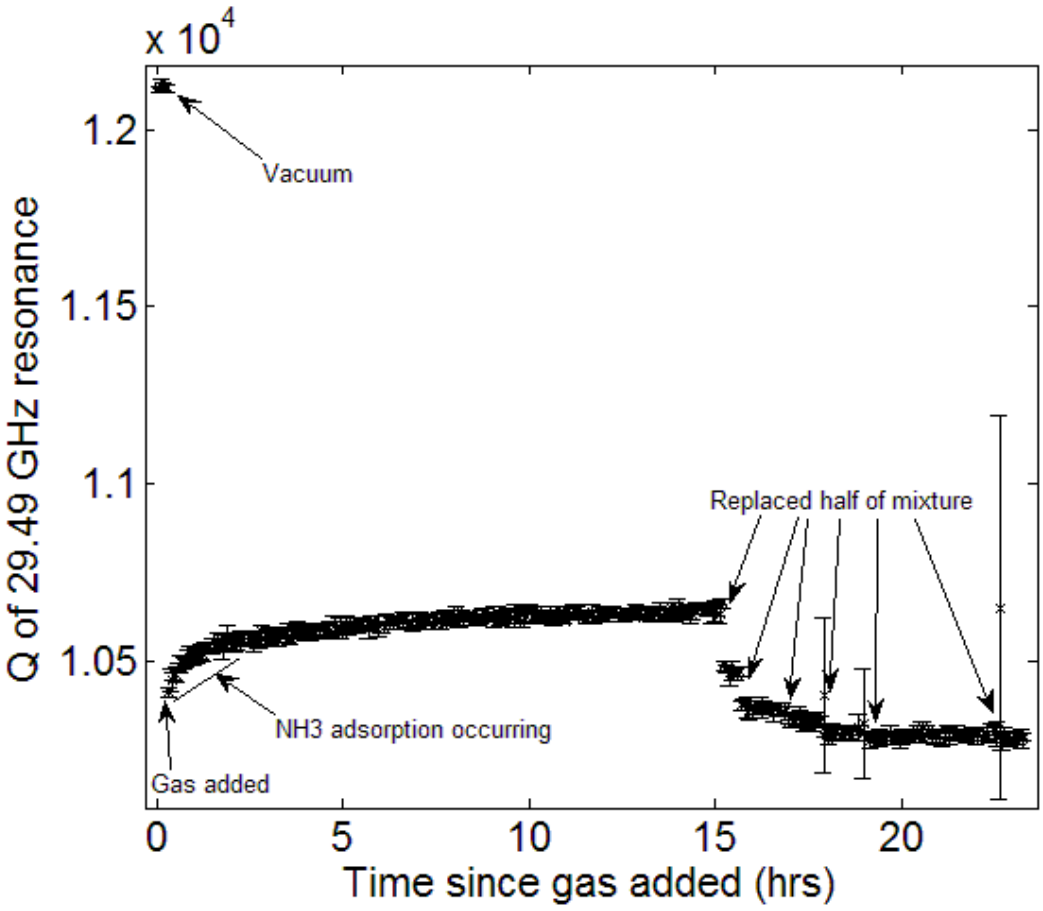

Figure 3.13: Tracking the Q of a 1% NH_3, 13.5% He, and 85.5% H_2 mixture at 1 bar. This data was taken with a 40 GHz network analyzer that allowed faster measurement times. The same patterns can be seen in the data taken with the spectrum analyzer, albeit with fewer points.

detection chamber to a level of 0.5 bar and mixed with ambient air to provide the minimum 5% oxygen required by the electrochemical sensor cell. This gas is continuously circled through the detector and the level of the adsorbate gas is measured in parts per million (ppm). Once the threshold of gas detection can no longer be reached (30 ppm for NH_3), the system is considered purged. As an added precaution, argon that is used during dielectric matching is not allowed to stand in the system for more than 6 hours without being replaced with fresh argon from the cylinder tank.

For a number of reasons, the gas detector is not used to directly measure the concentration of NH_3 gas mixtures from any experiments. As previously stated, the electrochemical cell requires at least 5% O_2, which is not present in any of the gas mixtures used in these experiments. Additionally, two percent of all H_2 molecules fed through the detector register a false positive for NH_3, while the maximum detectable concentration of NH_3 is only 0.2%, much lower than most concentrations used. Also, the detection chamber is made of Pyrex® or borosilicate glass, so NH_3 adsorption must be considered. Lastly, the chemical reaction in the sensor depletes the detector cartridge, which can only measure a finite amount of NH_3 in its lifetime and is designed around occasional detections of very small concentrations. The combination of these effects raises the uncertainties in concentration well beyond levels achieved through other methods, not to mention the additional cost (from replacement cartridges). Some ammonia analyzers exist that use non-reactive infrared sensors with heated sample lines to mitigate adsorption, but they are mostly designed for large volume gas applications such as monitoring smokestack emissions. (See, e.g., California Analytical Instruments Model 701 Ammonia Slip Analyzer). They can also be quite costly and still only offer

accuracies on the order of 2%. An attempt was even made to process a sample of NH_3 gas mixture through a quadrupole mass spectrometer via the assistance of colleagues in the School of Chemistry and Biochemistry, but the extremely low pressures involved only compounded the extent of ammonia adsorbing to the inside of the spectrometer. Coincidentally, this same effect occurred with the Galileo Probe Mass Spectrometer at Jupiter (Atreya *et al.* 2003).

Before any gases are added to the system, all the resonances of the system are measured under vacuum to create a baseline. The pressure gauges are zeroed to each other and to read minus one bar at vacuum. The ambient pressure is read from the barometer and noted. This reading is used for calibrating out any effect of variance in ambient pressure over the duration of an experiment. Since the ambient pressure readings are only used as a differential, there is no need to calibrate the barometer readings (which are relative to pressure at sea level) to account for the elevation of the laboratory. After the test gas(es) have been measured and the system has been purged, a second vacuum measurement is performed. Software calculates the frequency to which each resonance shifted while the system was loaded with the test gas. The software then prompts the user to add argon to the system until each resonance has shifted to that same frequency and a dielectrically matched measurement is taken. This usually requires a slightly different pressure of argon for each resonance depending on the structure of the absorption spectrum of the gas(es)[7]. The dielectric matched measurement is always performed at a temperature within 0.5 K of the original test gas mixture. After the end of

[7]Ideally, the dielectric matched measurement would be taken using the broadening gases (H_2/He) to remove any effects they may have on the opacity. Problems arise, however, in that hydrogen and helium are much less refractive at microwaves than the water vapor or ammonia. Trying to dielectrically match a mixture of H_2, He and NH_3 or H_2O with only H_2 and He requires a greater pressure. Since some measurements are already conducted near the maximum safe pressure of the vessel, the more refractive argon is instead used.

the dielectric matching, a third vacuum measurement is performed to check that the Q's of each resonance have returned to their pre-experiment values. Next, the cables are disconnected from the pressure vessel and connected together via a female-to-female Type-N or SMA connector, with the cable-to-cable connection kept inside of the thermal chamber. The straight-through transmissivities of the cables are then measured in the system under the same conditions (i.e. center frequency, span, RBW, etc.) as each pressure/frequency point of the test gas(es). The transmissivity measurements consist of multiple sweeps for each resonance and are measured two more separate times to conclude the experiment and better statistically characterize the reproducibility of the electrical connections. Each additional transmissivity measurement is performed after disconnecting and reconnecting the cables[8].

The digital pressure gauges cannot be operated inside the oven, so they must remain connected to the system at room temperature. This creates a problem with reading the pressures of warm gas mixtures containing components that would condense at room temperature, such as water vapor. This is not a concern for experiments with NH_3 since the amounts used are low relative to saturation and the gauges can be left in contact with the gas mixture. A different protocol, however, has been developed for reading the pressures of warm mixtures containing water vapor. The pressure vessel is sealed off from the external piping system via a valve internal to the oven. Water is first added to the evacuated pressure vessel in small amounts by quickly opening and closing the valve on the water reservoir. The shift in center frequency is monitored using the

[8] For the majority of the measurements in this work, a transmissivity measurement was performed before the second vacuum measurement. The greatest measurement accuracy, however, is achieved by not changing any of the electrical connections between the loaded and dielectrically matched measurements. Since the added uncertainty of disconnection and reconnection is fairly small, the uncertainties in transmissivity stated here are believed to be accurate.

$TE_{(0,1,1)}$ mode in the large cavity resonator to approximate the amount of water added. Once the target amount is reached, the system is allowed to stabilize and a measurement of the opacity of pure water vapor is performed. Then a small amount of broadening gas, in this case a H_2/He mixture, is added to the pipe connecting the pressure gauges to the pressure vessel to a pressure known to be greater than that in the pressure vessel, but not that much greater. Then while monitoring the reading on the pressure gauge, the valve between the pressure vessel and the pressure gauges is opened and the pressure quickly read before closing the valve again. The pressure reading stabilizes in less than a second, so the possibility of any significant amount of water vapor entering the pipes to the pressure gauges is very low. Since the volume of the pipe between the pressure gauges and vessel is very small relative to the volume of the pressure vessel and the pressure difference should be relatively small (less than 0.5 bar), no additional corrections need to be made to calculate the true pressure in the vessel prior to opening the pipe. After reading the pressure, additional broadening gas (H_2/He) is slowly added to the system. The flow is controlled via two needle valves, the one internal to the oven between the pressure gauges and the pressure vessel and the other between the pressure gauges and the gas cylinder. The former valve is opened fully and the latter valve is opened very slightly, about a 10° turn of the knob, to allow gas to flow at a slow, but steady rate. This allows directly reading the pressure in the vessel without allowing water to enter the piping due to the influx of H_2/He. Once the target pressure is reached, the internal valve is immediately closed, followed by the other valve. This also leaves enough gas in the pressure gauge pipe for the next pressure reading after the gas in the vessel has stabilized and been measured. This procedure is repeated for each desired pressure and works well

as long as the system is well sealed. In this case, a leak rate of less than 5 mbar per day at a pressure of 12 bars has been achieved at room temperature and warmer.

3.4 Data Processing

The data processing begins after an experiment has been completed. Software has been created that loads the experimental data, runs the smoothing algorithms, and calculates the absorptivity and refractivity of the test gas at the measured frequencies, pressures, temperature and mole fraction. A full description of the software can be found in Appendix B. The processing is broken down into two comparable routines, one for data taken with the spectrum analyzer and one for data taken with the network analyzer. The shape of any major variation in cable transmissivity over the frequency range of a resonance is deconvolved from the measured sweeps. Since this effect is quite small for resonances below 8.5 GHz, it is omitted for ease of calculation. The loss of the cables at the center frequency of each resonance under each pressure condition is calculated by averaging the values of the mean of each set of sweeps from the three transmissivity measurements. Additionally, the transmissivity of the cables inside the pressure vessel or the waveguides on the Fabry-Perot resonator must be considered. Since there is no easy way to measure these quantities without disassembling the chambers, no attempt was made to measure their effects until all the measurements of both NH_3 and H_2O were completed. At that point, the cables internal to the pressure vessel were measured in line with their feedthroughs to characterize the additional loss over the entire frequency band of operation. Another cubic spline was used to create a piecewise mathematical function of the loss in the internal cables of the pressure vessel for both the cables connecting the

small resonator and the large resonator. This function was used to generate an additional cabling loss at each measurement frequency that was added to the loss of the cables external to the vessel. The loss of the waveguides and waveguide-to-coax adapters in the Fabry-Perot resonator was measured with a resolution of 0.1 dB near the frequencies of the resonances used. The overall cabling or waveguide loss is subtracted from the peak power measured from the test gas and matching gas and the results are the loaded insertion loss (S_l) and matched insertion loss (S_m) respectively. These quantities are then used to generate t_{loaded} and $t_{matched}$ for equation 3.17.

The measured bandwidth is a function of the resolution bandwidth (RBW) and the filter response of the spectrum analyzer, which is assumed to be Gaussian. To correct for this effect, the following is applied:

$$BW_{actual} = \sqrt{BW_{measured}^2 - RBW^2}\ , \tag{3.25}$$

where BW_{actual} is used for BW in (3.11). This correction is not necessary for measurements using the network analyzer, since it is programmed to display the true response of the device under test. As mentioned previously, an experiment comparing the network analyzer performance to the spectrum analyzer showed that the two give consistent results with the data processing methods described herein.

3.4.1 Absorptivity

There are five uncertainties for any absorptivity measurement using this system: instrumentation errors and electrical noise (Err_{inst}), errors in dielectric matching (Err_{diel}), errors in transmissivity measurement (Err_{trans}), errors due to resonance asymmetry (Err_{asym}), and errors in measurement conditions (Err_{cond}) resulting from uncertainty in

temperature, pressure and mixing ratio. The term *Err* is used for representing uncertainties instead of the more frequently used σ to avoid confusion between 1σ, 2σ, and 3σ uncertainties.

The instrumentation errors and electrical noise result from the fact that none of the measurement devices used are perfect. Each has inherent limitations that arise from the noise of their internal electronics and the accuracies of their frequency references. For measurements made with the HP 8564E Spectrum Analyzer the two quantities of interest are the uncertainty in center frequency (Err_0) and half-power bandwidth (Err_Δ). The manufacturer-specified uncertainties are assumed to be 3σ values and are calculated per Hewlett-Packard (1997):

$$Err_0 < \pm\left(f_{reference\_accuracy} \times f_{measured} + 0.15 \times RBW + 0.01 \times SPAN + 10\right) \quad (3.26)$$

$$Err_\Delta < \pm\left(f_{reference\_accuracy} \times BW_{measured} + 4 \times N + 2 \times LSD\right), \quad (3.27)$$

where *RBW* is the resolution bandwidth, *N* is the mixer integer, and *LSD* is the least significant digit of the measured value. The mixer integer (*N*) is dependent on the frequency band measured and has values ranging from 1 to 8. The least significant digit (*LSD*) is calculated as

$$LSD = 10^x, \quad (3.28)$$

for the smallest non-negative integer value of *x* such that $SPAN < 10^{x+4}$. These formulas assume that $SPAN \le 2MHz \times N$. For situations where this is not the case, the 0.01 value in (3.26) is changed to 0.05. The frequency reference accuracy is calculated as

$$f_{reference\_accuracy} = 10^{-7} \times years\_since\_calibrated + 3.2 \times 10^{-8}, \quad (3.29)$$

where all variables have units of Hz, except for *N* and *LSD*, which are unitless. There is also a 3σ uncertainty in the value of the resolution bandwidth of ±10%, however, this only changes the value of equation 3.25 by less than 0.01%. It should be noted that the uncertainties presented above are the given specifications of the spectrum analyzer. The instrument is typically more accurate than this. Upon calibration after usage of more than seven years, the spectrum analyzer required no tuning and performed completely within the original specifications. Nonetheless, the previous formulas represent the worst-case condition.

For measurements using the Agilent E5071C-ENA Vector Network Analyzer, the absolute frequency accuracy is 1 part per million (ppm) or 0.0001% of the frequency reading. The 3σ stability of the frequency is 0.05 ppm plus 0.5 ppm/year within the temperature range of 18° C to 28° C and after a 90-minute warm-up period. The relative uncertainty in frequency is of greater concern than the absolute uncertainty, since the measurements are essentially differential with respect to frequency given an uncertainty as low as 1 ppm. Therefore (Err_0) is calculated as

$$Err_0 = f_{measured} \times \left(5\times10^{-8} + 5\times10^{-7} \times years\_since\_calibrated\right) \text{ (Hz)}, \quad (3.30)$$

with the measured frequency given in Hz. No specifications exist for calculating uncertainties in measured bandwidth for the network analyzer, so equation 3.30 was modified for calculating (Err_Δ)

$$Err_\Delta = BW_{measured} \times \sqrt{2} \times \left(5\times10^{-8} + 5\times10^{-7} \times years\_since\_calibrated\right) \text{ (Hz)}, \quad (3.31)$$

with the measured bandwidth given in Hz. The network analyzer was operated without any calibration corrections since the calibration standards cannot withstand the extreme temperature environment of most of the experiments. While the cables connecting the

pressure vessel could have been calibrated at room temperature, their performance would change once they were introduced into the temperature chamber, thus voiding the calibration. Instead the measured straight-thru transmissivity is essentially used to calibrate the amplitude values of S12 and S21.

In addition to the instrumental uncertainties of the spectrum and network analyzers, there are also uncertainties in the measurements caused by electrical noise. Each resonance measurement consists of a number of spectral sweeps, usually 5 for measurements with the spectrum analyzer and 30 with the network analyzer. The center frequency and bandwidth of the resonance for each sweep are measured and their mean values are used in calculating the respective *Q's* used in equations 3.17 and 3.38. (This averaging improves sensitivity since the electrical noise is uncorrelated between measurements and has equal chance of causing the measurements to read too high or too low.) Since the sweeps represent a sampling of the population of all measurements, the sample standard deviation (s_N) of each is calculated as

$$s_N = \sqrt{\frac{1}{n-1}\sum_{i=1}^{n}(x_i - \bar{x})^2}\ , \tag{3.32}$$

with $\bar{x}$ being the sample mean of the n number of measurements or sweeps. Of greater concern than trying to estimate the spread of the data is the probability that the true mean occurs within a specified interval of the measured mean. This interval is defined as the confidence interval and its spread varies with the confidence coefficient. The confidence coefficient is chosen such that the measured mean plus or minus its confidence interval contains the true population mean for a certain percentage of the time. For the measurements in this work, the confidence coefficient is chosen for a 95% chance, which

corresponds to roughly $2\times\sigma_N$ where σ_N is the standard deviation of the entire population of all measurements. The confidence coefficient is then equal to the critical value of the Student's *t*-Test (Student 1908) for a two-tailed significance of 0.05 and n-1 degrees of freedom. Thus 2.5% of the time, the true mean will fall above the confidence interval and 2.5% of the time it will fall below. Most statistics textbooks have tables of the t_{test} values, but for easier reference, one is provided here (Table 3.2) for sample sizes used in this work based on calculations performed in Matlab®.

Table 3.2: Critical values of t_{test} for 95% confidence

Number of Samples	3	5	10	30	∞
t_{test}	4.303	2.776	2.262	2.045	1.960

The ~2σ uncertainty in the mean of the population of the measurements (Err_N) is then calculated as

$$Err_N = \frac{t_{test}}{\sqrt{n}} s_N \,. \tag{3.33}$$

Equation 3.33 implies that the uncertainty in estimation of the true mean decreases with a greater number of measurements. Since the center frequency sample standard deviation of the measurements is a small fraction of a percent, its effects on the uncertainty in Q are disregarded and s_N refers only to the sample standard deviation of the bandwidth measurements for the remaining calculations.

The worst-case error scenario is used to transform the uncertainty in center frequency and bandwidth, for both the loaded and dielectrically matched measurements, into an uncertainty in absorptivity as described in DeBoer and Steffes (1994):

$$Err_{inst} = \pm \frac{8.686\pi}{\lambda} Err_{\psi} \text{ (dB/km)}, \tag{3.34}$$

with λ being the wavelength in km and σ_{ψ} calculated as

$$Err_{\psi} = \sqrt{\Gamma_l^2 + \Gamma_m^2 - 2(\Gamma_l \Gamma_m)}\,. \tag{3.35}$$

The other terms in (3.35) are calculated as

$$\Gamma_i^2 = \frac{\gamma_i^2}{f_{0i}^2}\left[\frac{Err_0^2}{Q_i^2} + Err_{\Delta}^2 + Err_{Ni}^2 + \frac{2Err_0 Err_{\Delta}}{Q_i}\right], \quad i = l,m \tag{3.36}$$

$$\Gamma_l \Gamma_m = -\frac{\gamma_l \gamma_m}{f_{0l} f_{0m}}\left[\frac{Err_0^2}{Q_l Q_m} + Err_{\Delta}^2 + \frac{Err_0 Err_{\Delta}}{Q_l} + \frac{Err_0 Err_{\Delta}}{Q_m}\right] \tag{3.37}$$

$$Q_i = \frac{f_{0i}}{BW_i}, \quad i = l,m \tag{3.38}$$

where the subscripts l and m denote the loaded and matched cases and γ, f_0, and BW represent the $1-\sqrt{t}$ terms from equation 3.17, the center frequency, and the bandwidth respectively. The center frequency and bandwidth used throughout the calculations have units of Hz and the Err_0 and Err_{Δ} terms used in (3.36) and (3.37) must be scaled by 2/3 of the values calculated by (3.26), (3.27), (3.30) and (3.31) to convert them to 2σ uncertainties.

Errors in dielectric matching arise from not precisely aligning the center frequency of the matched measurement with that of the loaded measurement. Since the Q of the resonator can vary slightly, even in the presence of a lossless gas, this effect creates an uncertainty in the Q of the matched measurement at the true center frequency

of the loaded measurement. To calculate the magnitude of this effect, the Q of the matched measurement is compared to the Q's of the three vacuum measurements to calculate the change in quality factor with frequency (dQ/df) for each resonance:

$$\left(\frac{dQ}{df}\right)_i = \left|\frac{Q_{vac,i} - Q_{matched}}{f_{vac,i} - f_{matched}}\right|, \quad \text{for } i = 1, 2, \text{ and } 3. \tag{3.39}$$

The maximum of the three dQ/df values is then used to generate a dQ value

$$dQ = \left(\frac{dQ}{df}\right)_{\max} \times \left|f_{loaded} - f_{matched}\right|, \tag{3.40}$$

where f_{loaded} and $f_{matched}$ are the center frequencies of the resonance under loaded and matched conditions respectively. This dQ value is then added to $Q^m_{matched}$ and α is calculated as in equation 3.17. The dQ value is also subtracted from $Q^m_{matched}$ and α is again calculated as in equation 3.17. The magnitude of the difference between these two α values is essentially a 2σ uncertainty and is designated by Err_{diel}.

The uncertainty in dielectric matching was non-trivial in the works of Hoffman *et al*. (2001) and Mohammed and Steffes (2003), where the alignment of the matched resonance with the loaded resonances was performed by eye. The development of software-aided positioning of the matched resonance to that of the loaded resonance has lowered this uncertainty to where its magnitude relative to the other uncertainties is insignificant. There are, however, a few instances where measurements could not be completed matched because of the large refractivities of the loaded gas(es). Therefore, the use of Err_{diel} is still considered.

Errors in transmissivity also affect the uncertainty of the measured opacity. While Err_{inst} is based on the ability to accurately measure frequency Err_{trans} results from uncertainty in the measurement of amplitude. This uncertainty is not only caused by the

instruments (spectrum analyzer, signal generator, and network analyzer), but also the cables that connect them to the resonators. The spectrum analyzer has a temperature stability of 0.1 dB/°C, but after being powered on for two hours, the internal temperature of the spectrum analyzer is stable enough to neglect this uncertainty. Like the network analyzer, other uncertainties in absolute magnitude are removed by the differential measurements of the insertion loss of the cables. The swept signal generator has a 3σ output amplitude accuracy (Err_{ssg}) of 1 dB for frequencies at or below 20 GHz and 1.2 dB for frequencies above 20 GHz. During measurements of the loaded or unloaded resonators the RF power of the signal generator is set to its maximum attainable leveled output to increase the signal to noise level (S/N) at the spectrum analyzer. This cannot be done, however, when measuring the loss of the cables since the power would exceed the maximum signal detection level of the spectrum analyzer. Therefore, all transmissivity measurements are performed with an RF output power of –10 dB. Since the power settings for transmissivity measurements and resonator measurements are not equal, identical differential measurements are not possible. Instead, the absolute amplitude uncertainty of the signal generator (Err_{ssg}) is utilized in these calculations.

The greatest uncertainty in the transmissivity measurements results from the process of disconnecting and reconnecting the cables. Since this process must occur at least once to change the connection of the cables from a resonator to each other, it is performed two more additional times to decrease the uncertainty of the statistical parameters. The standard deviation of these three measurements, calculated by (3.32), is then weighted by the t_{test} value for 3 samples and divided by the square root of 3 as in

(3.33) giving the measured transmissivity uncertainty (Err_{mt}). The uncertainty in insertion loss is then given as

$$Err_{ins\_loss} = \sqrt{Err_{mt}^2 + Err_{ssg}^2 + 0.25^2} \text{ (dB)}, \tag{3.41}$$

where Err_{ssg} is the uncertainty in RF output amplitude of the swept signal generator and the 0.25 factor is added to account for the uncertainty in the modeled loss of the cables or waveguides internal to the chambers. For measurements using the network analyzer, Err_{ssg} is set to zero. The insertion loss uncertainty is then used to derive the uncertainty in transmissivity by

$$Err_{t,i} = \frac{1}{2}\left(10^{-(S_i - Err_{ins\_loss})} - 10^{-(S_i + Err_{ins\_loss})}\right), \quad i = l,m \tag{3.42}$$

where the subscript i denotes the loaded and matched cases and S is the insertion loss of the resonator. This is then mapped to a 2σ uncertainty in opacity by a worst-case error propagation, giving

$$Err_{trans} = \frac{8.686}{2}\frac{\pi}{\lambda}\left(\frac{\sqrt{t_l + Err_{t,l}} - \sqrt{t_l - Err_{t,l}}}{Q^m_{loaded}} - \frac{\sqrt{t_m - Err_{t,m}} - \sqrt{t_m + Err_{t,m}}}{Q^m_{matched}}\right) \text{ (dB/km)}. \tag{3.43}$$

To test that the reproducibility of the electrical connections could be modeled in this way, 16 identical transmissivity measurements were made from 23 to 36 GHz using the small 2'-long cables, each time disconnecting and reconnecting the cables and even changing their orientations. The mean of the 16 measurements was then computed. A series of 3 of the 16 measurements were sampled at random and their mean and standard deviation were calculated. This was done for hundreds of repeated random samples and a scale factor was fit to multiply the standard deviation such that 95% of the time the mean plus or minus the scaled standard deviation would contain the mean of the 16 samples.

The value computed was 2.65, only slightly larger than 2.48, the t_{test} value for 3 samples divided by the square root of 3. It is believed that the difference is a result of both under sampling and the variation in behavior of the cables with orientation at those higher frequencies.

The asymmetry uncertainty results from the asymmetric nature of some resonances that could possibly be caused by overlapping with other resonances or defects in the resonators. This is computed by dividing each resonance at the peak power point and calculating two opacities as in (3.17), but with the Q's based on half power bandwidths calculated as

$$BW_h = 2\times\left(f_h - f_c\right) \tag{3.44}$$

$$BW_l = 2\times\left(f_c - f_l\right), \tag{3.45}$$

where BW_h and BW_l are the bandwidths of the high and low sides of the resonance respectively and f_h, f_l, and f_c, are as defined in (3.21). The difference between the opacities calculated with these bandwidths is essentially treated as a 2σ asymmetry error defined as Err_{asym}. This uncertainty accounts for disproportionate, asymmetric broadening by the test gas(es) relative to the matched measurements.

The uncertainty in measurement conditions (Err_{cond}) can only be computed if the pressure, temperature, and concentration dependences of the refractive and absorptive properties of the test gas mixture are known. Since this is not usually the case, their effects are often excluded from the stated measurement uncertainty with the acknowledgement of the conditional uncertainties elsewhere. This gives the final, 95% confidence, measurement uncertainty as

$$Err_\alpha = \sqrt{Err_{inst}^2 + Err_{diel}^2 + Err_{trans}^2 + Err_{asym}^2} \text{ (dB/km).} \tag{3.46}$$

The measurement condition uncertainties are also separated from Err_α since they apply equally to all of the resonances for an experiment at a particular pressure, temperature, and concentration. The relative median contribution of each uncertainty to the total can be seen in Table 3.3 for each resonator. If the dependence of opacity on pressure, temperature, or concentration can be modeled fairly accurately, then Err_{cond} can be calculated as

$$Err_{cond} = \sqrt{Err_{Temp}^2 + Err_P^2 + Err_C^2} \text{ (dB/km)}, \tag{3.47}$$

with Err_{Temp}, Err_P, and Err_C representing the 2σ uncertainties in temperature, pressure and concentration (or mole fraction) respectively. Each of those is calculated by taking the maximum modeled opacity with each uncertainty minus the minimum modeled opacity and halving the difference.

Table 3.3: Breakdown of the median percentage contribution of the uncertainties for each resonator. The large cylindrical cavity has slightly lower instrumental uncertainties since it was measured with the network analyzer, whereas the others were measured with the spectrum analyzer.

	Large Cylindrical Cavity	Small Cylindrical Cavity	Fabry-Perot
Err_{inst} (%)	0.68	1.13	2.34
Err_{diel} (%)	0.0075	0.046	0.088
Err_{trans} (%)	69.65	41.5	61.73
Err_{asym} (%)	29.66	57.33	35.85

3.4.2 Refractivity

Calculation of refractivity of a gas or gas mixture is performed by equation 3.19. While this may appear as a simple calculation, there are two compounding effects that require correcting.

The dimensions of the cylindrical cavity resonators changed throughout the course of the experiments as a result of various configurations. Initially the resonators did not have any dielectric washers isolating their end plates from the cylinders. This configuration, denoted *config. #1* for both resonators, was used for all of the 187 K and all but one of the 216 K ammonia experiments. At the time of those experiments, it had not yet been discovered that further isolation of the end plates from the central cylinder would result in greater damping of the degenerate $TM_{(1,M,L)}$ modes. As a result, most of the $TE_{(0,1,1)}$ and $TE_{(0,1,2)}$ mode data in the large resonator from those experiments had to be discarded. Other higher-ordered modes were less affected by this as the mode suppression slots cut into the top of the cylinders provided ample isolation. After this discovery had been made, Teflon® washers were added onto the screws that connected the top and bottom plates to their cylinders (*config. #2* for both resonators). Two washers were placed on each screw separating each plate from the cylinder by an additional 1.75mm and increasing the height of each resonator by 3.5mm. Additionally, the cylinder on the small resonator was inverted and rotated 90° to increase the symmetry of some resonances. This configuration was used for all of the room temperature measurements and one of the 216 K experiments that was performed as verification of the earlier 216 K data. It was also used for the preliminary measurements of ammonia at 375 K, but it was discovered that the Teflon washers became too soft and malleable at the warmer temperatures and led to changes in the height of the large resonator during the course of the experiments. At that time the configuration of the small resonator was again modified. Its cylinder was returned to its original configuration with the mode suppression slits on the top. The two Teflon® washers were replaced with one and the

standoffs that supported the resonator were trimmed by ~2 mm. This ensured that the two resonators would not be in contact as they thermally expanded, which might have lessened the quality of the vessel's seal and led to the previously measured changes in the large resonator's height during the experiment. Eventually the washers on the large resonator stabilized their shape and some experiments with water vapor at 350 and 375 K were carried out. Following those measurements, the washers on the large resonator were replaced with rigid ceramic (~99.8% Al_2O_3) washers with an operating temperature range from absolute zero to almost 2000 K. The Teflon® washers were not replaced in the small resonator since its lesser weight makes it less prone to deformation from the force of gravity.

Apart from the mechanical configuration changes, thermal expansion altered the dimensions of the resonators throughout the experiments. Being able to model the dimensions as a function of temperature is critical to more accurately characterizing the refraction of the gases measured. Each of the aforementioned configurations requires a separate formula for modeling each resonator's height as a function of temperature. Since nothing was done to modify the radius of the large resonator, only one formula is needed to model it. The small resonator, however, since its cylinder was inverted and rotated 90° for some of the experiments, requires two separate formulas for modeling its radius. This shows that the cylinder in the small resonator is about 3 μm wider in one dimension than the other, which limits its accuracy as a refractometer.

The formulas derived for each height and radius are based on subsets out of roughly 50 vacuum measurements from eight different groups of temperatures from 187 to 450 K. The center frequencies of all the measured $TE_{(0,M,L)}$ modes were compared to

the theoretical results from equation 3.22 (using $\mu_r = \varepsilon_r = 1$ for vacuum) and the parameters for radius (r) and height (h) were optimized to fit the data. This allowed assigning dimensions to the resonator at each temperature and fitting that data with a polynomial regression and least squares fit. For the radius of each resonator, the thermal expansion can be modeled as a quadratic whereas the height behaves linearly:

$$r = a_0 + a_1 \times T + a_2 \times T^2 \text{ (cm)} \tag{3.48}$$

$$h = b_0 + b_1 \times T \text{ (cm).} \tag{3.49}$$

For r and h given in cm and T in kelvin, the values for a_0, a_1, a_2, b_0, and b_1 for the various configurations can be found in Tables 3.4 and 3.5. The R^2 values are a measure of the goodness of the polynomial fit and represent the proportion of the variation in the data about the average that is explained by the model.

Table 3.4: Coefficients for modeling resonator radius (in cm) as a function of temperature (in K)

	Large resonator	Small resonator, *config. #1*	Small resonator, *config. #2*
a_0	13.06513	2.47258	2.47287
a_1	1.2895×10^{-4}	3.3034×10^{-5}	3.4841×10^{-5}
a_2	1.398×10^{-7}	1.522×10^{-8}	1.040×10^{-8}
R^2	0.99997	0.99994	0.99998

Table 3.5. Coefficients for modeling resonator height (in cm) as a function of temperature (in K)

	Large resonator *config. #1*	Large resonator *config. #2*	Large resonator *config. #3*	Large resonator *config. #4*	Small resonator *config. #1*	Small resonator *config. #2*	Small resonator *config. #3*
b_0	25.31654	25.63375	25.60325	25.61695	4.81633	5.25032	5.00384
b_1	3.6444×10^{-4}	4.1267×10^{-4}	4.5633×10^{-4}	4.6535×10^{-4}	7.9129×10^{-5}	1.0786×10^{-4}	7.9870×10^{-5}
R^2	0.9991	0.9999	0.9876	0.9995	0.9984	0.9981	0.9953

Although the numerical fits to the thermal expansion data are quite good, they are dependent on the accuracy of the temperature measurements. Thermal gradients vary throughout the vessel and are dependent of the specific heat of the gas mixture inside. For measurements at vacuum, there is no gas inside to transfer heat between the resonators and the thermocouple. Therefore, the time it takes for vessel to reach thermal equilibrium is longer than the cycle time of the thermostat on the thermal chamber and the temperatures of the vessel itself and the resonators inside may never equalize. This effect might have been reduced with the placement of thermistors on the sides of the resonators, but thermistors that can withstand the highest temperatures of some of the experiments do not have high enough accuracies. Also, the pressure vessel would have required additional feedthroughs. The placement of the thermocouple probe at the top of the vessel adds an additional uncertainty over the manufacturer's specifications for measurements at vacuum. This uncertainty is roughly 0.5° C for the large resonator at the bottom of the vessel and an additional 0.3° C for the small resonator near the top of the vessel.

Not only do thermal gradients exist across the vessel, but due to the specific heat of the gases measured in the experiments, the temperature of the system with the gases present is generally 0.3° to 2° C higher than the system under vacuum. This effect can be countered somewhat by changing the thermostat of the system as gases are added, but this task can be too painstaking and has limited accuracy, especially at room temperature. A better approach is to compensate for the temperature difference by modeling the resonators' dimensions as a function of temperature. From equations 3.48 and 3.49, the radius (r_{vac}) and height (h_{vac}) of the resonator at the average temperature of the three vacuum measurements (T_{vac}) is calculated along with the radius (r_{loaded}) and height (h_{loaded}) of the resonator at the temperature of the loaded gas (T_{loaded}). Additionally, the dimensions $r_{matched}$ and $h_{matched}$ at the temperature of the matched gas ($T_{matched}$) are also calculated.

Additional dimension corrections must be included for gas pressure, even though the resonators are contained within a pressure vessel and experience the same internal and external pressures. Adding gas to the vessel compresses the metal of the resonator and causes the radius to shrink while increasing its height. A classic text that presents formulas for calculating these types of deformations is *Roark's Formulas for Stress and Strain* (Young and Budynas 2002). The internal dimensions of the cavity resonators under gas compression are only dependent on the properties of their cylindrical middles. The end plates, while slightly flattened, will still maintain their positions relative to the cylinder due to gravity. To calculate the change in radius and height of a hollow cylinder under equal internal and external loading, the formulas for internal loading are combined with those for external loading. For a cylinder with internal radius b, external radius a,

and length l, the changes in the inner radius (Δb) and length (Δl) under uniform internal radial pressure (q) are given by

$$\Delta b = \frac{qb}{E}\left(\frac{a^2+b^2}{a^2-b^2}+v\right) \tag{3.50}$$

$$\Delta l = \frac{-qvl}{E}\frac{2b^2}{a^2-b^2}, \tag{3.51}$$

where v is Poisson's ratio (0.29 for type 304 stainless steel) and E is the modulus of elasticity (1.93 Mbar for type 304 stainless steel). Under uniform external radial pressure Δb and Δl are calculated as[9]

$$\Delta b = \frac{-qb}{E}\frac{2a^2}{a^2-b^2} \tag{3.52}$$

$$\Delta l = \frac{qvl}{E}\frac{2a^2}{a^2-b^2}. \tag{3.53}$$

Summing these two effects and simplifying the equations results in the final formulas for calculating Δb and Δl under uniform internal and external pressure:

$$\Delta b = \frac{-qb}{E}(1-v) \tag{3.52}$$

$$\Delta l = \frac{2qvl}{E}. \tag{3.53}$$

Although the dimensional changes are proportionately small ($\Delta b/b = 4.4\times10^{-6}$ and $\Delta l/l = 3.6\times10^{-6}$ at a pressure of 12 bars) their effects can still be seen in disproportionate frequency shifts with increasing mode numbers. Unfortunately, these formulas use the underlying assumption of a perfect cylinder in both external and internal radius. While the internal radius of the large resonator has been machined to a high precision, its

[9] In *Roark's Formulas* the published formula for Δb under external radial pressure on page 683 is missing a factor of b in the numerator.

external cross-section is more oval shaped with the wall thickness varying around the cylinder. Additionally, the angle between the end plates and the cylinder walls is not exactly 90°. These same issues are even more pertinent for the small resonator due to its smaller size and its aforementioned distorted radius. These effects could be counteracted in the data by comparing the measured refractivity of the lossless matching gas, in this case argon, whose refractivity at microwaves is frequency independent. This was not attempted for this work, however, since the effect is still smaller than that caused by uncertainty in temperature and frequency.

The result of the changing resonator dimensions is a corresponding change in resonant frequencies. To account for this effect when calculating refractivity, the center frequencies measured at vacuum must be transformed to the temperature and pressure of the loaded and matched measurements. First the radius and height of the resonator at the vacuum temperature r_{vac} and h_{vac} are scaled by the pressure of the loaded or matched case, depending on whether the goal is to calculate the refractivity of the test gas or the matching gas. Essentially the two refractivities should be equal, but slight temperature variations between the loaded and matched cases create small discrepancies. The new pressure corrected r_{vac} and h_{vac} values are given by

$$r_{vac,P} = r_{vac}\left(1-\frac{P}{E}(1-v)\right) \tag{3.54}$$

$$h_{vac,P} = h_{vac}\left(1+\frac{2Pv}{E}\right), \tag{3.55}$$

where P is the pressure in bars, v is the unitless Poisson's ratio, and E is the modulus of elasticity in bars. These values are used in equation 3.22 to generate frequencies ($f_{vac,P}$) of the resonances for the evacuated resonator under the same pressure conditions as the

test or matching gas. The frequencies of the evacuated resonator under the same temperature conditions are calculated using r_{loaded} and h_{loaded} or $r_{matched}$ and $h_{matched}$ in (3.22) to create $f_{vac,T}$. The pressure/temperature frequency correction factor (f_{PTcorr}) is then given as

$$f_{PTcorr} = f_{vac,P} - f_{vac,T} \,. \tag{3.55}$$

This gives rise to a modified form of equation 3.19 for calculating refractivity (N):

$$N = 10^6 \frac{(f_{vac} - f_{gas} - f_{PTcorr})}{f_{gas}}, \tag{3.56}$$

which can then be normalized via (3.20).

The uncertainty in the measured refractivity results from the uncertainty in the measurement of frequency, pressure and temperature. The uncertainty in frequency (Δf) is calculated in (3.26) and (3.30) for the spectrum analyzer and signal generator respectively. The uncertainty in the pressure and temperature correction term is calculated via worst-case error propagation, assuming a differential uncertainty in temperature of 0.5° C for the large cavity resonator and 0.3° C for the small cavity resonator. This is combined with the manufacturer specifications of the pressure gauges to calculate the maximum and minimum values of $f_{vac,P}$ and $f_{vac,T}$ for use in calculating the uncertainty in f_{PTcorr} (Δf_{PTcorr}). Since the percentage uncertainty in f_{gas} is very low, the uncertainty in N can be modeled as

$$\Delta N = \pm 10^6 \frac{\sqrt{\Delta f_{vac}^2 + \Delta f_{gas}^2 + \Delta f_{PTcorr}^2}}{f_{gas}}. \tag{3.57}$$

To further calculate the uncertainty in normalized refractivity, the pressure and temperature uncertainties must again be considered. Via (3.20) $\Delta N'$ can be calculated as

$$\Delta N' = \frac{NRT}{P}\sqrt{\left(\frac{\Delta N}{N}\right)^2 + \left(\frac{\Delta P}{P}\right)^2 + \left(\frac{\Delta T}{T}\right)^2} \text{ (cm}^3\text{·molecule}^{-1}\text{)}, \tag{3.58}$$

where ΔP and ΔT are the absolute uncertainties in pressure and temperature respectively, given by the manufacturer specifications of the measurement devices described in Section 3.2.1 and R is the gas constant. This formula describes the normalized refractivity of the entire gas mixture, but the goal is often to measure the normalized refractivity of only one of the gases in the mixture. The total measured refractivity of any mixture can be represented by the sum of the number density of each constituent weighted by their respective normalized molecular refractivities. In the case of mixtures of H_2, He and either H_2O or NH_3, this can be written as (Mohammed and Steffes 2003)

$$N_{meas} = \frac{N'_{H_2O,NH_3} P_{H_2O,NH_3}}{RT} + \frac{N'_{H_2} P_{H_2}}{RT} + \frac{N'_{He} P_{He}}{RT}, \tag{3.59}$$

where P_x is the partial pressure of the x constituent in bars, T is the temperature of the gas mixture in K, N' is the normalized refractivity of each constituent in N-units·cm^3 per molecule, and R = 1.38065×10^{-22} bar·cm^3·molecule^{-1}·K^{-1}. The quantity of interest $N'_{H2O,NH3}$ can be solved for as

$$N'_{H_2O,NH_3} = \frac{N_{meas} RT - N'_{H_2} P_{H_2} - N'_{He} P_{He}}{P_{H_2O,NH_3}} \text{ (cm}^3\text{·molecule}^{-1}\text{)}. \tag{3.60}$$

Newell and Baird (1965) measured the refractivity of hydrogen and helium at 47.7 GHz and normalized the values to 1 atmosphere of pressure and 0° C. Their results are a refractivity of 135.77 ± 0.05 for hydrogen and 34.51 ± 0.05 for helium. Normalizing these gives N'_{H2} = 5.053×10^{-18} cm^3·molecule^{-1} and N'_{He} = 1.284×10^{-18} cm^3·molecule^{-1}. These values are more accurate than the previously measurements of Essen (1953) at 9 GHz and are comparable to those measured by Spilker (1990) between 9 and 18 GHz.

Since the refractivities of H_2 and He are constant across the microwave band, the values measured at 47.7 GHz are used here instead of those at 9 GHz, despite being farther from most of the measured frequencies used in this work.

Calculating the uncertainty in normalized refractivity in (3.60) is notably more complicated than the formula presented in equation 3.58. The addition of uncertainties in partial pressures of each constituent causes an increase in the overall percentage uncertainty. Again, a worst-case error propagation approach is used to calculate the effect of all the individual uncertainties on the total by varying one component at a time and taking the quadrature sum of the individual results.

CHAPTER 4: RESULTS, DATA FITTING AND NEW NH_3 OPACITY MODEL

4.1 Experimental Results

Initial measurements of the microwave opacity of ammonia in a hydrogen/helium atmosphere were performed by this author beginning in December of 2004 using the cylindrical cavity resonators, with over a dozen experiments performed throughout 2005. However, the early measurements were insufficient to draw any more accurate conclusions about the opacity of NH_3 than already measured by other authors. What these experiments did provide, were data that eventually led to an improved understanding of the process of adsorption and gas mixing throughout the measurement system. With this added understanding and the addition of the K/K_a-band Fabry-Perot resonator, the greatest uncertainty of the previous measurements (the concentration of NH_3) was reduced to achieve much more accurate results. With these improvements in place, new measurements were initiated in June of 2006.

The frequencies of the resonances most used in the measurements of ammonia and water vapor are listed in Tables 4.1 and 4.2 along with their mode numbers, typical *Q*'s and the conditions under which they best performed. These are the resonant frequencies of the resonators under vacuum at 295 K. If gases are added to the resonators or their temperatures are increased, the resonances shift to lower frequencies. There are many more usable resonances in the large resonator than the small resonator. Additionally, the higher *Q*'s in the large resonator allowed data taken using that resonator to have lower uncertainties. The degraded performance of the small resonator is most likely due to the dimensions of the resonator and the behavior of the coupling probes. In

Table 4.1: The most commonly used resonances in the large cylindrical cavity resonator. The frequencies correspond to the resonator with height configuration #2 from Table 3.5 at 295K under vacuum.

Frequency (GHz)	TE Mode Number (*N*,*M*,*L*)	Typical Q_{vac}	Notes:
1.5105	(0,1,1)	67,500	Worked well for all measurements with added dielectric spacers.
1.8160	(0,1,2)	63,200	Worked well for all measurements with added dielectric spacers.
2.2342	(0,1,3)	63,100	Worked well for almost all measurements.
2.7135	(0,1,4)	65,700	Worked well for all measurements below 300 K.
2.8052	(0,2,2)	83,900	Worked well for all measurements with added dielectric spacers.
3.0924	(0,2,3)	76,300	Worked well for all measurements with added dielectric spacers.
4.3254	(0,2,6)	60,800	Worked well for all measurements with added dielectric spacers below 400 K.
5.0885	(0,3,6)	92,100	Worked well for all measurements with added dielectric spacers.
5.3097	(0,2,8)	52,200	Worked well for all measurements.

Table 4.2: The most commonly used resonances in the small cylindrical cavity resonator. The frequencies correspond to the resonator with radius configuration #2 and height configuration #2 from Tables 3.4 and 3.5 at 295K under vacuum.

Frequency (GHz)	TE Mode Number (*N*,*M*,*L*)	Typical Q_{vac}	Notes:
14.6228	(0,2,2)	23,000	Worked well for all measurements with added dielectric spacers.
15.9390	(0,2,3)	16,800	Worked well for all measurements.
21.3162	(0,3,3)	16,700	Worked reasonably well for almost all measurements.
22.5971	(0,3,4)	10,800	Worked well for almost all measurements.
24.1460	(0,3,5)	11,100	Worked reasonably well for almost all measurements.

the case of this work, the increased opacity resulting from the ammonia inversion lines near 24 GHz compensates for the lesser measurement sensitivity in the small resonator.

4.1.1 Ammonia

The microwave opacity of NH_3 in an H_2/He atmosphere was measured at five different temperature bands: 184-189 K, 213-218 K, 292-297 K, 372-377 K, 445-450 K. The pressures ranged from as low as 30 mbar to as high as 12 bars and the NH_3 concentration ranged from 0.06% to 8% with a handful of measurements of 100% NH_3. The frequencies measured range from 1.5 GHz to 27 GHz for measurements using the cylindrical cavity resonators and 22 GHz to 39 GHz for measurements using the Fabry-Perot resonator. Measurements using the Fabry-Perot resonator were limited to room temperature, however. Each experiment involved measuring an average of 30 resonances

with the hope that each would provide usable data. Over 80 resonances in the two cavity resonators were utilized for at least one experiment. It was discovered that virtually all of the $TE_{(N,M,L)}$ resonances where $N \neq 0$ were unable to provide useful data once the dielectric spacers were added to the resonators. The measurements using these resonances generally overestimated the opacity of the gas. Resonances with $N = 0$, however, became much more reliable with the dielectric spacers present and these represent the majority of the measurements.

The hydrogen and helium used in the experiments came from a certified premixed cylinder with (13.6 ± 0.272)% He and the remainder H_2. This is approximately the helium mole fraction at Jupiter as measured by the Galileo probe (von Zahn *et al.* 1998). Additionally, a certified premixed cylinder of (0.983 ± 0.0197)% NH_3, 13.5% He and 85.52% H_2 was used for many of the measurements. These cylinders and similar mixtures were provided by both Matheson Tri-Gas, Inc. and Airgas, Inc. No attempt was made to characterize the opacity of ammonia broadened only by hydrogen or helium due to time constraints, but the behavior of each individually as a broadening gas is fairly well understood from measurements by other authors.

A total of 3191 data points of the opacity of NH_3 were measured with each point representing a unique combination of temperature, pressure, NH_3 concentration and frequency. Of these, only 1912 came from reliable resonances and provided consistent opacity data. The other 1279 points were identified by eye and excluded due to any number of contributing factors, most often for modes where $N \neq 0$. Other reasons for exclusion include interference from overlapping resonances, usually under high-opacity conditions, and low signal to noise ratios. The population of usable resonances

throughout the measured frequency range is large enough such that the bad data points can be ignored without greatly affecting the accuracy of the derived model. The unused data are cataloged along with the good data as they may provide useful refractivity data for future applications. An additional 250 data points were taken using the Fabry-Perot resonator and provide insight as to the behavior of ammonia at K/K_a-band. Most of the Fabry-Perot data was taken using an HP 8722D network analyzer with a measurement range from 50 MHz to 40 GHz borrowed from colleagues for a month. This provided faster measurement times and greater accuracy, both of which gave insight into the nature of adsorption in the Pyrex® pressure chamber and eventually led to the development of the replace-half technique. All of the processed NH_3 data is too lengthy to list here or as an appendix, so it is available in electronic format at:

http://users.ece.gatech.edu/~psteffes/palpapers/hanley_data/NH3data_ALL.xls

separated by the resonator used. Some plots of the opacity data are shown in section 4.3 (below) compared to previous models for ammonia opacity and the model developed as part of this work. A list of the NH_3 experiments performed in the cavity resonators and Fabry-Perot resonator can be found in Tables 4.3 and 4.4 respectively. The scattering parameters S12 and S21 were recorded for measurements using the network analyzers, but the only the S21 data was processed since both S12 and S21 produce essentially the same result.

Previously, chapter 3 described the current state of the art for the measurement system. Its development has been realized through a number of incremental equipment and procedural changes during the course of the measurements of NH_3. Therefore, many of the early, colder temperature, measurements have additional uncertainties since they

Table 4.3: Listing of all experimental conditions for the measurements of ammonia opacity and refractivity using the cavity resonators performed as part of this work

Experiment Dates	Temp. Range (K)	Nominal Pressures (bar) and {NH_3 concentration (%)}	Resonator Configs.[10]	Upgrades Not Yet Realized
6/18/06 - 8/18/06	184 - 189	0.5{1}, 1{0.65}, 2{0.45}	1,1,1	(1), (2), (3), (4), (5)
7/03/06 - 8/18/06	184 - 189	0.5{1.15}, 1{0.75}, 2{0.49}	1,1,1	(1), (2), (3), (4), (5)
7/07/06 - 8/18/06	184 - 189	0.5{1.8}, 1{1.2}, 2{0.8}	1,1,1	(1), (2), (3), (4), (5)
7/23/06 - 8/18/06	184 - 189	0.5{1.8}, 1{1.15}, 2{0.75}	1,1,1	(1), (2), (3), (4), (5)
8/25/06 - 10/26/06	213 - 218	1{0.98}, 2{0.7}, 4{0.53}, 6{0.42}	1,1,1	(1), (2), (3), (4), (5)
8/31/06 - 11/1/06	213 - 218	1{1.1}, 2{0.82}, 4{0.58}, 6{0.47}	1,1,1	(1), (2), (3), (4), (5)
9/7/06 - 11/3/06	213 - 218	0.06{100}, 1{1.95}, 2{1.4}, 4{1.1}, 6{0.94}	1,1,1	(1), (2), (3), (4), (5)
9/20/06 - 11/2/06	213 - 218	0.125{5}, 0.25{3.7}, 0.5{2.7}, 1{1.85}, 2{1.32}, 4{1}, 6{0.88}	1,1,1	(1), (2), (3), (4), (5)
12/6/06 - 12/15/06	292 - 297	0.125{1.25}, 0.25{1.12}, 0.5{1.05}, 1{0.98}, 2{0.92}, 4{0.89}, 6{0.88}	2,2,2	(3), (4), (5)
1/10/07 - 1/30/07	292 - 297	0.5{0.49}, 1{0.47}, 2{0.44}, 4{0.43}, 6{0.42}	2,2,2	(3), (4), (5)
2/19/07 - 3/5/07	292 - 297	0.25{100}, 0.032{6}, 0.064{5.5}, 0.125{4.8}, 0.25{4.6}, 0.5{4.4}, 1{4.2}, 3{4}, 6{4}	2,2,2	(3), (4), (5)
3/8/07 - 3/18/07	213 - 218	0.5{1.05}, 1{0.95}, 2{0.88}, 4{0.785}, 6{0.77}	2,2,2	(3), (4),(5)
3/31/07 - 4/13/07	292 - 297	0.06{100}, 0.24{100}, 4{0.5}, 6{0.5}, 4{1}, 6{1}, 4{4}, 6{4}	2,2,2	(3), (5)
5/25/07 - 6/1/07	292 - 297	3{0.983}, 4{0.98}, 8{0.95}, 12{0.9}, 4{0.312}, 8{0.282}, 12{0.262}	2,2,2	none
12/6/07 - 12/19/07	372 - 377	0.03{100}, 4{0.94}, 8{0.93}, 12{0.93},4{0.25},8{0.25},12{0.25}	4,1,3	none
1/7/08 - 1/28/08	445 - 450	0.03{100}, 0.12{100}, 0.5{0.97}, 1{0.97}, 2{0.97}, 4{0.92}, 6{0.92}, 8{0.92}, 12{0.92}, 4{0.27}, 8{0.24}, 12{0.229}, 8{0.068}, 12{0.068}	4,1,3	none

[10] The format is as follows from Tables 3.4 and 3.5: large resonator height configuration, small resonator radius configuration and small resonator height configuration respectively.

Table 4.4: Listing of all experimental conditions for the measurements of ammonia opacity and refractivity using the Fabry-Perot resonator performed as part of this work

Experiment Dates	Temp. Range (K)	Nominal Pressures (bar) and {NH_3 concentration (%)}	Mirror Spacing (cm)	Upgrades Not Yet Realized
2/22/07 - 3/7/07	292 - 297	0.25{100}	5.85	(3), (4), (5)
3/28/07 - 4/3/07	292 - 297	1{0.983}, 2{0.983}, 3{0.983}	5.85	(3), (5)
3/31/07 - 4/3/07	292 - 297	0.25{1}, 0.5{1}, 1{1}, 2{1}, 3{1}	5.85	(3), (5)
4/4/07 - 4/9/07	292 - 297	0.0625{4}, 0.125{4}, 0.25{4}, 0.5{4}, 1{4}, 2{4}, 3{4}	5.85	(3), (5)
4/4/07 - 4/11/07	292 - 297	0.24{100}, 0.5{8}, 1{8}, 2{8}, 3{8}	5.85	(3), (5)
4/16/07- 4/22/07	292 - 297	0.25{0.983}, 0.5{0.983}, 1{0.983}, 2{0.983}, 3{0.983}	6.17	(3), (5)
4/24/07 - 4/26/07	292 - 297	0.5{0.5}, 1{0.5}, 2{0.5}, 3{0.5}	6.17	(3), (5)
1/15/08 - 1/28/08	292 - 297	0.5{0.983}, 1{0.983}, 2{0.983}, 3{0.983}	5.85	none

were taken under less accurate conditions. These additional uncertainties are not large enough to justify the time required to repeat the measurements using the current state of the art, especially considering the temperature range of the more accurate measurements. These more precise data at the higher temperatures were sufficient to infer the temperature dependence of ammonia and to produce an accurate model for the ammonia opacity, described in section 4.3, that matched the earlier data well within their error bars.

The major accuracy improvements include: the addition of dielectric spacers in the cavity resonators (1), the closer placement of the mirrors in the Fabry-Perot resonator (2), the acquisition of a second DPG7000 pressure gauge for lower pressures (3), the

identification of adsorption in the Fabry-Perot resonator and the development of the replace-half technique (4), and the tracking of ambient pressure to further calibrate the pressure gauges (5). The addition of the dielectric spacers allowed for more reliable data from more resonances in both cavity resonators, but the improvement in accuracy is difficult to characterize quantitatively. Moving the mirrors closer together in the Fabry-Perot resonator allowed much more accurate characterization of adsorption in the cavity resonators and the identification of adsorption occurring in the Fabry-Perot resonator itself further reduced the uncertainty in NH_3 concentration. Previous measurements were limited to ± 5-10% precision, whereas current measurements are on the order of ± 2%. Adding a second DPG7000 pressure gauge reduced the uncertainty in pressure readings below 2 bars absolute pressure to ± 0.68 mbar from the previous ± 2 mbar uncertainty of the vacuum gauge. Tracking ambient pressures with a barometer allowed achievement of the stated accuracies of the pressure gauges. A ± 10 mbar uncertainty in pressure was added to early measurements due to fluctuations in ambient pressure during the course of an experiment, even after initial calibration of the gauges before the experiment. The lack of these upgrades are noted by number in the last columns of Tables 4.3 and 4.4 for experiments where they occurred.

As shown in Table 4.4, the opacity of the 0.983% NH_3 premixed gas at K/K_a-band was measured at multiple pressures and two mirror positions. These measurements from early April 2007 were performed when the premixed gas cylinder was mostly full. That cylinder was used frequently over the following months for measurements using the cavity resonators and another set of measurements in the Fabry-Perot resonator were performed just before the cylinder was emptied in January 2008. The two results were

consistent meaning that the NH_3 concentration in the cylinder did not change with partial pressure or settling over time. This is due primarily to the anti-adsorption coating present on the inside of the cylinder.

4.1.2 Water Vapor

The number of measurements of the opacity of H_2O in an H_2/He atmosphere is significantly less than those performed using NH_3. This is due to two compounding factors, the lower opacity of H_2O relative to NH_3 and the lower saturation vapor pressure of H_2O. In order to raise the opacity of the H_2O gas mixture to the level of detectability, fairly large partial pressures of H_2O must be used. These pressures are only attainable at temperatures well above room temperature. It would be possible to measure the opacity of H_2O broadened by H_2/He at room temperature, but it would require H_2/He pressure on the order of 100 bars, well above the rated limits of the current pressure vessel. Therefore, measurements were taken in the temperature bands of 350-352 K, 372-377 K and 447-451 K using the cylindrical cavity resonators. This led to the measurement of only 222 data points of the opacity and refractivity of H_2O. Other attempts were made at measuring water vapor at 100% relative humidity at room temperature in 3 bars of H_2/He at K/K_a-band in the Fabry-Perot resonator and in 12 bars of H_2/He in the cavity resonators, but no significant opacity was detected. The list of the warmer experimental conditions is shown in Table 4.5. To avoid the possibility of condensation occurring in the resonators, the partial pressure of water vapor was always kept below 70% of saturation and usually below 50%.

Table 4.5: Listing of all experimental conditions for the measurements of water vapor opacity and refractivity using the cavity resonators performed as part of this work

Experiment Dates	Temp. Range (K)	Nominal Pressures (bar) and {NH_3 concentration (%)}	Resonator Configs.
10/23/07 - 10/31/07	350 - 352	0.3{100}, 4{7.3}, 8{3.8}, 12{2.5}	3,1,3
11/4/07 - 11/6/07	372 - 377	0.35{100}, 8{4.3}	3,1,3
2/5/08 - 2/13/08	447 - 451	0.57{100}, 1{100}, 4{14}, 8{7.1}, 11.1{5.1}, 4{26}, 8{13}, 11{9.5}	4,1,3

Like the NH_3 opacity data, the H_2O opacity data measured as part of this work is too numerous to list on paper and is available in electronic form at:

http://users.ece.gatech.edu/~psteffes/palpapers/hanley_data/H2Odata_ALL.xls

As with ammonia, the data is separated by the cavity resonator used. The refractivity of some of the H_2O mixtures was so large that dielectrically matching the measurements would have required pressures of argon exceeding the safe operating pressure of the vessel. For those measurements, the values of $Q_{matched}$ and $t_{matched}$ in equation 3.17 were replaced with the vacuum values, Q_{vac} and t_{vac}, since the Q's of the resonators did not change significantly from vacuum with the addition of argon. For the measurements near 450 K, the transmissivities of the cables used in the H_2O opacity calculations are the same as those from NH_3 measurements in the same temperature range. This was done to eliminate addition disconnection and reconnection of the cables, which at those temperatures became prone to the connectors shearing apart from the cables.

The relative size of the measurement uncertainties and the small amount of data do not allow for the development of an improved model for H_2O opacity at this point. Further data are needed, taken at higher pressures where the opacity is greater. Some of the measured H_2O opacity data is plotted in Figures 4.1 – 4.6 compared with the models of DeBoer (de Pater *et al.* 2005) and Goodman (1969). For measurements of pure H_2O without H_2 or He, the Goodman model equates to an opacity of zero since it does not include the effect of the self-broadening of H_2O and is not included in those plots. The dashed lines about the models show the variability of the modeled values due to uncertainties in the measurements of pressure, temperature and H_2O concentration. The black error bars represent only the values of Err_α. Error bars are shown without data points when the data have negative values and many error bars from positive data span values below zero. The data show that the DeBoer model underestimates the effect of the self-broadening of H_2O, which appears to be dominant even where the concentration of H_2O is only on the order of ten percent. When the H_2O concentration is lowered and higher pressures of H_2/He are added, the DeBoer model appears to overstate the opacity. Based on the data, the Goodman model appears to function as a lower limit for the H_2/He broadened opacity of H_2O.

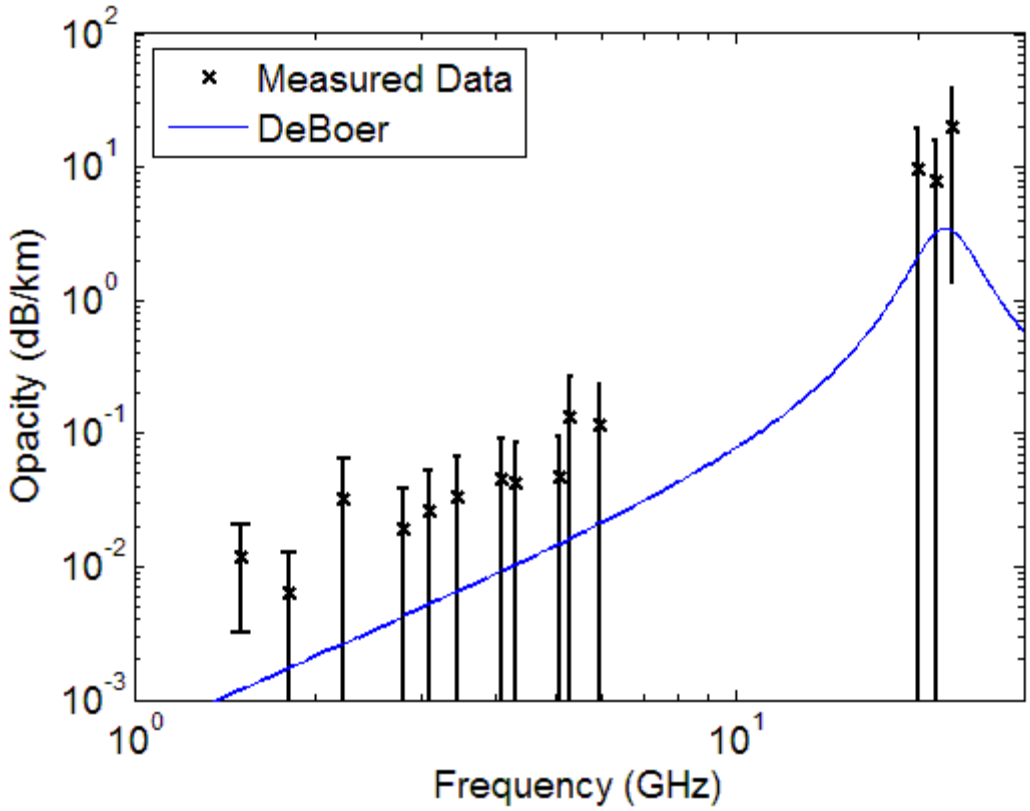

Figure 4.1: Measured opacity of 0.303 bar of pure water vapor at a temperature of 350.5 K.

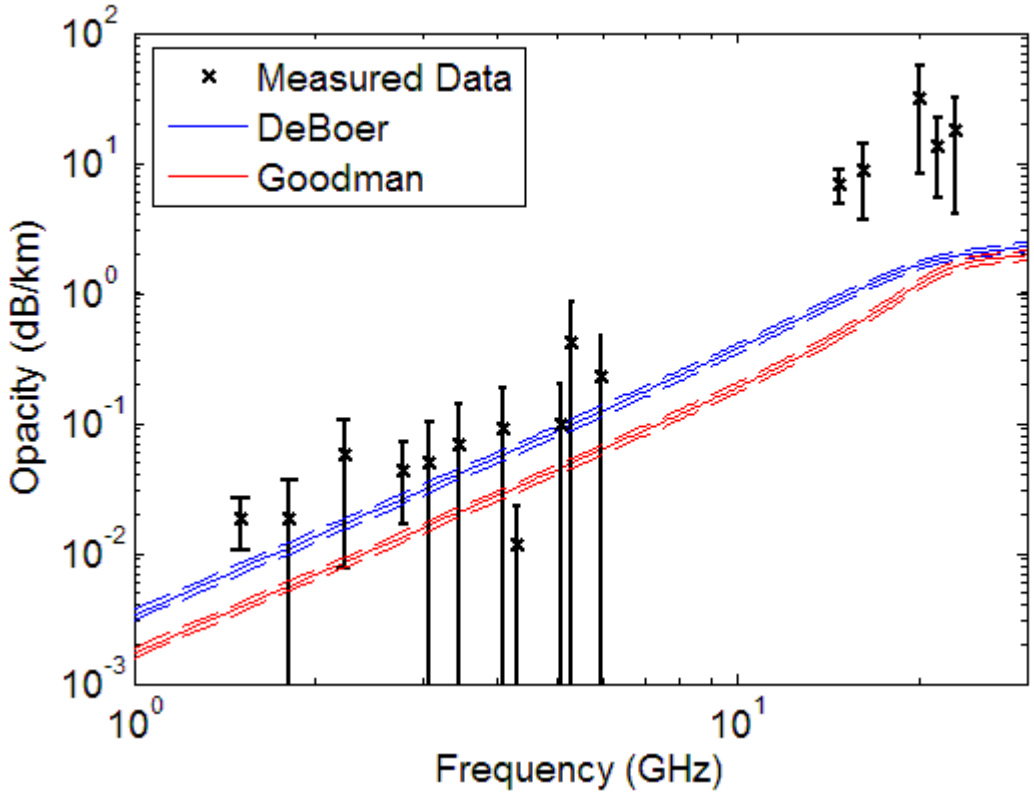

Figure 4.2: Measured opacity of water vapor broadened by hydrogen and helium at 4.033 bar of pressure and a temperature of 351.6 K (H_2O = 7.29%, He = 12.61% and H_2 = 80.1%).

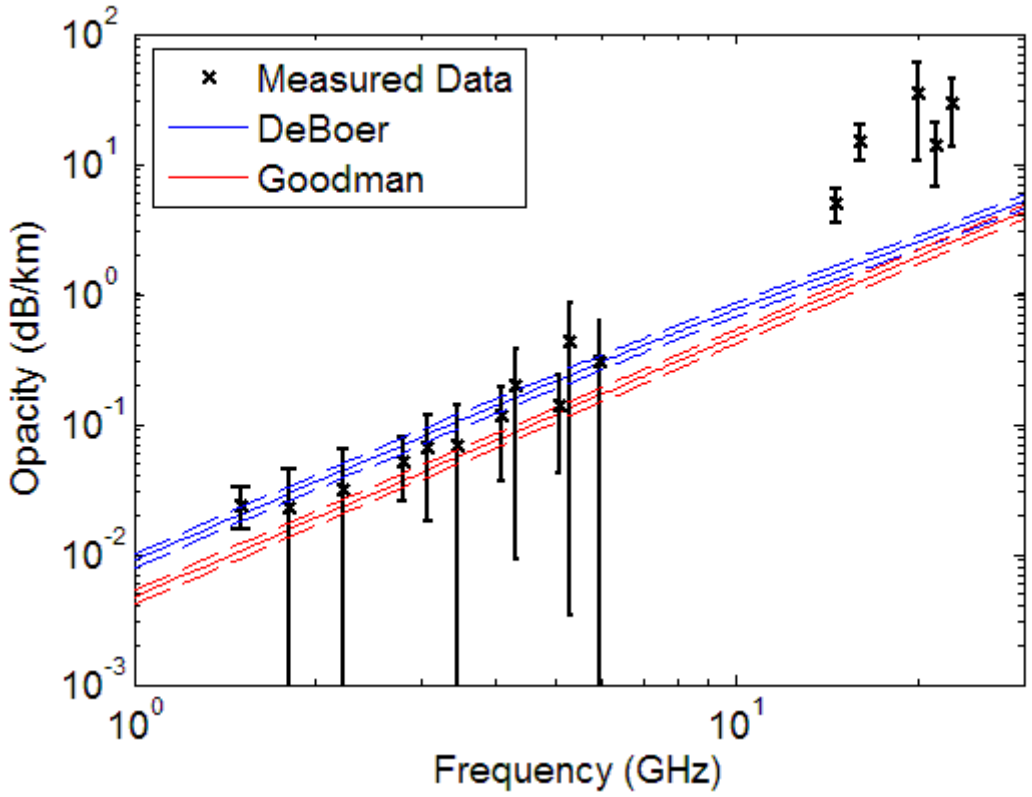

Figure 4.3: Measured opacity of water vapor broadened by hydrogen and helium at 11.676 bar of pressure and a temperature of 351.7 K (H_2O = 2.45%, He = 13.27% and H_2 = 84.28%).

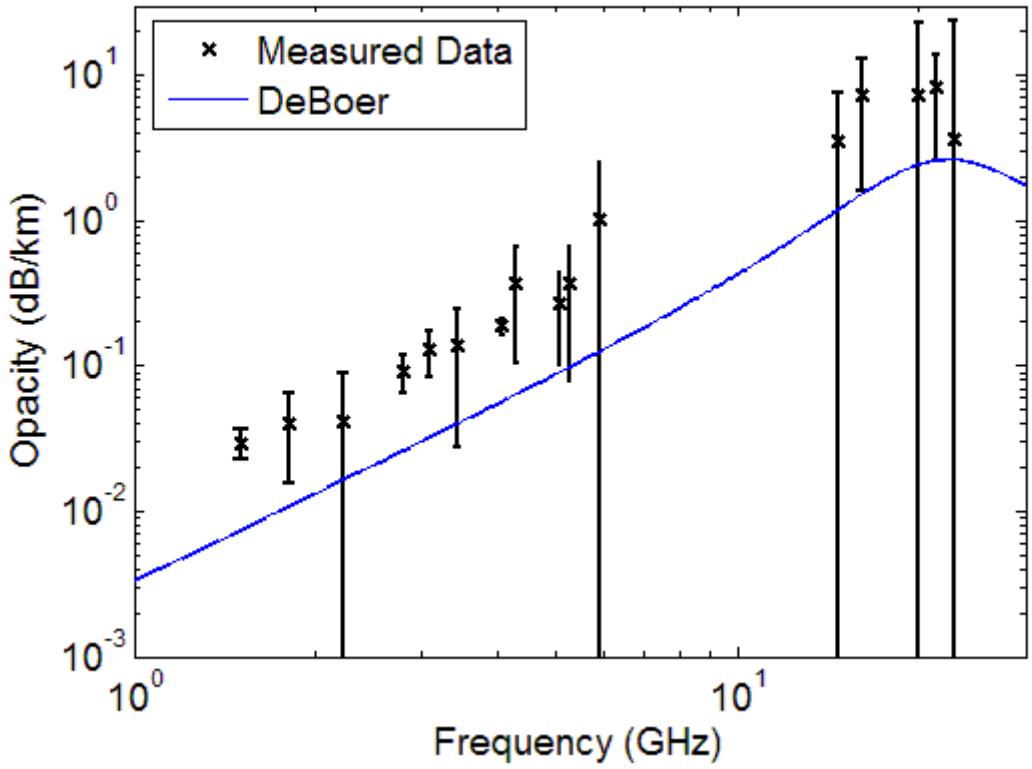

Figure 4.4: Measured opacity of 1.041 bar of pure water vapor at a temperature of 448.2 K.

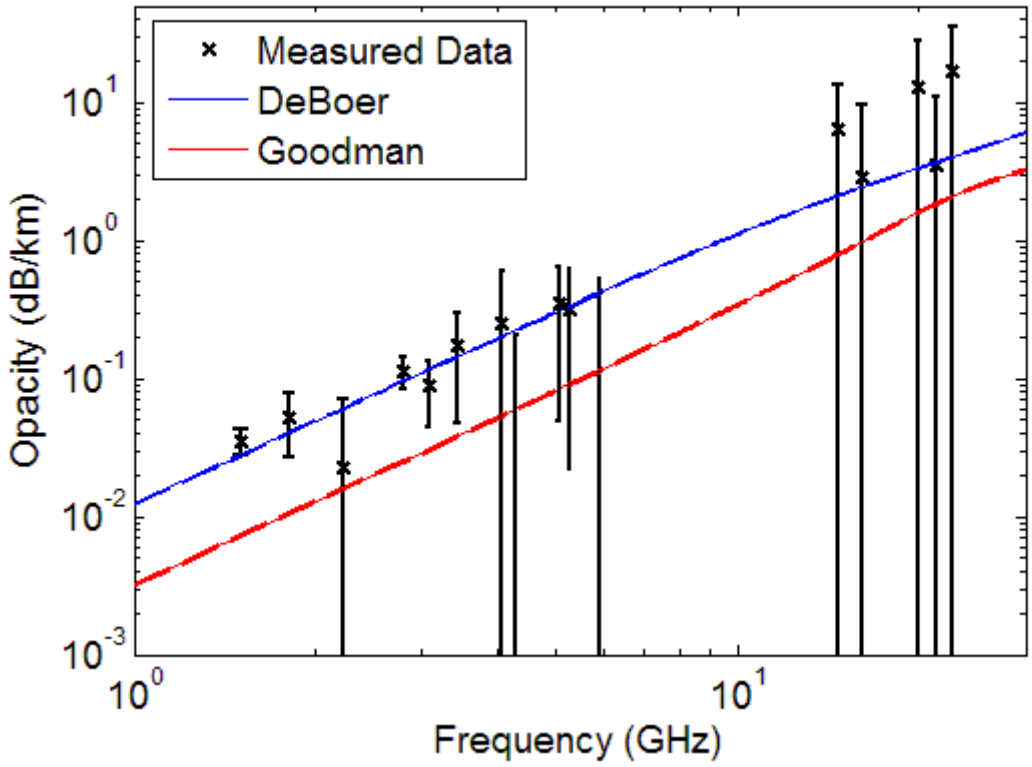

Figure 4.5: Measured opacity of water vapor broadened by hydrogen and helium at 7.965 bar of pressure and a temperature of 450.2 K (H_2O = 13.07%, He = 11.82% and H_2 = 75.11%).

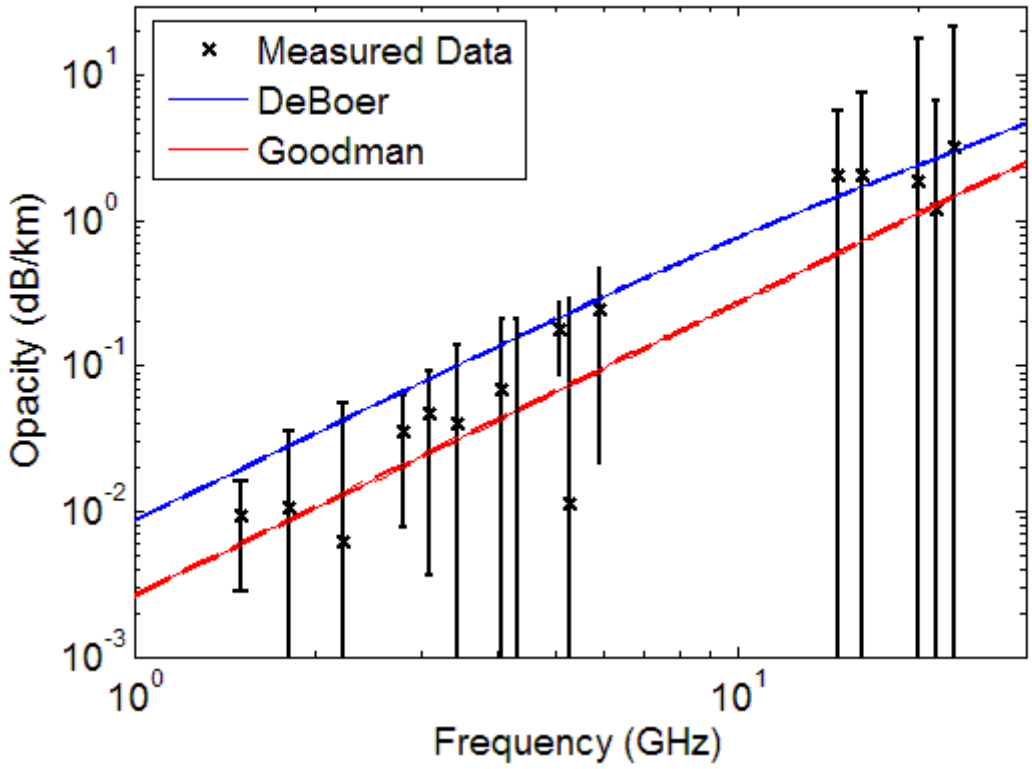

Figure 4.6: Measured opacity of water vapor broadened by hydrogen and helium at 11.129 bar of pressure and a temperature of 448.3 K (H_2O = 5.11%, He = 12.9% and H_2 = 81.98%).

4.2 Data Fitting

Measuring the microwave opacity of NH_3 and H_2O in a laboratory setting provides a means of proving or disproving current theories and models. All previous models for the H_2/He broadened opacity of NH_3 and H_2O under Jovian conditions are based on limited and often flawed laboratory data. With the aid of more precise wider-ranging data, it is possible to not only detect the usable ranges of certain models, but also develop more accurate ones. The goal of the laboratory measurements of ammonia is to create a model that will predict the opacity of NH_3 equally well over a diverse range of conditions.

The large amount of measured data on the opacity of ammonia spans temperatures ranging from 187 to 450 K, pressures from 29.7 mbar to 12.07 bar, and NH_3 concentrations as low as 676 ppm up to 8% and even a handful of measurements of 100% NH_3. Measurement frequencies range from 1.5 to 27 GHz using the cavity resonators and from 22.2 to 39.2 GHz using the Fabry-Perot resonator. This data spans a large four-dimensional space of frequency, temperature, pressure and NH_3 concentration, but the data are not equally distributed in this space. Due to the behavior of the resonators, close to three quarters of the usable data was measured at frequencies below 10 GHz. More data was also measured at room temperature than any other temperature, especially the K/K_a-band data from the Fabry-Perot resonator that was measured exclusively at room temperature. The measurements at colder temperatures were limited to lower concentrations of NH_3 in order to avoid condensation. Also, the sensitivity at lower frequencies was not high enough to detect NH_3 at the lowest pressures and the higher frequency resonances were not accurate enough to measure large opacities of NH_3 to high precision.

To prevent the accuracy of the derived model from being skewed toward the most often measured conditions, each data point must be scaled relative to the uniqueness of its four measurement variables: frequency (f), temperature (T), pressure (P) and NH_3 concentration (C) or mole fraction. The approach used divides each of these variables in roughly equally spaced bins that span the measurement space. The total number of measurements that fall into each bin are counted and then each data point is weighted by the sum of the reciprocals of the counts of the bins corresponding to its four measurement variables. Of the 1912 data points using the cavity resonators, 481 points corresponding to data from the first 8 experiments listed in Table 4.3 were not used in the data fitting due to their relatively large uncertainties in NH_3 concentration from upgrades not implemented at the time of the measurements. These 481 points were compared to the model derived from the rest of the data, and both the NH_3 concentrations and opacities agreed well with the theoretical nature of adsorption and desorption that occurred during the experiments. For the remaining 1431 points, the *fTPC* space is broken down as shown in Table 4.6.

Once the population of each bin was established, each individual data point received a data weight (DW) value according to

$$DW = \frac{1}{f_{count}} + \frac{1}{T_{count}} + \frac{1}{P_{count}} + \frac{1}{C_{count}}, \tag{4.1}$$

where f_{count}, T_{count}, P_{count}, and C_{count} represent the values of the entries in Table 4.6 for the conditions of the data point. These DW values were then utilized in fitting a model to the data. The data-fitting routine involved using a multi-variable simplex function similar to that of Hoffman *et al*. (2001) to minimize the value of

Table 4.6: The breakdown of the utilized NH_3 data in the *fTPC* space

Frequency Range (GHz)	$0 \le f < 5$	$5 \le f < 10$	$10 \le f < 15$	$15 \le f < 20$	$20 \le f < 25$	$25 \le f < 30$
f_{count}	556	455	106	122	192	0
Temperature Range (K)	$150 \le T < 200$	$200 \le T < 250$	$250 \le T < 300$	$300 \le T < 350$	$350 \le T < 400$	$400 \le T < 450$
T_{count}	0	150	973	0	112	196
Pressure Range (bar)	$0 \le P < 0.26$	$0.26 \le P < 0.51$	$0.51 \le P < 1.1$	$1.1 \le P < 2.1$	$2.1 \le P < 4.1$	$4.1 \le P < 8.1$	$8.1 \le P < 16$
P_{count}	215	108	159	118	337	351	143
Concentration Range (%)	$0 \le C < 0.3$	$0.3 \le C < 0.6$	$0.6 \le C < 1.0$	$1.0 \le C < 2.5$	$2.5 \le C < 4.5$	$4.5 \le C \le 100$
C_{count}	174	266	518	107	161	205

$$\sum_{n=1}^{1431} \frac{\left(\alpha_n^{meas} - \alpha_n^{model}\right)^2}{\left(Err_{\alpha}^{meas} + Err_{cond}^{meas}\right)^2} \times DW \,, \tag{4.2}$$

where α_n^{meas} and α_n^{model} represent the measured and modeled opacity values respectively and Err_{α}^{meas} and Err_{cond}^{meas} are the 2σ uncertainties in measured opacity and measurement conditions as described in section 3.4.2. The constrained minimum of this function was calculated using the Matlab® function *fmincon* multiple times using random input values (described in the next section) until a convergent solution was found. The Err_{cond}^{meas} values were initially calculated using the temperature, pressure and concentration dependences of the Joiner and Steffes (1991) NH_3 opacity model, since it matched the data closer than any other previous model. After the initial optimization resulted in the formalism described in section 4.3, the Err_{cond}^{meas} values were recalculated and an additional iteration of equation 4.2 was executed, but the optimized model did not show any significant changes.

The 250 NH_3 data points taken using the Fabry-Perot resonator were not used since they represented only data above 25 GHz and were all taken at room temperature. Even using the data weighting in this case would skew the resulting model toward better agreement at room temperature. The model derived from the measurements using the cavity resonator was, however, compared to the data from the Fabry-Perot resonator and found to be in comparable or better agreement than the other frequently used NH_3 models as shown in section 4.3.

For the water vapor experiments of this work, there is insufficient data to derive a more accurate model for H_2/He broadened H_2O opacity as was mentioned in the previous section. A cursory attempt was made at refining some of the broadening parameters, but the results required self-broadened linewidths on the order of three times that measured by other researchers and still did not follow the temperature dependence of the data. Attempts were made at fitting with both the Gross and Van Vleck-Weisskopf lineshapes, and the Gross lineshape fit the data better. As more data becomes available from future higher-pressure measurements, then the extra parameters of the Ben-Reuven lineshape can be applied.

4.3 New Model for H_2/He-broadened NH_3 Microwave Opacity

The new model for the hydrogen and helium broadened opacity of ammonia at frequencies up to 40 GHz is a refinement of previous models by Berge and Gulkis (1976) and Mohammed and Steffes (2003). The model calculates the opacity at a given frequency, temperature, pressure, and concentration of H_2, He and NH_3 by summing the

individual contributions of each NH_3 inversion line up to $J = K = 19$. The opacity from each line at a frequency of f can be written as

$$\alpha_{J,K}(f) = A_{J,K}\pi\Delta f_{J,K}\left(\frac{f}{f_0(J,K)}\right)F_{BR}D\,, \tag{4.3}$$

where $A_{J,K}$ is the absorption at the center of the J, K line, $\Delta f_{J,K}$ is the linewidth (half width at half max), $f_0(J,K)$ is the center frequency of the J, K line, F_{BR} is the Ben-Reuven (1966) lineshape as defined in equation 2.6, and D is a unitless empirically derived scale factor. The absorption at the line center in units of cm^{-1} is calculated by

$$A_{J,K} = \frac{nS_{J,K}(T)}{\pi\Delta f_{J,K}}\,, \tag{4.4}$$

where n is the number density of ammonia in molecules/cm^3 and $S_{J,K}(T)$ is the intensity of the J, K line in cm^{-1}/(molecule/cm^2) at a temperature T with $\Delta f_{J,K}$ having units of cm^{-1}. Assuming ideal gas behavior, n in units of molecules/cm^3 can be calculated as

$$n = 7.244\times10^{21}\frac{P_{NH_3}}{T}\,, \tag{4.5}$$

where P_{NH_3} is the partial pressure of ammonia in bar and T is the temperature in K. The line intensities are calculated as

$$S_{J,K}(T) = S_{J,K}(T_0)\left(\frac{T_0}{T}\right)^{5/2} e^{(1/T_0 - 1/T)E''_{J,K}hc/k}\,, \tag{4.6}$$

where $S_{J,K}(T_0)$ is the intensity of the line at the reference temperature T_0, T is the temperature in kelvin, $E''_{J,K}$ is the lower state energy of the transition in cm^{-1} and h, c, and k are Plank's constant in units of J·s, the speed of light (cm/s), and Boltzmann's constant (J/K) respectively. For these units, $hc/k = 1.439$. The values of $f_0(J,K)$, $S_{J,K}(T_0)$ and $E''_{J,K}$ at the reference temperature of 300 K for lines up to $J = K = 19$ can be found in the JPL

Submillimeter, Millimeter, and Microwave Spectral Line Catalog described in Pickett *et al*. (1998). The values of $S_{J,K}(T_0)$ given in the catalog have units of $\log_{10}(\text{nm}^2\cdot\text{MHz})$ and must be taken as the exponent of 10 and divided by 2.99792458×10^{18} to be utilized in equations 4.4 and 4.6. The total opacity in cm^{-1} is then calculated using the Ben-Reuven lineshape (1966) as

$$\alpha_{NH_3}(n,T,f)=\frac{2Dn}{\pi}\sum_{J=1}^{19}\sum_{K=1}^{J}S_{J,K}(T)\left(\frac{f}{f_0(J,K)}\right)^2\frac{(\gamma-\zeta)f^2+(\gamma+\zeta)\left[(f_0(J,K)+\delta)^2+\gamma^2-\zeta^2\right]}{\left[f^2-(f_0(J,K)+\delta)^2-\gamma^2+\zeta^2\right]^2+4f^2\gamma^2}, \quad (4.7)$$

where γ, ζ, and δ are the linewidths, coupling parameters, and shift parameters respectively of each line in units of cm^{-1}. The width and coupling parameter of each pressure-broadened line are the sums of the contributions of each component of the gas mixture and are calculated by

$$\gamma=\gamma_{H_2}P_{H_2}\left(\frac{300}{T}\right)^{\Gamma_{H_2}}+\gamma_{He}P_{He}\left(\frac{300}{T}\right)^{\Gamma_{He}}+\gamma_{NH_3}\gamma_0(J,K)P_{NH_3}\left(\frac{295}{T}\right)^{\Gamma_{NH_3}} \quad (4.8)$$

$$\zeta=\zeta_{H_2}P_{H_2}\left(\frac{300}{T}\right)^{Z_{H_2}}+\zeta_{He}P_{He}\left(\frac{300}{T}\right)^{Z_{He}}+\zeta_{NH_3}\gamma_0(J,K)P_{NH_3}\left(\frac{295}{T}\right)^{Z_{NH_3}}, \quad (4.9)$$

where γ_i and ζ_i are constant scale terms, Γ_i and Z_i represent the constant temperature dependences of the broadening of each gas and P_i are the partial pressures in bar for i = H_2, *He* and NH_3 and $\gamma_0(J,K)$ are the self-broadening linewidths of NH_3 in MHz/torr. Unlike the Berge and Gulkis NH_3 model in which the pressure shift term is proportional to the partial pressure of NH_3, δ is calculated here as

$$\delta=d\times\gamma \quad (4.10)$$

similar to the lineshape of Anderson (1949) where d is an empirically derived constant. Equations 4.8, 4.9, and 4.10 have been simplified to use average values of the empirically derived constant for all lines, even though each line behaves differently, as measured by

various researchers (Buffa *et al.* 1979; Hewitt 1977; Nouri *et al.* 2004; Story *et al.* 1971). The reason for this simplification is that not enough accurate data exists on the behavior of each NH_3 line and no one pressure broadening theory has been able to match all of the various experimentally measured data. The values of $\gamma_0(J,K)$ used in equations 4.8 and 4.9 are from the calculations of Poynter and Kakar (1975) assuming a T_0 value of 295 K using the theory of Anderson (1949). Poynter and Kakar do not list the linewidths for values of J > 16 or for lines with center frequencies below 7.2 GHz. For these unlisted lines, $\gamma_0(J,K)$ is calculated as

$$\gamma_0(J,K) = 25.923 \frac{K}{\sqrt{J(J+1)}} \text{ (MHz/torr).} \tag{4.11}$$

The linewidth values generated by equation 4.11 agree well with those measured for higher values of *J*, but do not agree with the values for lower numbered *J* lines. An attempt was made to match the linewidths calculated by Poynter and Kakar (1975) using the Anderson theory, but the authors do not provide enough information as to the precise method used. However, the linewidths given by Poynter and Kakar do fit the data more accurately than using equation 4.11 alone for all of the lines or the simplified formula described in Bleaney and Penrose (1948).

The previously listed equations have fourteen free parameters that must either be determined empirically or theoretically. Since the broadening effects of hydrogen and helium were not measured separately, the H_2 and He scale terms in equations 4.8 and 4.9 cannot be decoupled. Therefore the exponents Γ_{He} and Z_{He} are assigned theoretical values of 2/3 and the values of γ_{He} and ζ_{He} are assigned those of the Berge and Gulkis (1976) formalism, 0.75 and 0.3 respectively. The value of Γ_{NH_3} is assigned a

theoretically determined value of 1, which is also fairly consistent with the results of Baldacchini *et al*. (2000) for the ν_2 NH_3 vibrational band. The nine remaining constants were determined by the optimization of the data-fitting equation (4.2). The values of γ_{NH_3}, ζ_{NH_3} and Z_{NH_3} were further constrained by considering only the experiments involving pure ammonia gas. To save on computing time, random samples of 400 of the 1431 data points were used in calculations to find the values of the broadening parameters, linewidths, and pressure shift term, although the model was optimized for all 1431 points after the initial constants were better constrained. The constants were optimized for linewidth and shift units of GHz/bar with pressures given in bar and temperatures in K. The units of $\gamma_0(J,K)$ remain in MHz/torr, since their conversion to GHz/bar is included in the terms of γ_{NH_3} and ζ_{NH_3}. The frequencies of the absorption and line centers are used with units of GHz, which requires scaling the result of equation 4.7 by 29.979 to convert the lineshape from units of GHz^{-1} to cm. This produces values of opacity in units of cm^{-1}, which can be converted to dB/km by multiplying by 4.343×10^5. The values of the 14 constants used in the new formalism are shown in Table 4.7. Since the constants are optimized to the current line catalog values, a spreadsheet of these values has been archived at

http://users.ece.gatech.edu/~psteffes/palpapers/hanley_data/NH3lincat190.xls

in the event that the catalog is ever changed or updated. Software for running the model in Matlab® is available at

http://users.ece.gatech.edu/~psteffes/palpapers/models.html

Some caution must be exercised when using the ideal gas assumption of equation 4.5 at higher pressures since gases are hardly ideal under deep Jovian atmospheric

Table 4.7: Values of the constants used in the new model for H_2/He-broadened NH_3 absorption.

	$i = H_2$	$i = He$	$i = NH_3$
γ_i	1.640	0.75	0.852
Γ_i	0.7756	2/3	1
ζ_i	1.262	0.3	0.5296
Z_i	0.7964	2/3	1.554
$d = -0.0498$		$D = 0.9301$	

conditions. The assumptions of the ideal gas law that molecules have zero volume and no intermolecular forces begin to break down at higher pressures and for large concentrations of polar molecules. As an example, assuming an ideal gas would over-estimate the number of hydrogen molecules present by 6.5% at 100 bar of pressure and by 73% at 1000 bars at 300 K compared to the Redlich-Kwong equation of state (Redlich and Kwong 1949). The difference is slightly lesser under Jovian conditions, 4.2% at 100 bar and 500 K and 18% at 1000 bar and 1250 K. Since the extrapolation of the formalism of this work to pressures higher than 20 bar will have limited accuracy due to the lack of data at those pressures, the ideal gas assumption of equation 4.5 is used here throughout all calculations.

Assessing the fit of the model to the data provides clues as to the quality of the model and the conditions of its effectiveness. For the 1431 data points used to generate the model, 96.1% of them agree with the model within the value of their 2σ uncertainties and 75.1% within 1σ. For the 250 points taken using the Fabry-Perot resonator, 85.2% agree within their 2σ uncertainties and 66.4% within 1σ. Comparisons of these values with the models of Berge and Gulkis (1976), Spilker (1990), Joiner and Steffes (1991), and Mohammed and Steffes (2003) can be seen in Table 4.8. Plots comparing some of

the data to the models can be seen in Figures 4.7 through 4.19. The error bars on the data shown include both the conditional uncertainty values (Err_{cond}) and the measurement uncertainties (Err_{α}). Since the amount of measured data is too large to allow display of a plot for each experiment, the results shown focus on the pressure-temperature points nearest to those found on Jupiter, with the exception of pure NH_3 measurements and those taken with the K/K_a-band Fabry-Perot resonator. The Mohammed and Steffes (2003) model is omitted from plots of the measurements with the cavity resonators since it is only specified to work between 32 and 40 GHz.

The various models for NH_3 opacity are fairly complex, and as a result their respective software realizations can be prone to errors. Additionally, the descriptions of the models given by Joiner and Steffes (1991) and Joiner (1991) are inconsistent and certain assumptions had to be made as to the units employed and the true formulas utilized. In this case, the simple qualitative description provided by Joiner and Steffes (1991) is used. Despite many attempts and permutations of possible errors, this author was unable to exactly reproduce the numerical results of that model as tabulated by Joiner (1991) and Joiner and Steffes (1991). The results are typically 1 to 3% higher than those tabulated previously. Spilker (1990) and Berge and Gulkis (1976) provide plots of their models, but do not provide any numerical results for comparison. Therefore, numerical values of modeled results at various conditions as calculated by this author have been provided in Table 4.9 for cross-reference. The software realizations of each model are also available for reference in Matlab® code format online at:

http://users.ece.gatech.edu/~psteffes/palpapers/models.html

Table 4.8: The percentage of the data measured as part of this work that fits the various NH_3 opacity models within *1σ* and *2σ* uncertainties

NH_3 Opacity Model	Cavity Resonators (1.5 – 27 GHz)		Fabry-Perot Resonator (22 – 40 GHz)	
	1σ Uncertainty	*2σ* Uncertainty	*1σ* Uncertainty	*2σ* Uncertainty
Berge and Gulkis	34.9%	53.1%	64.4%	89.2%
Spilker	46.7%	70.2%	28.4%	48.4%
Joiner and Steffes	60.2%	82.9%	70.4%	84.4%
Mohammed and Steffes	32.9%	57.2%	41.6%	55.2%
This work	75.1%	96.1%	66.4%	85.2%

Table 4.9: The numerical results of various models for ammonia opacity calculated at a frequency of 5 GHz for a mixture of 1% NH_3, 13.5% He and 85.5% H_2. Listed from top to bottom in each cell are the results of this work, Berge and Gulkis (1976), Joiner and Steffes (1991), Mohammed and Steffes (2003) and Spilker (1990). *The Spilker model under these conditions results in a complex opacity. Shown is the real part of the modeled opacity.

P (bar) \ *T* (K)	150	300	450
1.0	1.8319 2.3757 1.7325 1.4154 1.4817	0.27492 0.39547 0.28830 0.23884 0.28228*	0.096364 0.14400 0.10538 0.090597 0.11122*
6.0	51.880 58.720 47.397 39.316 38.961	8.9294 11.788 9.1039 7.5653 10.026	3.1558 4.4382 3.3888 2.8659 3.4030
12.0	125.81 129.10 114.54 96.875 90.622	27.054 32.518 27.306 22.892 26.650	10.372 13.417 10.958 9.2689 9.9645

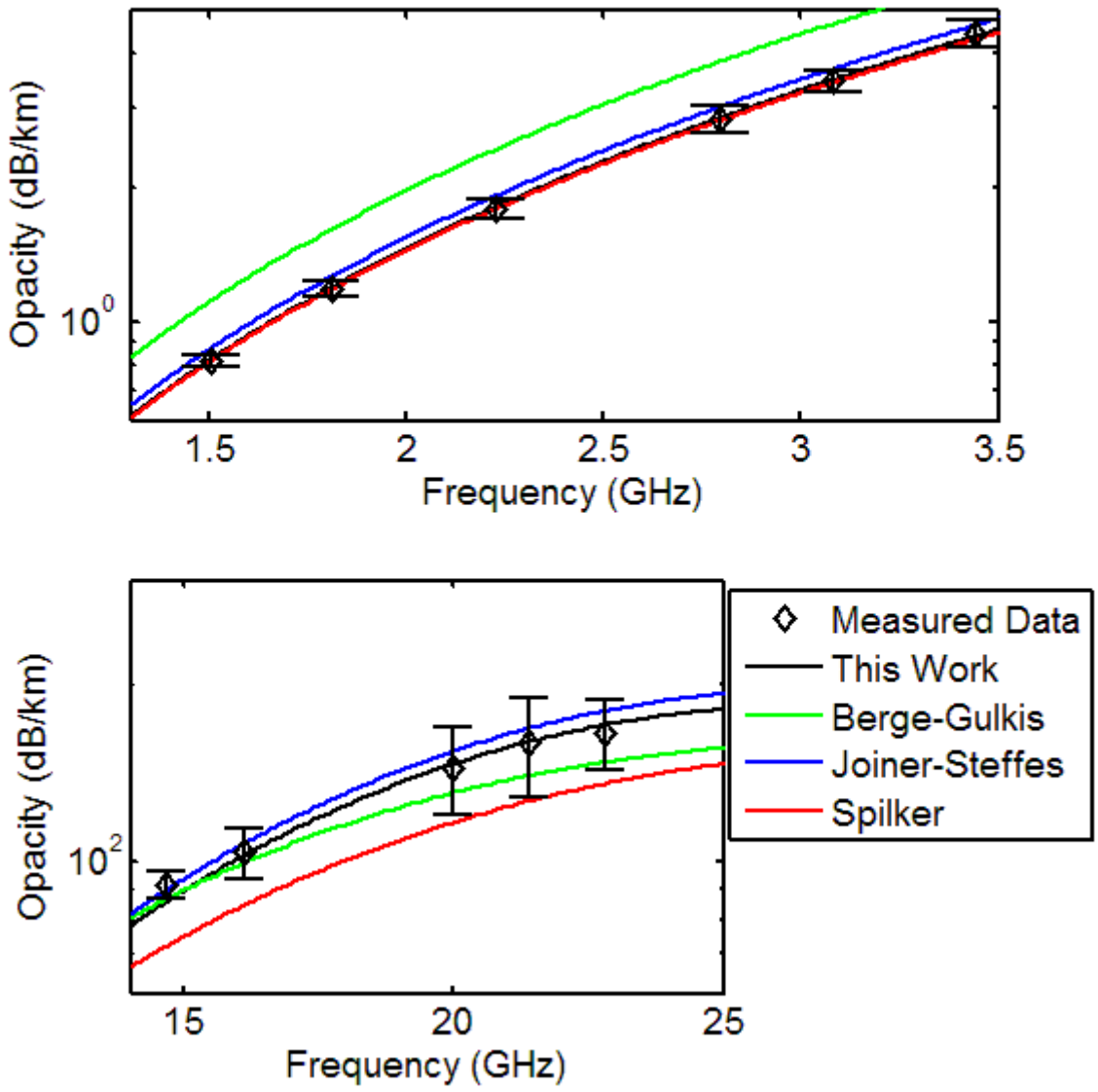

Figure 4.7: Opacity data measured using the large cavity resonator (above) and small cavity resonator (below) for a mixture of NH_3 = 0.92%, He = 13.47%, H_2 = 85.61% at a pressure of 11.742 bar and temperature of 448.4 K compared to various models. The models from this work and Spilker overlap in the plot from the large cavity resonator.

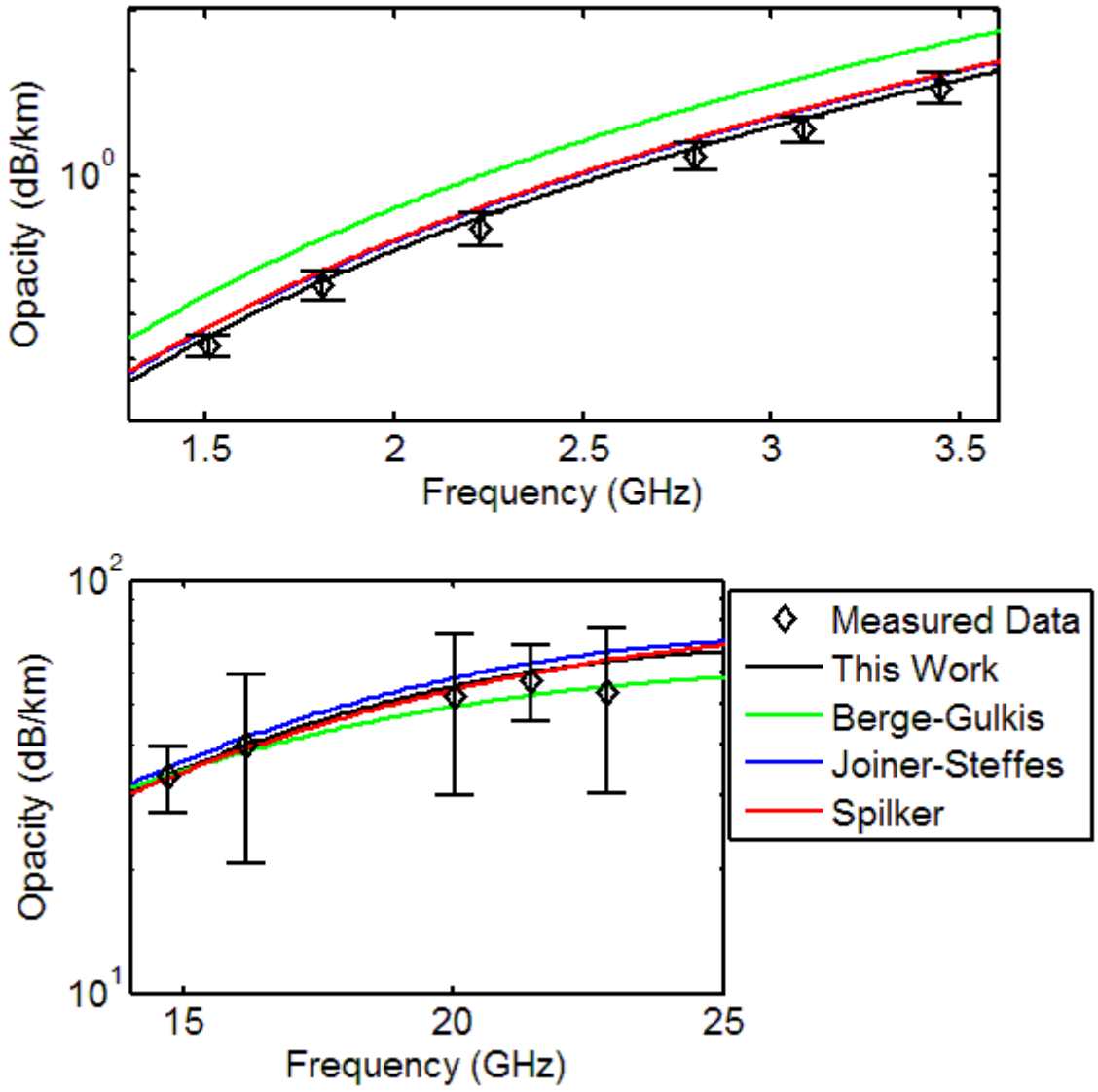

Figure 4.8: Opacity data measured using the large cavity resonator (above) and small cavity resonator (below) for a mixture of NH_3 = 0.25%, He = 13.57%, H_2 = 86.19% at a pressure of 11.896 bar and temperature of 373.7 K compared to various models. The models of Joiner-Steffes and Spilker overlap in the plot from the large cavity resonator.

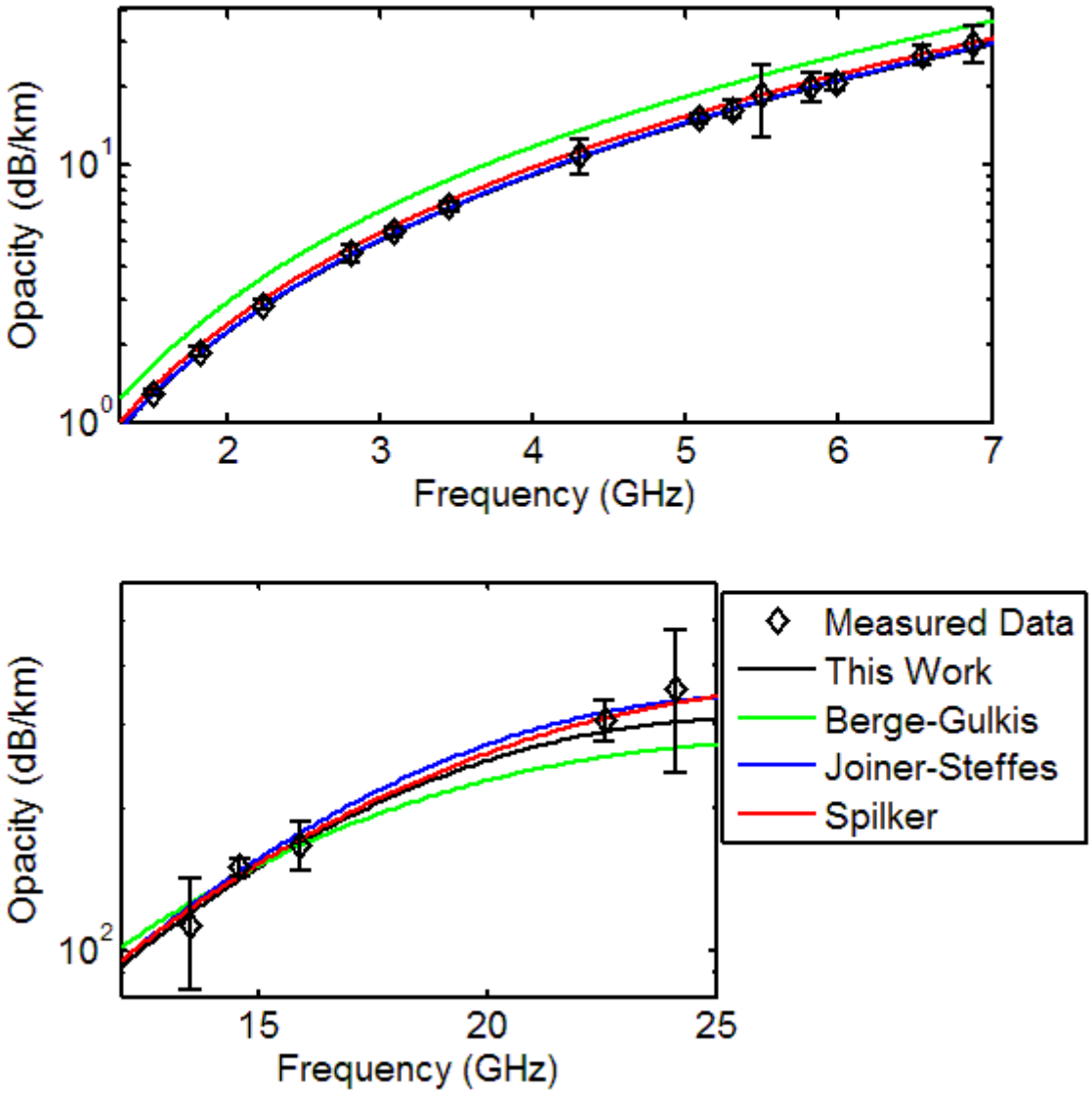

Figure 4.9: Opacity data measured using the large cavity resonator (above) and small cavity resonator (below) for a mixture of NH_3 = 0.95%, He = 13.47%, H_2 = 85.58% at a pressure of 8.0 bar and temperature of 295.5 K compared to various models. The models from this work and Joiner-Steffes overlap in the plot from the large cavity resonator.

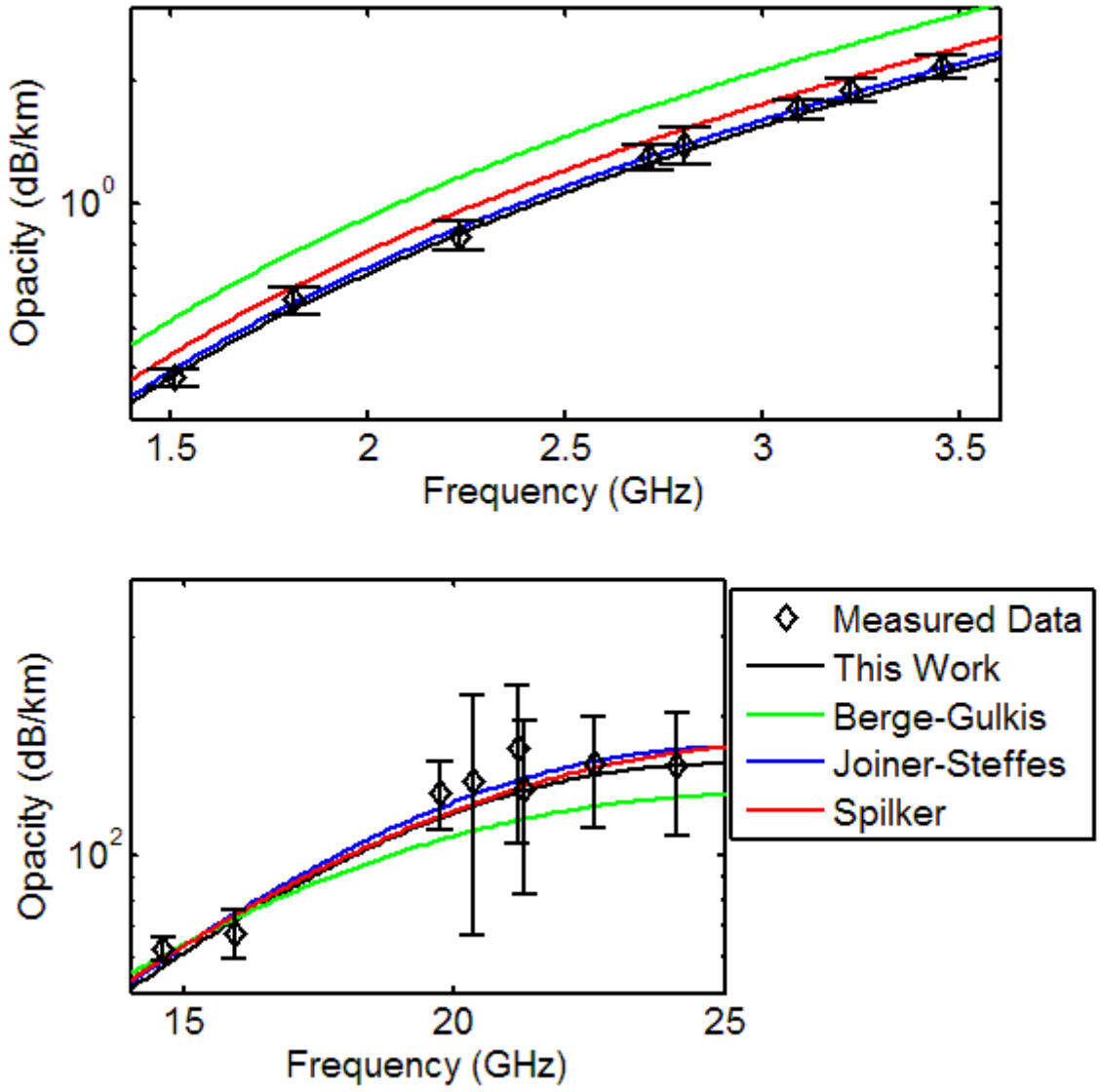

Figure 4.10: Opacity data measured using the large cavity resonator (above) and small cavity resonator (below) for a mixture of NH_3 = 0.5%, He = 13.53%, H_2 = 85.97% at a pressure of 6.0 bar and temperature of 295.8 K compared to various models.

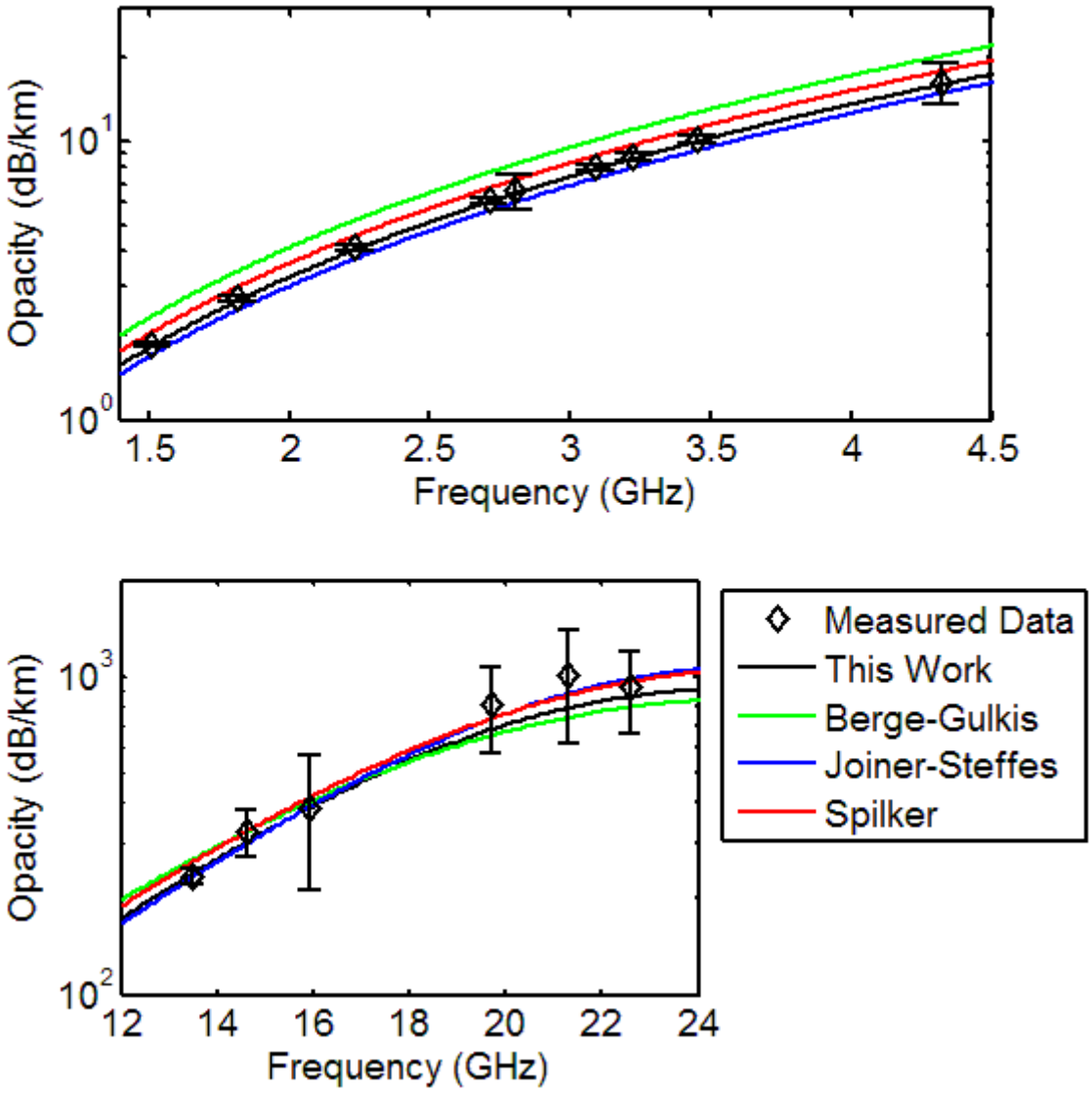

Figure 4.11: Opacity data measured using the large cavity resonator (above) and small cavity resonator (below) for a mixture of NH_3 = 4.0%, He = 13.06%, H_2 = 82.94% at a pressure of 4.004 bar and temperature of 294.9 K compared to various models.

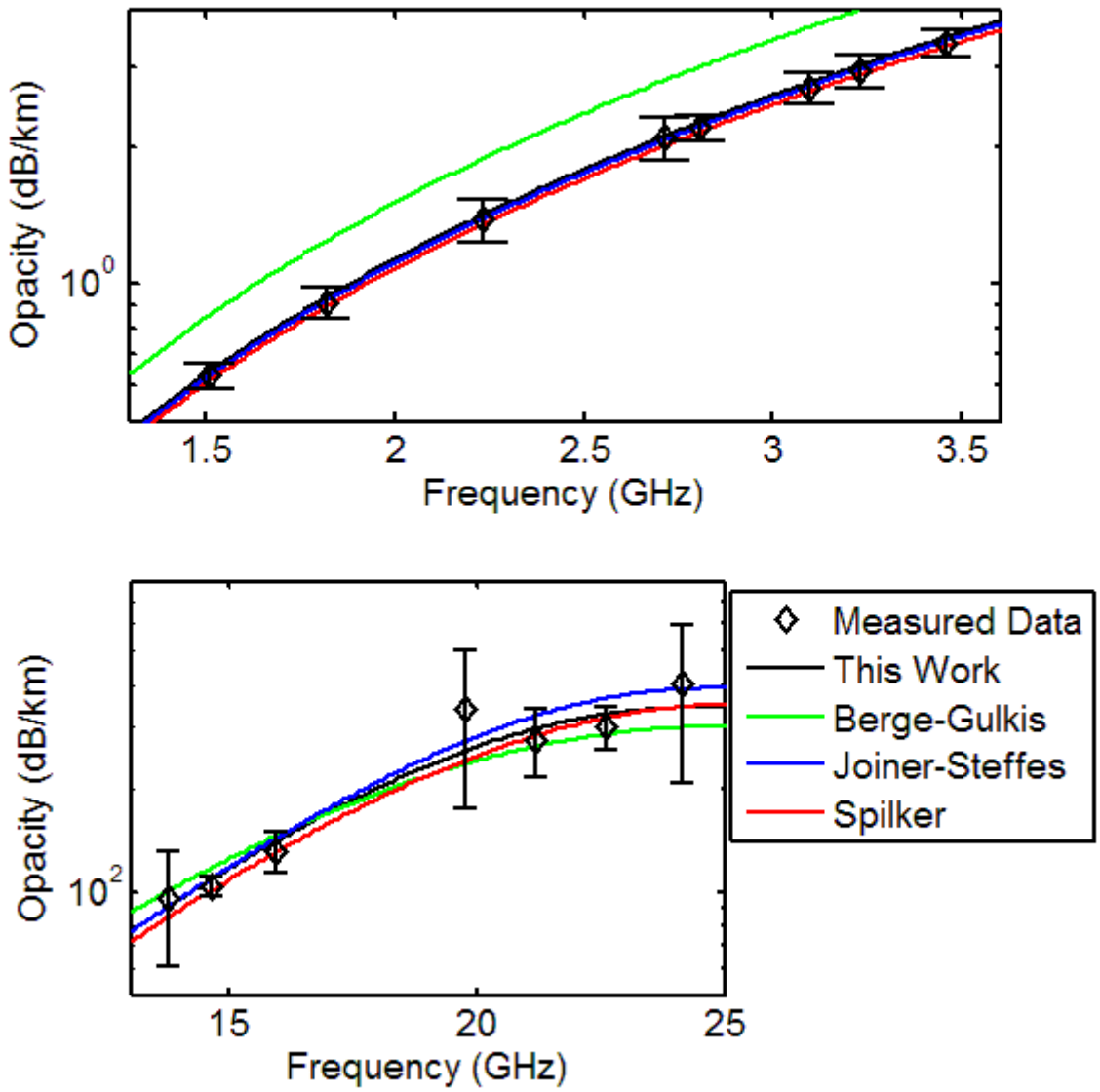

Figure 4.12: Opacity data measured using the large cavity resonator (above) and small cavity resonator (below) for a mixture of NH_3 = 0.79%, He = 13.49%, H_2 = 85.72% at a pressure of 3.987 bar and temperature of 217.8 K compared to various models. The models from this work and Joiner-Steffes overlap in the plot from the large cavity resonator.

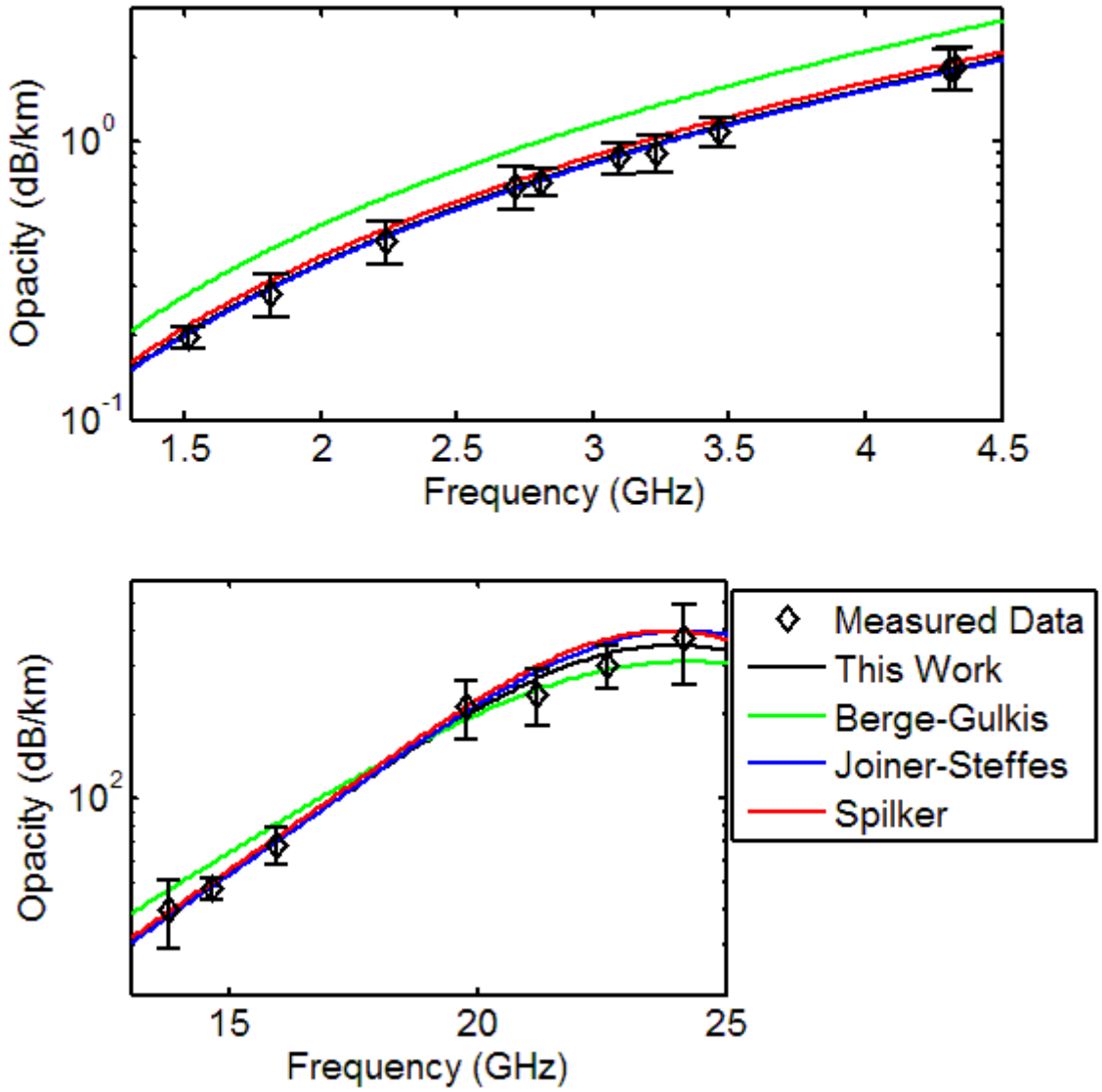

Figure 4.13: Opacity data measured using the large cavity resonator (above) and small cavity resonator (below) for a mixture of NH_3 = 0.88%, He = 13.48%, H_2 = 85.64% at a pressure of 2.092 bar and temperature of 217.6 K compared to various models. The models from this work and Joiner-Steffes overlap in the plot from the large cavity resonator.

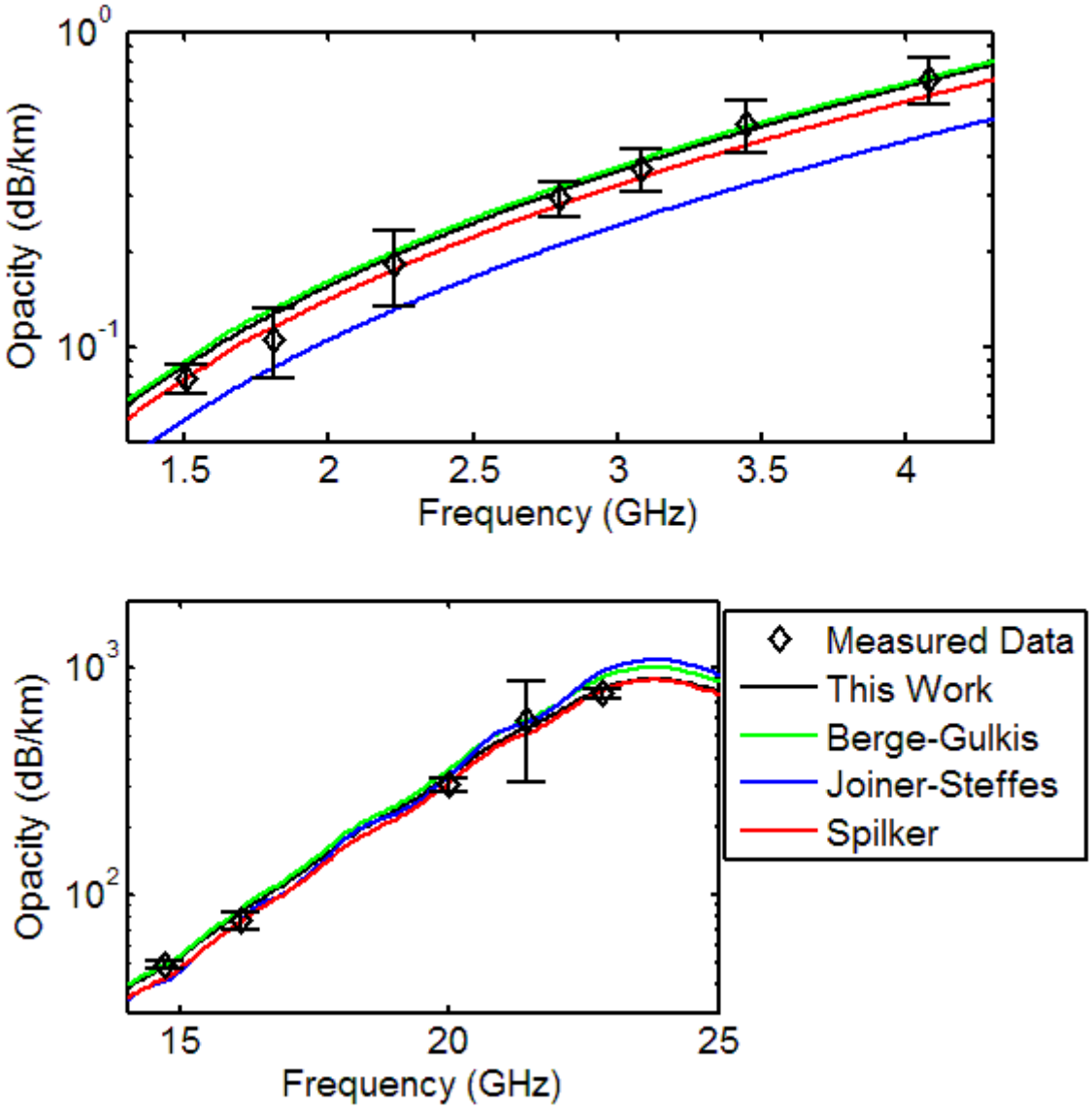

Figure 4.14: Opacity data measured using the large cavity resonator (above) and small cavity resonator (below) for pure NH_3 gas at a pressure of 118 mbar and temperature of 447.2 K compared to various models.

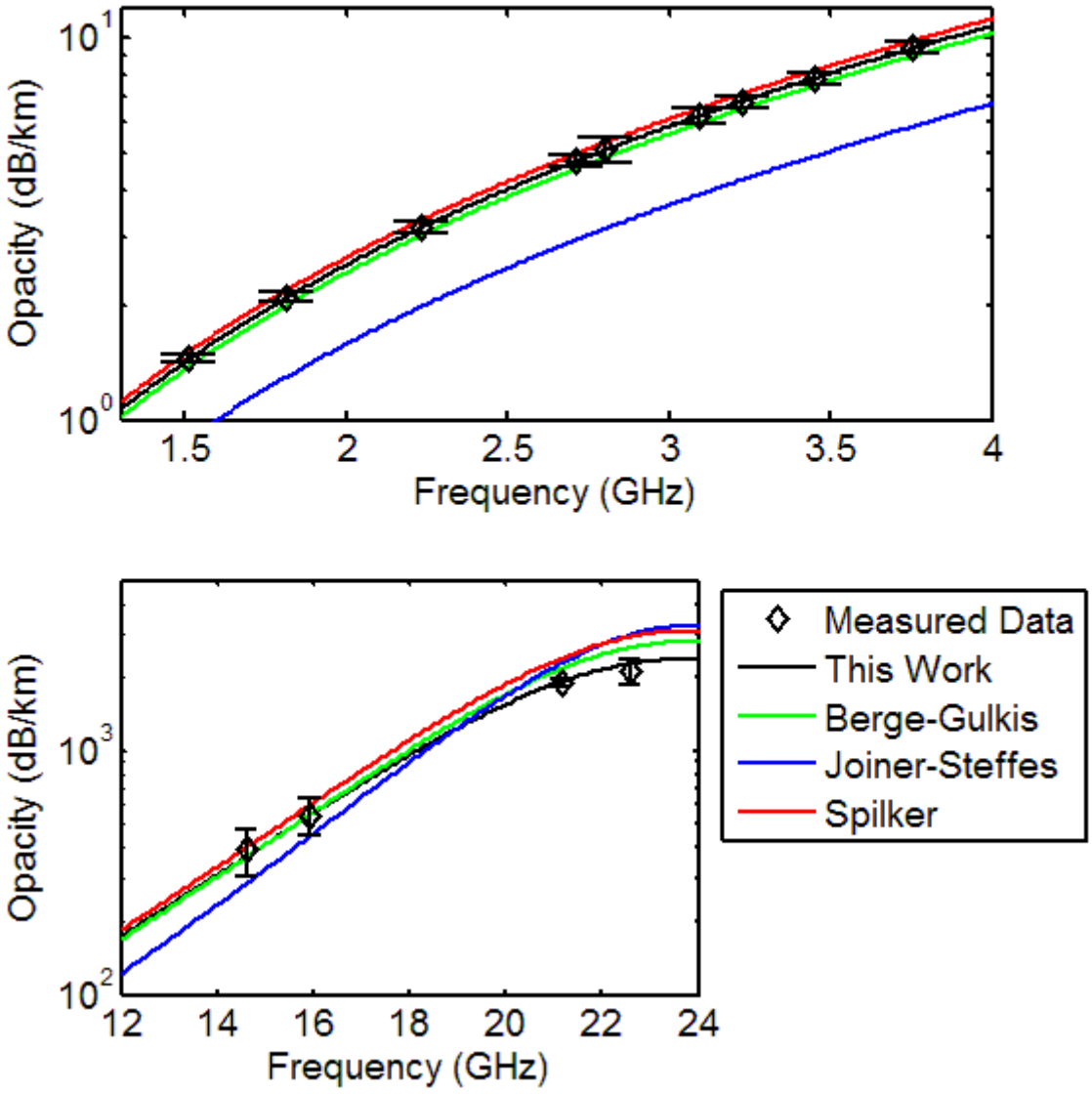

Figure 4.15: Opacity data measured using the large cavity resonator (above) and small cavity resonator (below) for pure NH_3 gas at a pressure of 249 mbar and temperature of 294.4 K compared to various models.

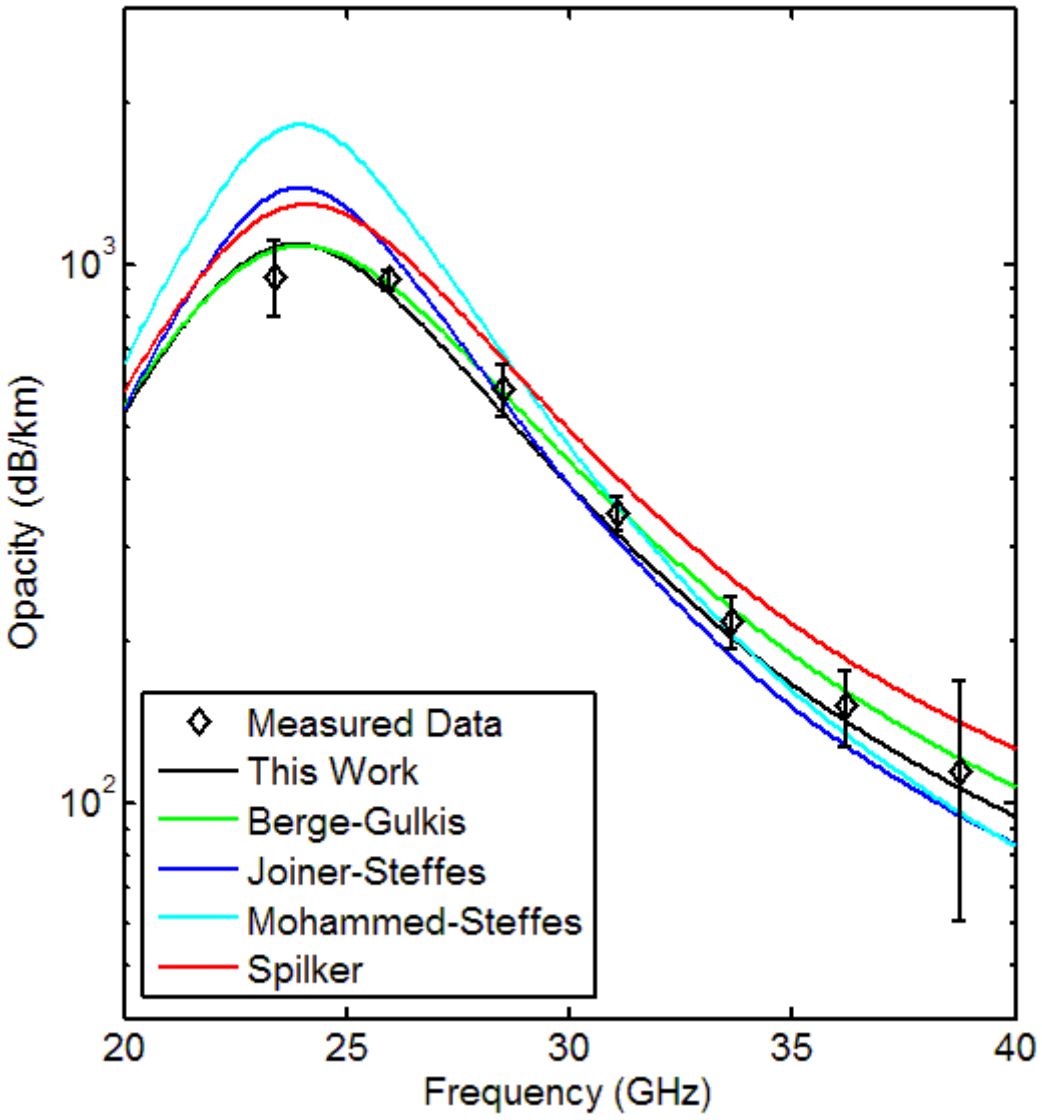

Figure 4.16: Opacity data measured using the Fabry-Perot resonator with a mirror spacing of 5.85 cm for a mixture of NH_3 = 8.0%, He = 12.51%, H_2 = 79.49% at a pressure of 1.0 bar and temperature of 295.5 K compared to various models.

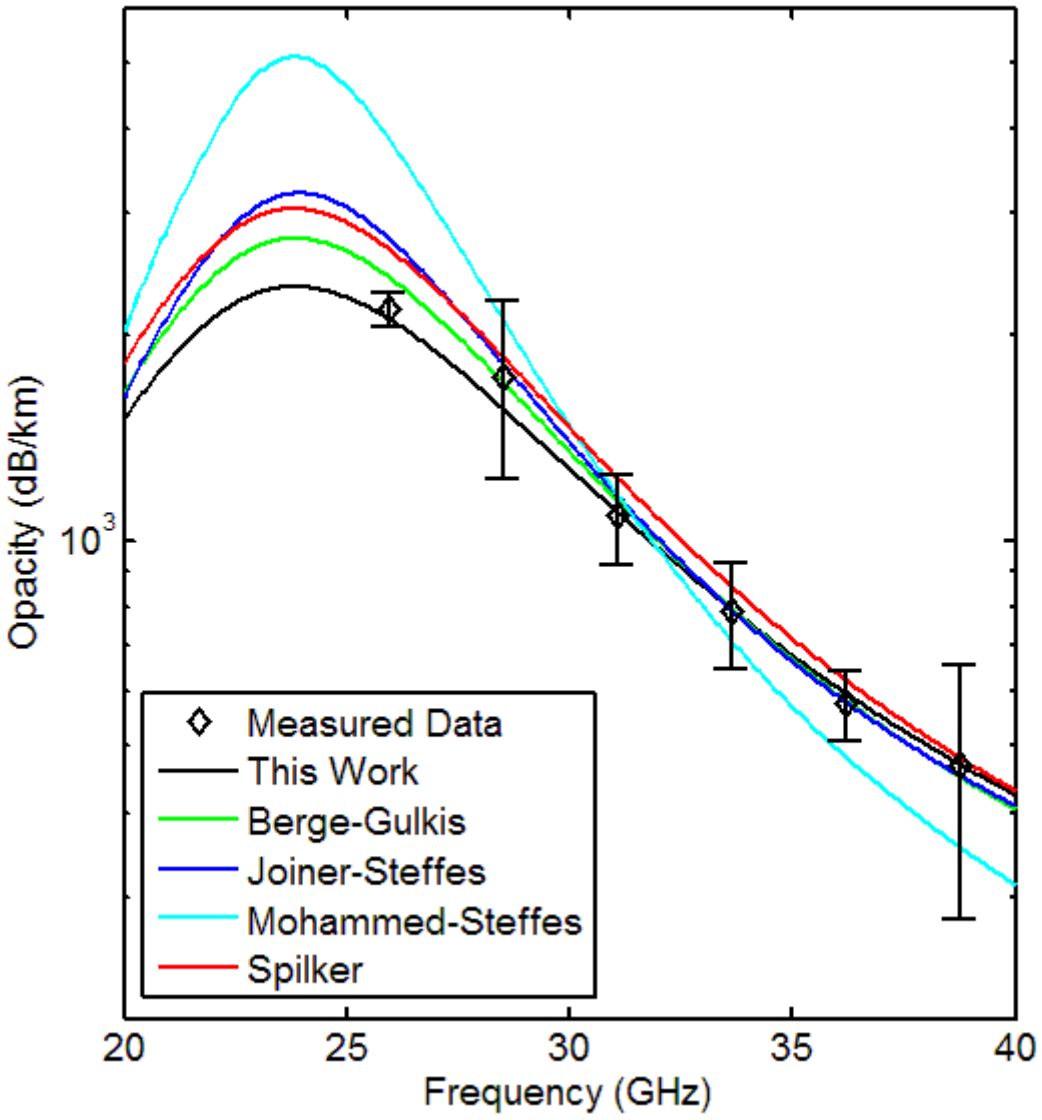

Figure 4.17: Opacity data measured using the Fabry-Perot resonator with a mirror spacing of 5.85 cm for pure NH_3 gas at a pressure of 240 mbar and temperature of 295.8 K compared to various models.

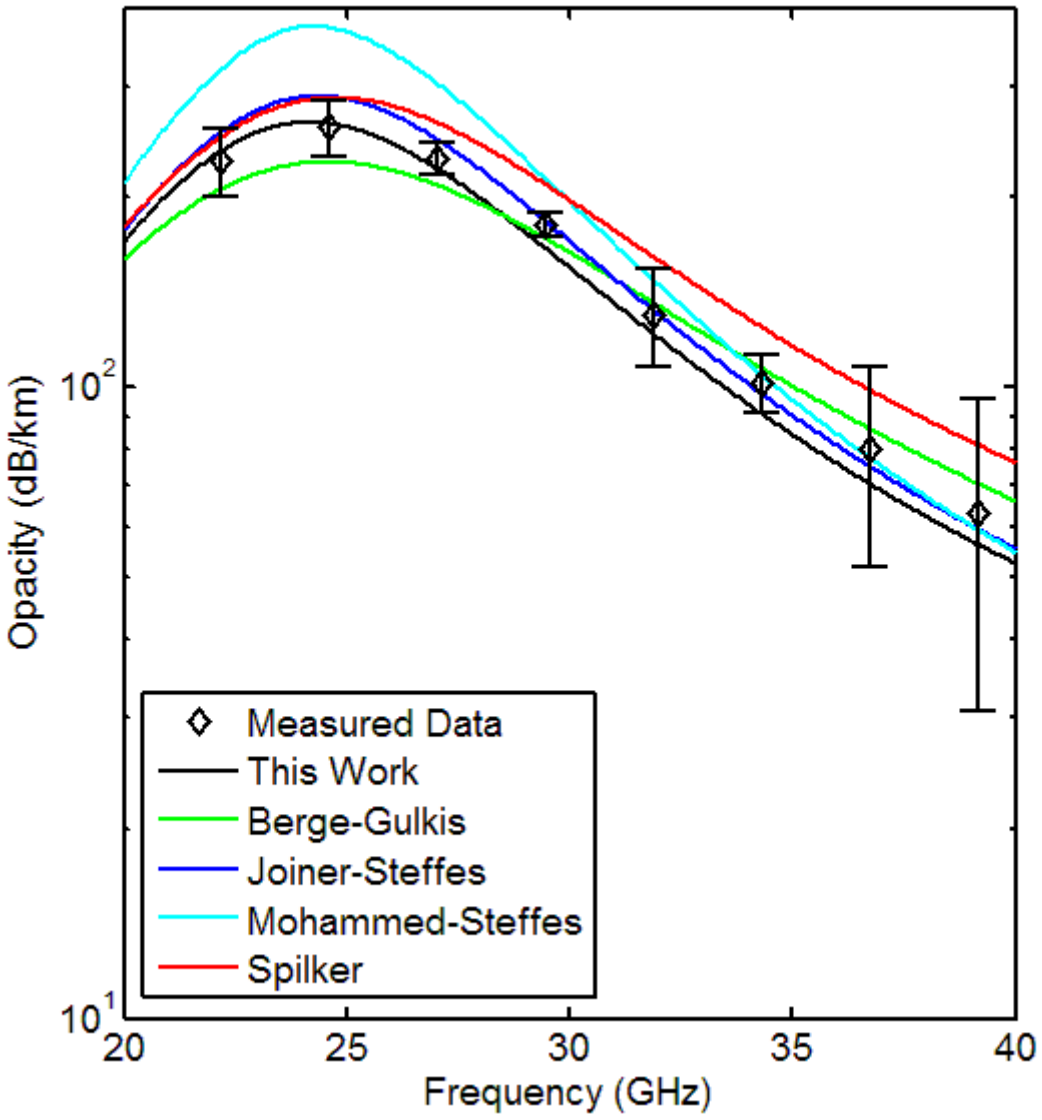

Figure 4.18: Opacity data measured using the Fabry-Perot resonator with a mirror spacing of 6.17 cm for a mixture of NH_3 = 0.98%, He = 13.47%, H_2 = 85.55% at a pressure of 3.002 bar and temperature of 295.7 K compared to various models.

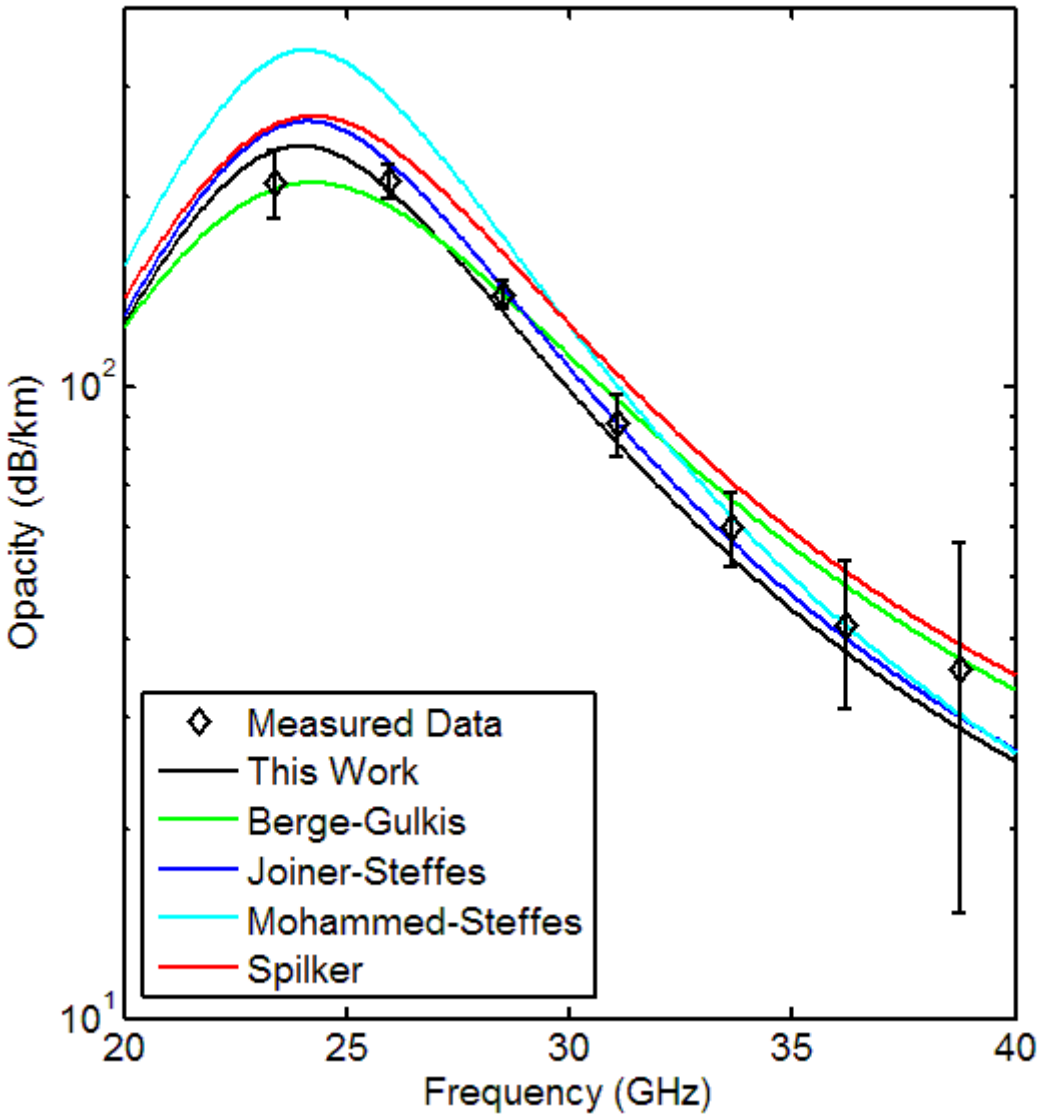

Figure 4.19: Opacity data measured using the Fabry-Perot resonator with a mirror spacing of 5.85 cm for a mixture of NH_3 = 0.98%, He = 13.47%, H_2 = 85.55% at a pressure of 2.0 bar and temperature of 295.3 K compared to various models.

CHAPTER 5: IMPACT OF NEW NH_3 MODEL

The new higher-accuracy model for the opacity of ammonia under Jovian conditions has a number of important benefits. Not only will it aid in more accurate retrievals of both NH_3 and H_2O abundances at Jupiter from future measurements (i.e. Juno), but it also allows previous measurements of the microwave properties of Jupiter to be reassessed, such as the Galileo Probe radio signal absorption measurements (Folkner *et al.* 1998). While the difference between the new model and others is generally less than 30% under the conditions measured by the Galileo Probe, the accuracies of the future retrievals of NH_3 and H_2O abundances from the highly sensitive Juno spacecraft will greatly benefit from the new model. Additional considerations and limitations must be considered however, when extrapolating the modeled results to the hundreds of bars of pressure that will be sensed by Juno's longest wavelength channel.

5.1 Galileo Entry Probe Results

The Galileo spacecraft was launched on its path toward Jupiter in October of 1989. It carried with it an atmospheric probe that was detached from the orbiter five months before the two arrived at Jupiter. On December 7, 1995, the probe entered Jupiter's atmosphere at a speed of 106,048 mph (Seiff *et al.* 1998). The craft was slowed due to drag and deployed a parachute to further slow its descent into the Jovian atmosphere. The probe communicated with the orbiter via a two channels, one right-circularly polarized at 1387.1 MHz and the other left-circularly polarized at 1387 MHz (Folkner *et al*. 1998). The transmitted and received power for both channels was monitored as the craft descended from an atmospheric pressure of roughly 0.5 bar down to a pressure of 22 bars about an hour later, whereupon the probe stopped transmitting. Through knowledge

of both the transmitting and receiving antenna gains, their pointing angles and the distance between the orbiter and the probe, the additional attenuation of the signal due to atmospheric absorption can be calculated. Folkner *et al*. (1998) attributed this atmospheric absorption solely to the presence of ammonia gas and used the model of Spilker (1990) to derive the concentration or mole fraction of NH_3 as a function of pressure. As previously discussed, the model of Spilker is less accurate than the model derived as part of this work. Therefore, the NH_3 mole fraction results derived by Folkner *et al*. (1998) can be adjusted using the state of the art NH_3 opacity model. The ratio of the new model to previous models can be seen in Figure 5.1. The anomalous behavior of the Spilker model relative to the others is due to its empirically derived scale term and broadening coefficients as a function of temperature. At temperatures above 600 K or below 40 K, the Spilker model predicts a negative opacity from NH_3, which is of course, non-physical.

To reprocess the results of Folkner *et al*. (1998) the numerical data from their plot of NH_3 mole fraction had to be extracted, since it was not available in tabular form. This was done by zooming in on the image in the digital copy of the article and counting the number of pixels between the data points and the scale markings. The mole fractions of NH_3 and the atmospheric pressures were combined with the corresponding temperatures from Seiff *et al*. (1998) and the He mole fraction from von Zahn *et al*. (1998) to generate the corresponding measured opacities, assuming the remainder of the composition was H_2. These opacities were then compared to the new NH_3 model by varying the mole fraction of NH_3 until the opacities were

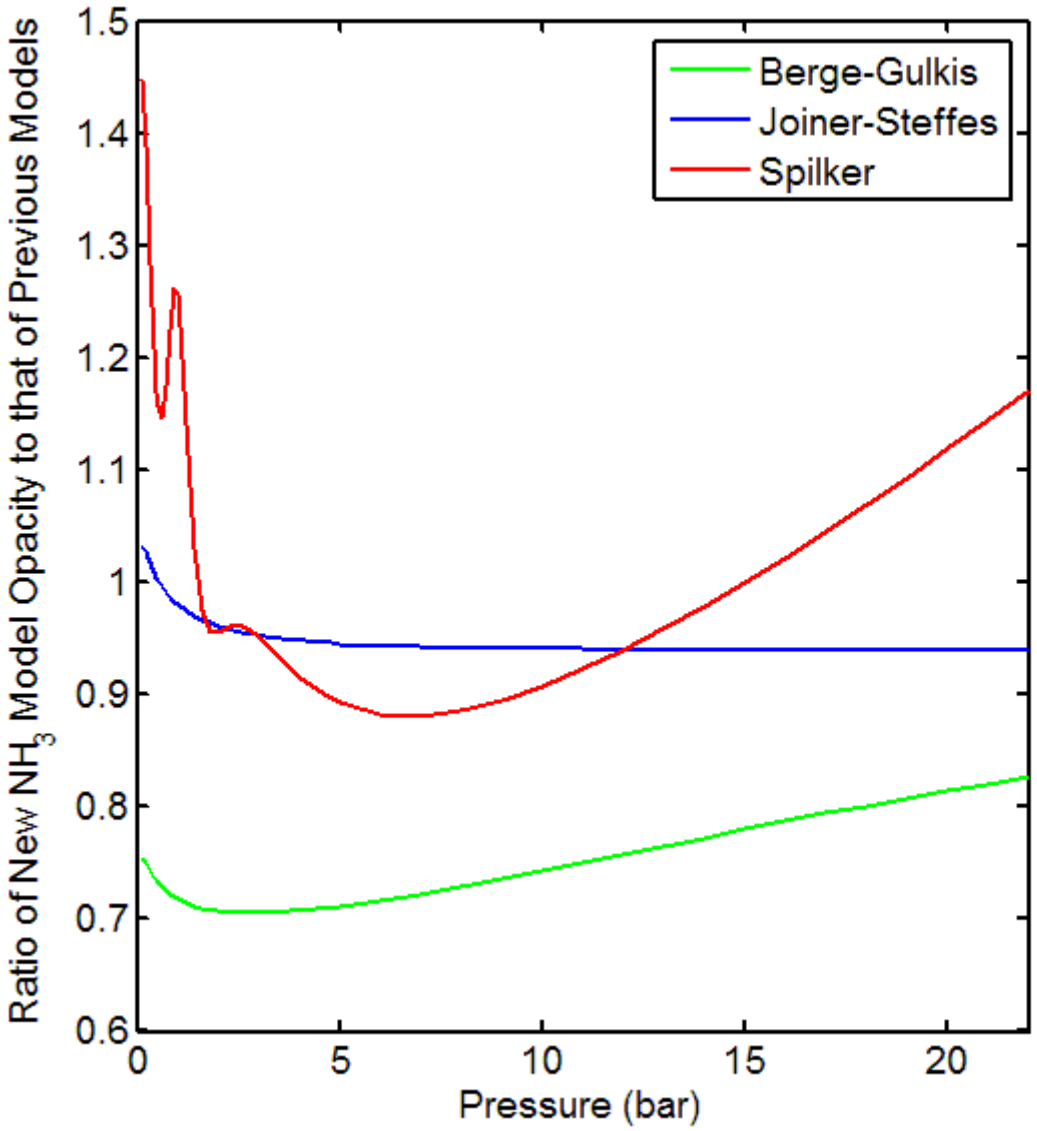

Figure 5.1: The ratio of the new ammonia opacity model at 1.387 GHz to the previous models under the pressure and temperature conditions of the Galileo Probe from Seiff *et al*. (1998) for a mixture of 0.05% NH_3, 13.5% He and 86.45% H_2.

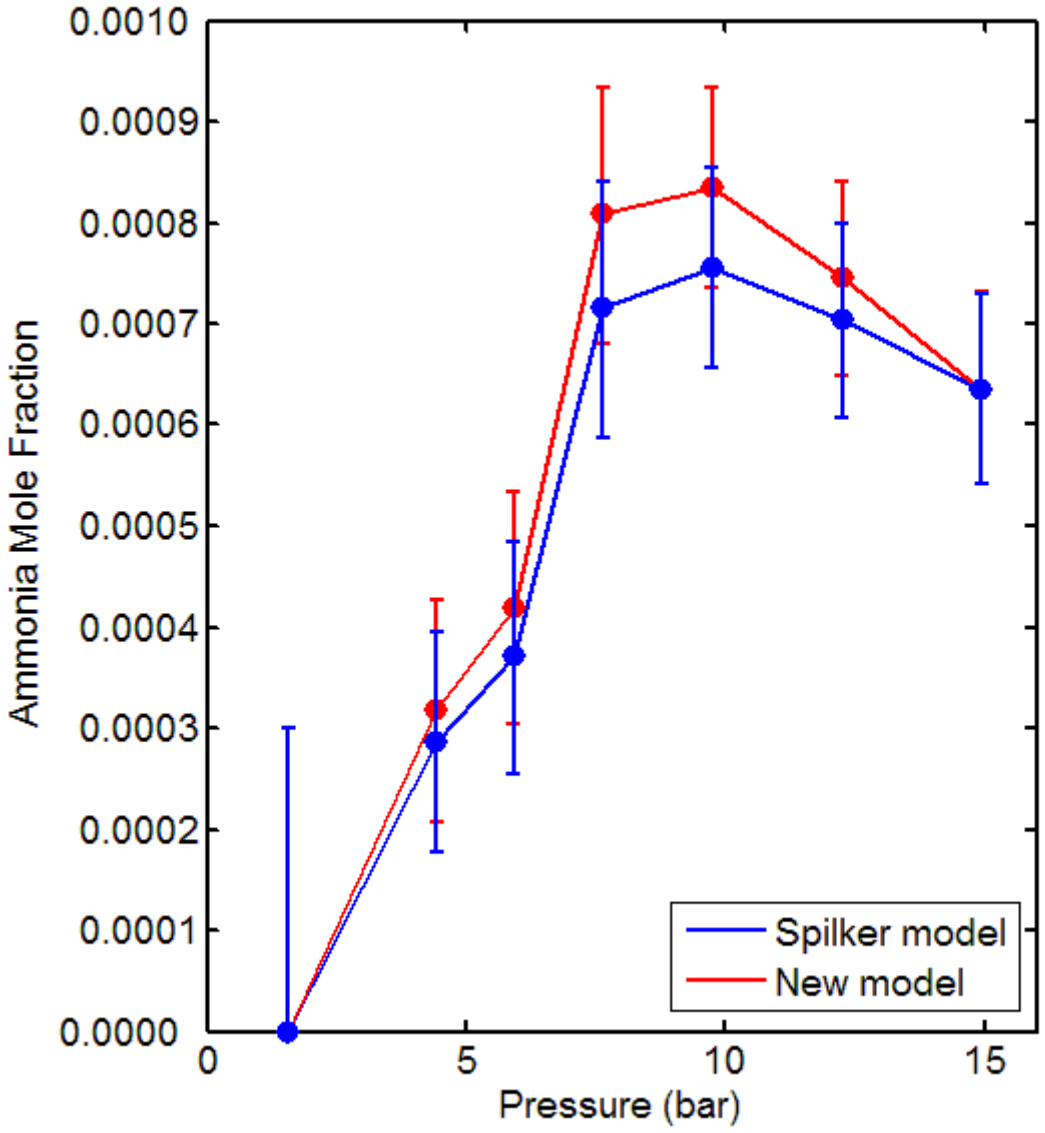

Figure 5.2: The results of the Galileo Probe radio signal absorption measurements of NH_3 mole fraction from Folkner *et al.* (1998), using the model of Spilker (1990), reanalyzed with the new model from this work.

identical. The size of the error bars remained unchanged since they were due to other uncertainties in the measurements. The new results are plotted in Figure 5.2.

The new Galileo Probe results are still consistent with the old results within the stated uncertainties, but have values from 5% to 15% higher than previously derived. The data are also in general agreement with the latest derived values from the Galileo Probe Mass Spectrometer (Atreya *et al*. 2003). The new data also show a more pronounced difference between the NH_3 mole fraction at 10 bars and 15 bars, similar to that measured by the Mass Spectrometer, meaning that the ammonia is not likely well-mixed at pressures below 7 bars. The downdraft that explains the increase of NH_3 mole fraction up to a pressure of 7 bars (Showman and Ingersoll 1998) may intersect with a stable atmospheric layer somewhere between 10 and 15 bars. Regardless, these new results show a peak NH_3 concentration roughly 6.5 times the latest published solar value of nitrogen relative to H_2 (Grevesse *et al*. 2005). By further measurement of the Jovian atmosphere by Juno and future spacecraft, the atmospheric dynamics and constituent concentrations and distributions can be better understood.

5.2 Juno Radiative Transfer Simulations

In order to utilize the brightness temperature data that will be taken by the Juno spacecraft, radiative transfer simulations must be performed. The simulations require making some assumptions about the behavior and structure of the atmosphere of Jupiter in order to match the brightness temperature data from each of the measurement channels. The radiative transfer model used to analyze the effect of the new model for NH_3 opacity is that of Hoffman (2001) as modified by Karpowicz *et al*. (2007). This

model relies on the thermochemical model of DeBoer (1995) to describe the behavior of the temperature of the atmosphere with pressure. The thermochemical model assumes a wet adiabatic dependence of temperature with pressure, such that the energy of a parcel of gas remains constant with changes in pressure. The model starts deep in the atmosphere using the concentrations of H_2, He, CH_4, NH_3, H_2O, PH_3, and H_2S as input parameters. The range of pressures from the 0.1 bar level down to 6000 bars is divided into incremental layers. As the pressure is decreased, the temperature also decreases and a check is performed to see if any of the gas components would condense at the new temperature. In this way, various cloud layers can also be simulated.

With the creation of a temperature-pressure profile and the models of molecular concentration with pressure, the transfer of microwave radiation from one layer to the next is simulated. Considering the black body thermal emission of each layer and the microwave absorption of its constituents, the amount of radiation at each measurement frequency exiting the atmosphere can be predicted. The input values of the concentration of each absorbing molecule can then be changed and a new iteration of the model calculated until the measured values for brightness temperature agree with the calculated values. The calculated brightness temperature as a function of frequency is shown for various conditions of possible deep NH_3 and H_2O concentrations in Figure 5.3, using the new model for NH_3 opacity and the model of DeBoer (de Pater *et al.* 2005) for H_2O opacity. The mean value of deep NH_3 concentration used is 0.039%, whereas the depleted and enhanced concentrations are 0.0172% and 0.0609% respectively. These values are roughly based on some maximum and minimum predictions from other authors (see, e.g. Kunde *et al*. 1982 and Atreya *et al*. 2003). The mean value of H_2O used

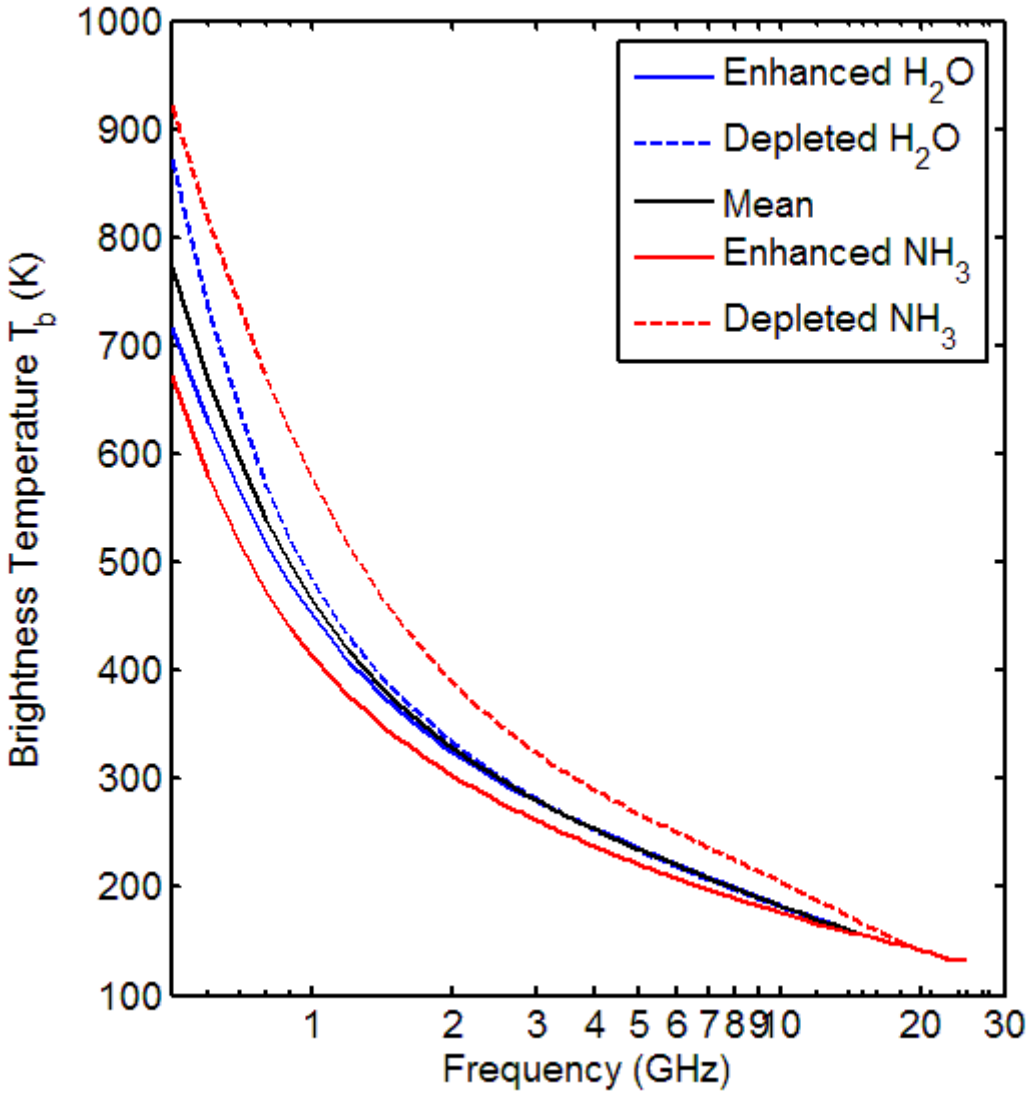

Figure 5.3: Predicted nadir brightness temperature under various conditions using the NH_3 opacity model of this work and the H_2O opacity model of DeBoer (de Pater *et al.* 2005).

in Figure 5.3 is 0.5474% or roughly 3.75 times the previously considered solar concentration of oxygen from Anders and Grevesse (1989) with the enhanced value being 0.8731% or six times solar and the depleted value of 0.2197% or 1.5 times solar. Both of the published values of the concentrations of solar nitrogen and oxygen decreased by close to 40% between 1989 and 2005, well outside the respective uncertainties of those published measurements. For this reason, it is important to reference the appropriate source of all solar concentration information at the time of publication, or to simply refer to the abundances of elements in *absolute* mole fraction. The effects of the various ammonia opacity models on the calculated brightness temperature at frequencies roughly corresponding to those proposed for Juno can be seen in Table 5.1.

Each measurement channel or frequency is represented by a weighting function, which defines the respective contribution of each pressure layer to the total emitted radiation. In essence, a weighting function describes which pressure layers are sensed at a particular frequency. Both the weighting function and brightness temperature calculations also depend on the emission angle of the radiation from the planet relative to the normal of its isobaric "surfaces". When this angle is 0° the alignment of the spacecraft antenna is said to be at nadir. At an angle of 60°, the maximum emission angle proposed for Juno (Janssen *et al.* 2005), the antenna is said to be pointing at the limb of the planet. Simple geometry demonstrates that the path length through the atmosphere at the limb is longer than that at nadir and thus limb brightness temperature values will be lower. This phenomenon is known as limb darkening. The weighting functions at the limb also probe less deep into the atmosphere than at nadir. The predicted opacities of the NH_3 models at the peak of each weighting function are shown

in Table 5.2. The calculated relative contributions of each pressure to the normalized weighting function at each frequency can be seen in Figures 5.4 and 5.5 for the nadir and limb cases respectively.

Table 5.1: The calculated nadir brightness temperatures (in K), for the mean concentrations of NH_3 and H_2O used in Figure 5.3, comparing the various NH_3 opacity models. *The Spilker model does not compute for these situations due to its anomalous behavior at higher temperatures.

Frequency (GHz)	This Work	Spilker (1990)	Joiner and Steffes (1991)	Berge and Gulkis (1976)
0.6	668.41	N/A*	656.90	642.93
1.2	418.72	N/A*	412.67	393.81
2.6	296.00	N/A*	293.39	279.42
5.2	231.66	N/A*	230.35	219.84
10.0	182.36	184.05	181.96	175.53
22.0	136.20	138.61	136.06	136.14

Table 5.2: NH_3 opacity values in dB/km from various models with an NH_3 concentration of 390 ppm. The pressures and temperatures utilized correspond to the peak of the respective weighting function at nadir for each frequency.

Frequency (GHz)	This Work	Spilker (1990)	Joiner and Steffes (1991)	Berge and Gulkis (1976)
0.6	0.022297	-0.0048543	0.023793	0.022158
1.2	0.070543	0.055327	0.075005	0.082867
2.6	0.13246	0.14838	0.14066	0.1795
5.2	0.22209	0.23804	0.23324	0.30905
10.0	0.45028	0.44147	0.46257	0.61416
22.0	15.569	10.401	16.11	15.139

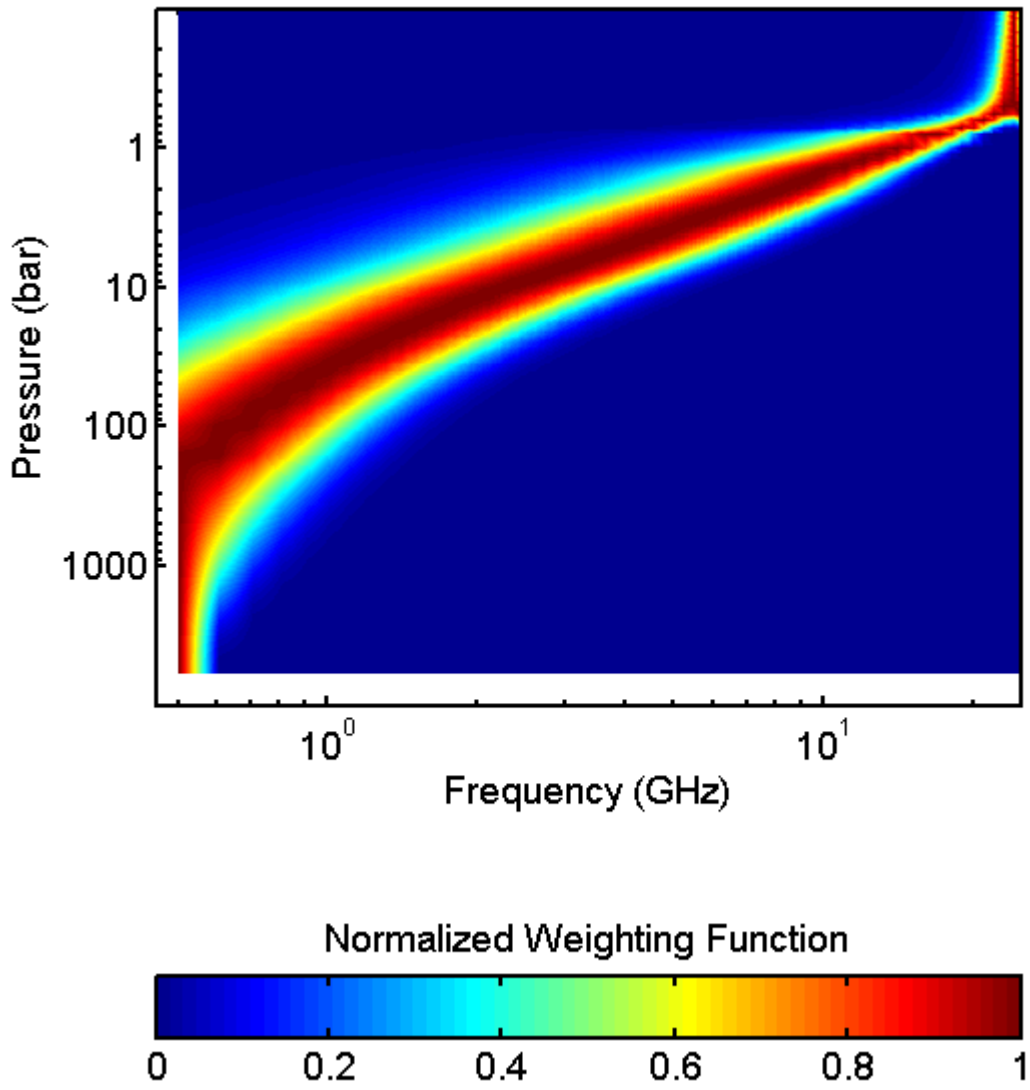

Figure 5.4: The normalized weighting function at each frequency as a function of pressure for a nadir viewing angle using the NH_3 opacity model of this work for the mean condition of Figure 5.3.

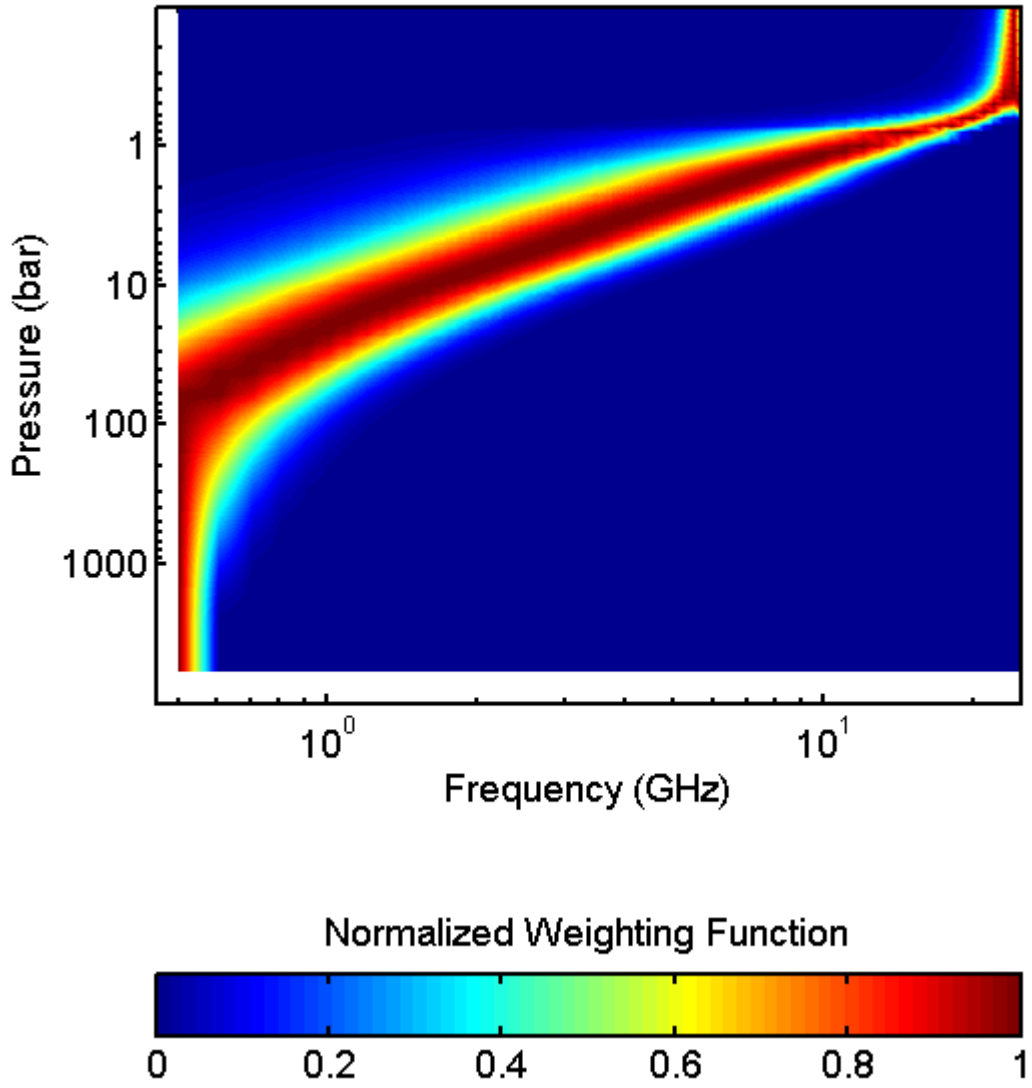

Figure 5.5: The normalized weighting function at each frequency as a function of pressure for a 60° emission angle using the NH_3 opacity model of this work for the mean condition of Figure 5.3.

5.3 High-Pressure Extrapolation and Influence of Rotational Lines

The absolute accuracy of the Juno Microwave Radiometer is estimated to be better than 2% with the relative measurements better than 0.1% (Janssen *et al*. 2005). The added precision of the newly derived model for H_2/He-broadened NH_3 opacity and a new model of H_2O opacity to be derived based on future high-pressure measurements, will allow the most accurate measurements of the concentration and distribution of ammonia and water vapor in the Jovian atmosphere to date. Some caution, however, must be exercised when using the new NH_3 model at pressures much greater than 50 bars. While the measurements from which the model was derived were only performed up to pressures of 12 bars, some extrapolation can be made to higher pressures with reasonable certainty. The measurements of Morris and Parsons (1970), hereby referred to as M&P, show that higher order effects become significant around pressures of 100 bars. Berge and Gulkis (1976) modeled these affects as a parabolic function of the number of hydrogen molecules, but did not include additional terms for the amount of helium present despite its behavior similar to that of hydrogen in the measurements of M&P. The data on the opacity of NH_3 measured by M&P show a steep increase in opacity with pressure up to around 100 bars, where the opacity tends to level off before increasing again, less steeply, at higher pressure. Morris (1971) attempts to explain this behavior as the shift from resonant to non-resonant Debye absorption similar to that of liquids along with the greater frequency of collision of the molecules. However, for this work, a different approach was taken. The impact of including the 20 lowest frequency NH_3 rotational lines from the JPL line catalog (Picket *et al.* 1998) from 572 GHz to 2951 GHz in the new NH_3 model was investigated and found to reproduce a similar rise in opacity with

pressure as that measured by M&P. This effect can be seen in Figure 5.6 comparing the model of Berge and Gulkis (1976) that was fit to the M&P data on the H_2-broadened opacity of NH_3 to the new model with and without the contribution of the first 20 rotational lines. The self-broadened linewidths used for each rotational line were chosen as 15 MHz/torr (although the results are not very sensitive to that value for this lower mole fraction of NH_3) and the calculation utilized the Gross (1955) lineshape, similar to the model of Joiner and Steffes (1991). The other scale factors, broadening parameters, and temperature dependences used for the inversion lines were also applied to the rotational lines. The results show that the rotational lines do provide significant added opacity for pressures above 100 bars and must be considered for any pressures greater than 100 bars.

There are other factors that change in the gas mixture as the pressures are increased, such as the deviation from ideal gas law that was not included in the model calculations of Figure 5.6. This would tend to decrease the overall opacity from the value calculated assuming an ideal gas mixture. Additionally, many of the assumptions about binary and elastic collisions used for most of the lineshape theories are invalid under these conditions. There is also some added uncertainty in the results of M&P due to their assumption that NH_3 did not adsorb in their glass system at room temperature during their procedure. This adds more uncertainty to the accuracy of their stated mixing ratios and although M&P acknowledge that the mixing ratio of ammonia changes with the partial pressure of the gas, their results are plotted showing a constant mixing ratio. Another possible shortcoming of the data is that it was taken at only one resonant frequency. The possibility of that resonance being contaminated by other resonances is non-trivial

despite the best efforts of damping unwanted modes, as was witnessed for many resonances in the cavity resonators used as a part of this work.

All of the possible uncertainties in the Morris and Parsons (1970) data and the fit of Berge and Gulkis (1976) to it further point out the challenges of modeling the deep Jovian atmosphere at the hundreds of bars of pressure that will be sensed by the Juno Microwave Radiometer's lowest frequency channel. They also show the difficulty in predicting the behavior of the rotational lines based on measurements at pressures and frequencies where their impact is not detectable, such as those measured as a part of this work.

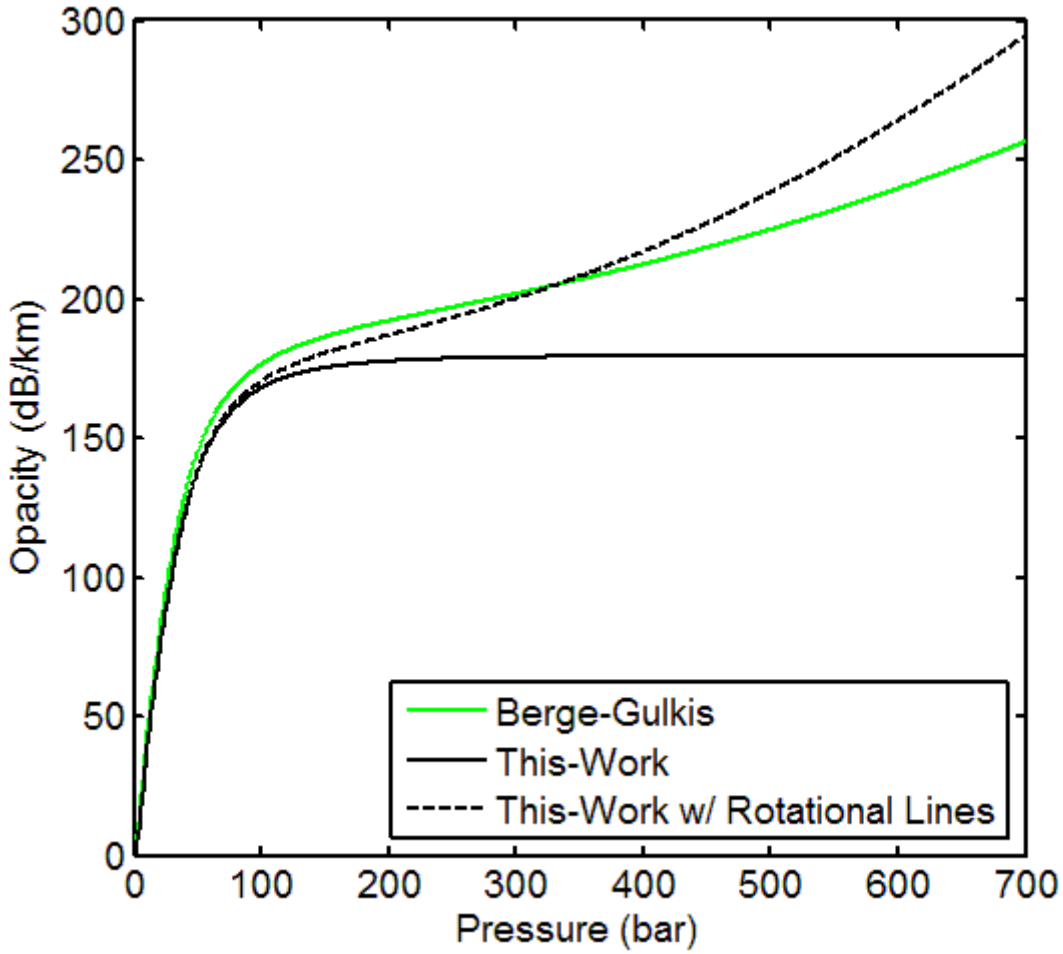

Figure 5.6: The effect of adding the contributions of the 20 lowest frequency rotational lines to the NH3 opacity model of this work. The simulation is performed under the same conditions as the experiment by Morris and Parsons (1970) that was fit by Berge and Gulkis (1976): T = 295 K, NH_3 = 1/229, He = 0, H_2 = 228/229, f = 9.58 GHz.

CHAPTER 6: SUMMARY AND CONCLUSIONS

The primary focus of this research has been to better understand the microwave behavior of gaseous ammonia and water vapor under the conditions of Jupiter. This was accomplished through the redesign and improvement of a high-sensitivity gaseous microwave measurement system that was used to characterize the properties of NH_3 and H_2O through a number of experiments. The results of the H_2O experiments were insufficient to devise a new model for H_2O opacity in an H_2/He atmosphere, but do indicate the shortcomings of the presently used models. The NH_3 results allowed for the derivation of the most accurate model to date of the microwave properties of gaseous NH_3, pressure-broadened by H_2 and He. The new model is valid specifically for temperatures between 185 and 450 K, but could easily be extrapolated beyond those bounds. It is accurate at total pressures of tens of mbar up to 12 bars and possibly upwards of 50 bars. The model works well for all concentrations of NH_3 that have been detected throughout the solar system and even pure NH_3 gas at pressures up to 300 mbar. The model accurately predicts the behavior of ammonia at frequencies up to 25 GHz under the aforementioned conditions and even up to 40 GHz for temperatures near 300 K and pressures below 3 bars. This new model has been used to reevaluate the results from the Galileo Probe radio signal absorption measurements and displays roughly a 10% increase over the previously calculated amount of ammonia present at pressures near 10 bars. Simulations under the measurement conditions of the Microwave Radiometer onboard the future Juno mission to Jupiter show that the new model for NH_3 opacity will help enable more accurate retrievals of both the concentration and distribution of ammonia and water vapor in the atmosphere of Jupiter. This, combined with better

knowledge of the solar concentration of H_2O and NH_3, will allow for a greater understanding of the formation of not only our solar system, but many other solar systems, some which may contain planets hospitable to life.

6.1 Suggestions for Future Work

While this work provides a high-accuracy model for the opacity of ammonia at Jovian conditions up to 50 bars, the lowest frequency of the Juno MWR will sense much deeper, down to pressures of hundreds of bars. As shown in Figure 5.6 the contributions from the rotational spectrum of NH_3 become significant at those pressures and the behavior of those lines must be verified. A new pressure vessel capable of withstanding pressures of 100 bars along with a digitally controlled oven that contains it have been procured through the support of the Juno mission. This vessel will allow much higher pressure measurements than measured previously at temperatures from 300 to 600 K (up to 100 bars). While this will be useful for detecting any new phenomena of the behavior of the NH_3 inversion lines at high pressures, it may not be sufficient to accurately predict the contributions of the rotational spectrum at frequencies below 25 GHz. To better detect this contribution, either the total pressure or the frequency of the measurements should be increased. Increasing the pressure would require a new pressure vessel capable of withstanding the higher pressures. The current 100 bar vessel is just large enough to contain the large cylindrical cavity resonator used in this work and weighs 1200 lbs. Building a vessel that could withstand higher pressures would become too cumbersome and expensive, unless its volume was reduced. Reducing the volume of the vessel would limit the size of the internal cavity resonator and increase the frequency of its lowest

frequency resonance. Since the higher frequencies probe less deep into the Jovian atmosphere, the extrapolation of the higher pressure measurements to the lowest frequency MWR channel of 600 MHz would cause additional uncertainty.

Measuring the properties of NH_3 at higher frequencies, however, requires smaller resonators. A cavity resonator similar to that of Newell and Baird (1965) could be manufactured to operate near 50 GHz. Although this frequency is closer to the rotational lines the predicted opacities are roughly 25 times higher under the same measurement conditions as Figure 5.6. This larger opacity would likely saturate the resonances and lessen the overall accuracy. A better approach is to move even higher in frequency to 150 GHz and operate at pressures on the order of a few bars, so the effect of the inversion lines on the total opacity is lesser. As shown in Figure 6.1, the effect of adding rotational lines is noticeable at 150 GHz. The properties of NH_3 between 75 and 150 GHz will be measured by fellow graduate student Kiruthika Devaraj using a fully confocal Fabry-Perot resonator enclosed in a glass tube capable of withstanding 3 bars of pressure. These high frequency signals will be generated using a times-six active multiplier chain or a frequency tripler, whereas various harmonic mixers will be used with the spectrum analyzer as a signal detector. These measurements may even help predict the behavior of the 140 GHz transition in the ν_2 vibrational band of NH_3 as predicted by Shimizu (1969) and measured by Chu and Freund (1973).

In order to more accurately measure the properties of water vapor under Jovian conditions, H_2O-H_2-He mixtures with higher opacities must be used. This will require the use of the new pressure vessel (previously mentioned) using the large cylindrical cavity resonator from 1.4 to 6 GHz to measure the gases at pressures up to 100 bars and

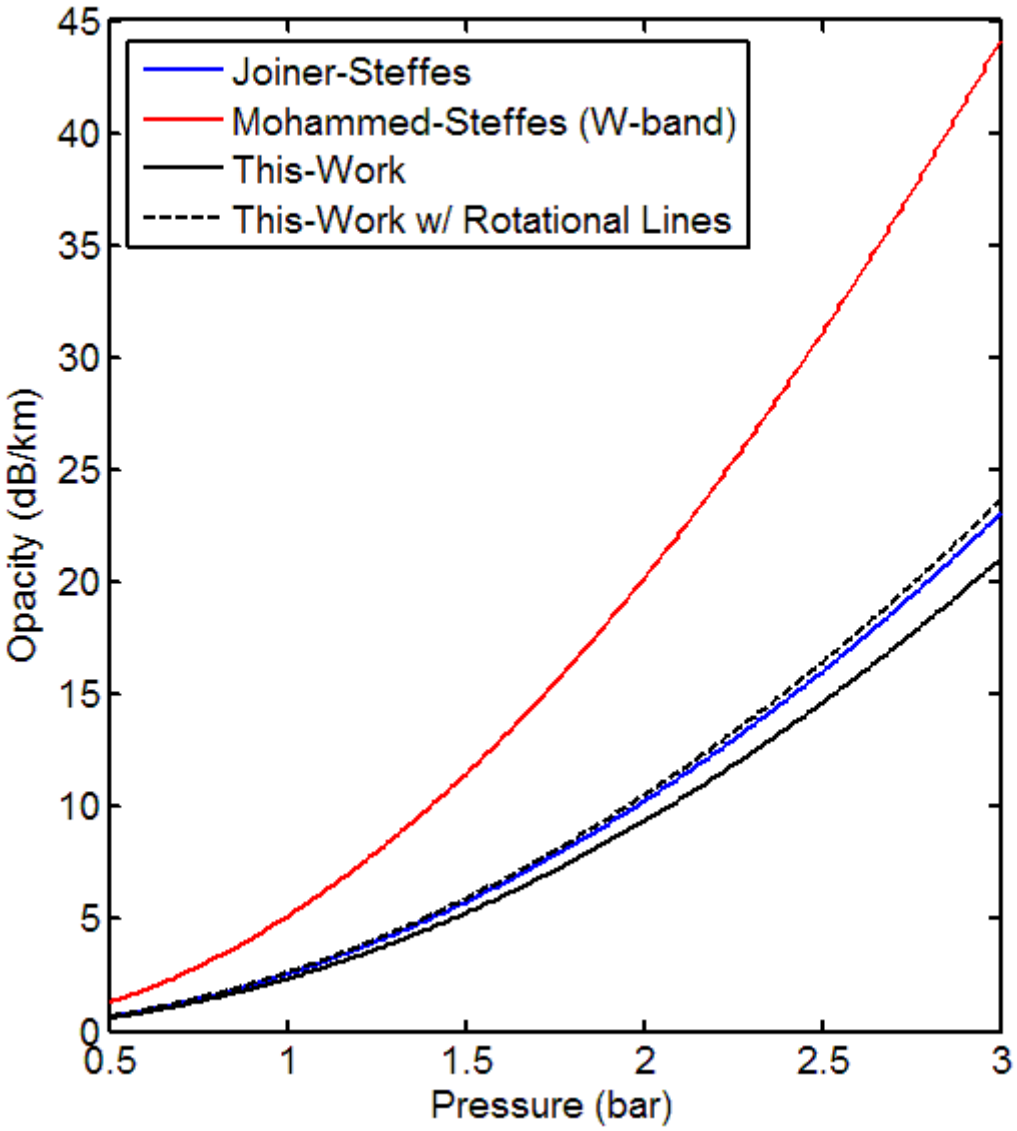

Figure 6.1: NH_3 opacity as a function of pressure as calculated by various models at 150 GHz for a mixture of 2% NH_3, 13.5% He, and 84.5% H_2 at 295 K. The models of Joiner and Steffes (1991) and Mohammed and Steffes (2004) are shown since they include some effect of the NH_3 rotational lines.

temperatures from 310 K to 525 K and possibly up to 600 K. This work will be performed by fellow graduate student Bryan Karpowicz using a further redesigned version of the system described in this work (see Karpowicz and Steffes 2008), and a new model for H_2O opacity under Jovian conditions will be derived. A plot of the temperatures and pressures of the NH_3 and H_2O measurements conducted as part of this work and future planned measurements is shown in Figure 6.2 along with the temperature-pressure profile of Jupiter.

Since the measured opacities of pure water vapor shown in section 4.1.2 are almost an order of magnitude higher than those predicted by the DeBoer model, it is possible that a thin layer of H_2O adsorbed to the inside walls of the resonators may be providing additional opacity. The effect of this layer on the absorptivity and refractivity of the measurements is not yet fully understood. To investigate this effect, additional measurements are necessary. One way to measure this would be to fill the pressure vessel containing the large cylindrical cavity resonator with ambient air on a humid day. A quick vacuum could then be drawn on the pressure vessel while simultaneously measuring the quality factor and center frequency of a number of resonances with the Agilent E5071C-ENA network analyzer. After the pressure in the vessel is less than 1 mbar, the vacuum pump would be closed off from the system and any adsorbed water would be allowed to desorb. The changes in center frequency and Q would be monitored as the water molecules transition from being bound to the surfaces in the vessel to the gaseous state. This procedure could be repeated with dry argon to calibrate any effects of temperature changes during the vacuuming due to the heat of expansion of the gases.

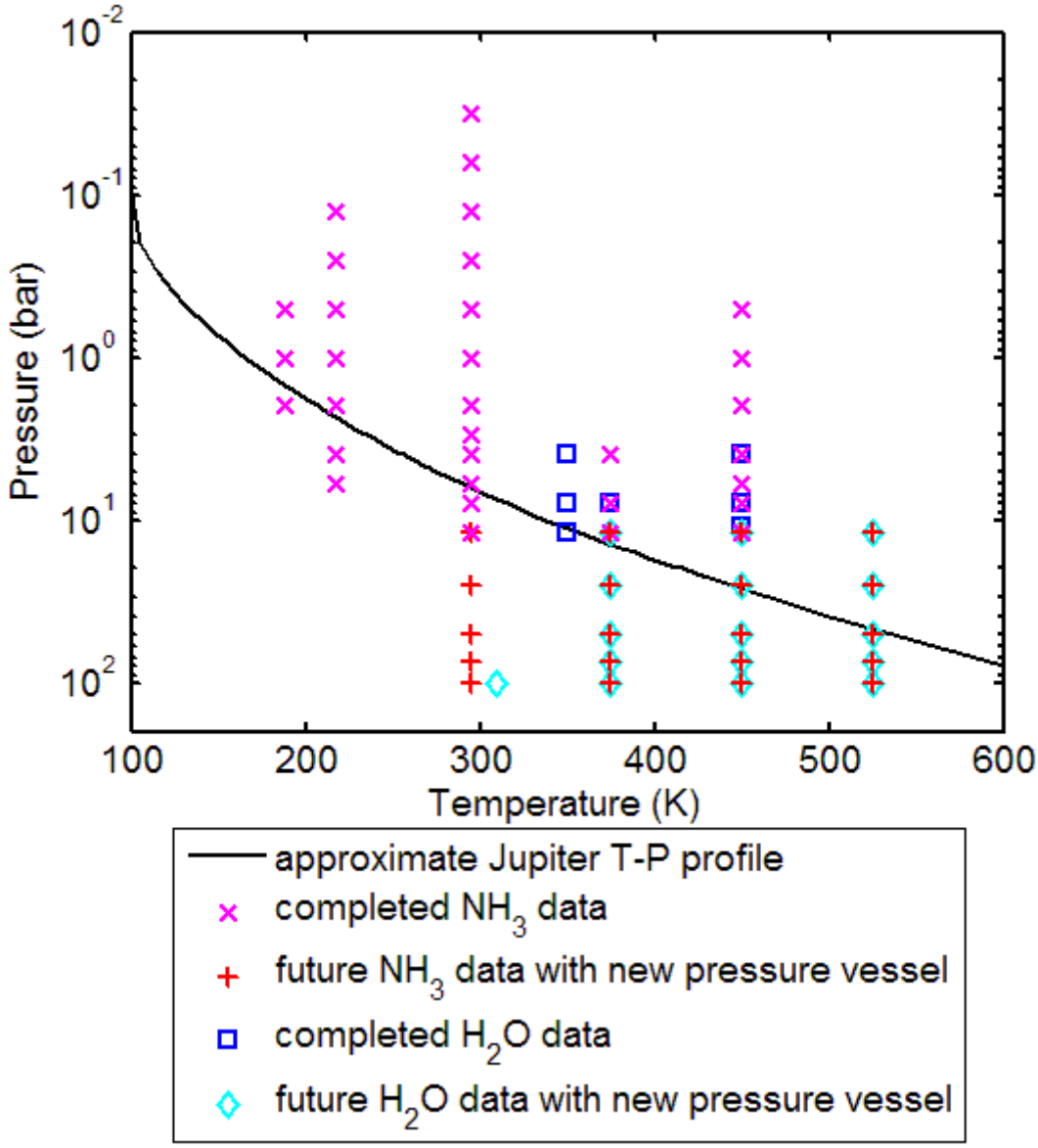

Figure 6.2: The pressure and temperature space showing the NH_3 and H_2O measurements of this and future works alongside the approximate conditions at Jupiter

The opposite effect could also be measured during the addition of the humid air to the evacuated vessel and tracking the subsequent adsorption of the water vapor.

The performance of the small cavity resonator could be improved for use in the new 100-bar pressure vessel, which would allow higher frequency measurements at higher pressure. To do this, the interior radius of the cylinder should be machined more uniformly, and the coaxial coupling probes should be replaced by waveguides with irises. Also, the mode suppression slots should be removed to provide uniform cylinder height around the resonator and thinner dielectric spacers should be used to lessen the amount of energy escaping the resonator. These improvements would allow greater precision at higher frequencies, which would be useful in measuring gases with lesser opacity.

Although the measurements performed as a part of this work involved gas mixtures with a constant helium to hydrogen ratio, future high pressure measurements should also incorporate mixtures of H_2O or NH_3 broadened only by H_2 and/or He. This would allow better determination of the individual effects of each broadening gas on the overall opacity, thereby increasing the accuracy of the models under conditions of other outer planets (Saturn, Uranus and Neptune) that have different He to H_2 ratios than Jupiter.

6.2 Contributions

Throughout the course of this work, several contributions have been made by this author to the fields of microwave spectroscopy and planetary atmospheric modeling.

First, the microwave measurement system previously used by Hoffman *et al.* (2001) was upgraded to enable greater precision. This involved the recognition of

overlapping TM modes and the placement of dielectric spacers in the cavity resonators to improve their performance. More accurate temperature and pressure monitoring devices were installed and for the first time a network analyzer was used to measure the resonances of the large cavity resonator during experiments. The adsorptive behavior of ammonia, which was recognized as a major source of uncertainty in previous measurements by other authors, was characterized for this measurement system for the first time by the addition of a Fabry-Perot resonator operating at K/K_a-band. The performance of this resonator was greatly improved by moving the mirrors much closer together than done previously. Procedures were developed, such as the "replace-half" technique, to ensure more accurate knowledge of the NH_3 mole fraction in all measured gas mixtures. The differential adsorption of NH_3 in various volumes of the pressure vessel was detected and a method of tracking the center frequency and Q of multiple resonances was developed to ensure uniform gas mixing and thermal stabilization throughout the pressure vessel before any measurements were performed. Software was developed to replace that of DeBoer and Steffes (1996) allowing further automation of measurements and more accurate data processing and storage with the added convenience of the Matlab® platform. A new program was written to further automate the process of dielectric matching that drastically reduces the amount of uncertainty it provides.

This improved microwave measurement system was used to measure the microwave properties of ammonia and mixtures of ammonia, hydrogen and helium under a wider range of conditions than measured by previous authors. This led to the retrieval of over 2000 individual usable data points of the behavior of NH_3. A formula was devised to weight the data equally throughout the range of measurement temperatures,

pressures, NH_3 concentrations and frequencies. A model was derived that fit the data more accurately than any previous models and was used to reprocess the NH_3 mole fraction data from the Galileo Probe radio signal absorption experiment. The applicability of this model to simulated results from the future Juno mission was confirmed.

The microwave properties of water vapor and mixtures of water vapor, hydrogen and helium were also investigated. The opacity and refractivity of $H_2O/H_2/He$ was measured under higher-pressures than ever before and the shortcomings of the models of DeBoer (de Pater *et al*. 2005) and Goodman (1969) were identified. The need for more higher-pressure measurements of the opacity of H_2O was recognized and a plan for future measurements constructed.

6.3 List of Publications

Refereed Journal Articles:

T.R. Hanley and P.G. Steffes (2008), "A New Model of the Hydrogen and Helium-Broadened Microwave Opacity of Ammonia Based on Extensive Laboratory Measurements," *Icarus*, in preparation.

T.R. Hanley and P.G. Steffes (2007), "A High-Sensitivity Laboratory System for Measuring the Microwave Properties of Gases under Simulated Conditions for Planetary Atmospheres," *Radio Science*, 42, RS6010, doi:10.1029/2007RS003693.

T.R. Hanley and P.G. Steffes (2005), "Laboratory Measurements of the Microwave Opacity of Hydrochloric Acid Vapor in a Carbon Dioxide Atmosphere," *Icarus*, 177, 286-290, doi:10.1016/j.icarus.2005.03.018.

Conference Presentations:

B.M. Karpowicz, P.G. Steffes, and T.R. Hanley, "A Laboratory System for Simulation of Extreme Atmospheric Conditions in the Deep Atmospheres of Venus, Jupiter, and Beyond," *Proceedings of the 6th International Planetary Probe Workshop*

(IPPW-6). To be presented at the 6th International Planetary Probes Workshop, Atlanta, GA, June 25, 2008.

T.R. Hanley and P.G. Steffes, "New Laboratory Measurements of the Microwave Absorption Coefficient of Ammonia and Water Vapor under Jovian Conditions", Proceedings of the 2008 URSI National Radio Science Meeting, p. 12, Presented at the 2008 URSI National Radio Science Meeting, Boulder, CO, January 3, 2008.

P.G. Steffes, T.R. Hanley, B.M. Karpowicz, and K. Devaraj, "Laboratory Measurements of the Microwave and Millimeter-Wave Properties of Planetary Atmospheric Constituents: The Georgia Tech System," In *Workshop on Planetary Atmospheres*, pp. 117-118. LPI Contribution No. 1376, Lunar and Planetary Institute, Houston. Presented at the 2007 Workshop on Planetary Atmospheres, Greenbelt, MD, November 6, 2007.

T.R. Hanley and P.G. Steffes, "New High-Precision Laboratory Measurements of the Hydrogen and Helium Broadened Microwave Opacity of Ammonia under Simulated Deeper Atmospheric Jovian Conditions," Bulletin of the American Astronomical Society, vol. 39, no. 3, 2007, p. 447. Presented at the 39th Annual Meeting of the Division for Planetary Sciences of the American Astronomical Society, Orlando, FL, October 9, 2007.

P.G. Steffes, B.M. Karpowicz and T.R. Hanley, "A Laboratory System for Measurement of the Centimeter-Wave Properties of Gases under Simulated Conditions for Deep Jovian Atmospheres," Bulletin of the American Astronomical Society, vol. 39, no. 3, 2007, p. 447. Presented at the 39th Annual Meeting of the Division for Planetary Sciences of the American Astronomical Society, Orlando, FL, October 9, 2007.

P.G. Steffes and T.R. Hanley, "An Enhanced System for Laboratory Measurements of the Centimeter-Wave Properties of Ammonia under Simulated Conditions for the Outer Planets," Bulletin of the American Astronomical Society, vol. 38, no. 3, 2006, pp. 608-609. Presented at the 38th Annual Meeting of the Division for Planetary Sciences of the American Astronomical Society, Pasadena, CA, October 12, 2006.

T.R. Hanley and P.G. Steffes, "New High-Precision Laboratory Measurements of the Hydrogen and Helium Broadened Microwave Absorption of Ammonia under Simulated Jovian Conditions," *Bulletin of the American Astronomical Society*, vol. 38, no. 3, 2006, p. 608. Presented at the 38th Annual Meeting of the Division for Planetary Sciences of the American Astronomical Society, Pasadena, CA, October 12, 2006.

T.R. Hanley and P.G. Steffes, "Method of Characterizing Ammonia Opacity in Jovian Atmospheres with Application to Entry Probe Radio Links," *Proceedings of the*

4th International Planetary Probe Workshop (IPPW-4), 7 pages. Presented at the 4th International Planetary Probes Workshop, Pasadena, CA, June 29, 2006.

A. Rager, T.R. Hanley, C. Calvin, T. Balint, D. Santiago, J. Anderson, T. Cassidy, D. Chavez-Clemente, B.M. Corbett, H. Hammerstein, A. Letcher, E.M. McGowan, D.S. McMenamin, N. Murphy, M.D. Obland, J.S. Parker, T. Perron, N. Petro, M. Pulupa, R. Schofield, and H.G. Sizemore, "Endurance: The Rewards and Challenges of Landing a Spacecraft on Europa," *Proceedings of the 4th International Planetary Probe Workshop (IPPW-4)*, 8 pages. Presented at the 4th International Planetary Probes Workshop, Pasadena, CA, June 28, 2006.

T.R. Hanley and P.G. Steffes, "New Laboratory Measurements of the Microwave Absorption of Ammonia under Jovian Conditions," *Bulletin of the American Astronomical Society*, vol. 37, no. 3, 2005, p. 774. Presented at the 37th Annual Meeting of the Division for Planetary Sciences of the American Astronomical Society, Cambridge, UK, September 9, 2005.

T.R. Hanley and P.G. Steffes, "The Microwave Absorption Properties of Hydrochloric Acid Vapor in the Venus Atmosphere," *Bulletin of the American Astronomical Society*, vol 36, no. 4, 2004, p. 1165. Presented at the 36th Annual Meeting of the Division for Planetary Sciences of the American Astronomical Society, Louisville, KY, November 11, 2004.

P.G. Steffes and T.R. Hanley, "Preliminary Results for the Centimeter Wavelength Opacity of Water Vapor Under Jovian Conditions Based on New Laboratory Measurements," *Bulletin of the American Astronomical Society*, vol 36, no. 4, 2004, p. 1154. Presented at the 36th Annual Meeting of the Division for Planetary Sciences of the American Astronomical Society, Louisville, KY, November 11, 2004.

APPENDIX A: DISCUSSION OF MOLECULAR ADSORPTION AND THE SYNTHESIS OF AMMONIA

Adsorption is the process of gaseous molecules of one substance, the adsorbate, adhering to the surface of a liquid or solid substance, the adsorbent or substrate. This is not to be confused with absorption, where the molecules are allowed to diffuse into the liquid or solid and form a solution. There are two types of adsorption, chemical and physical, sometimes referred to as chemisorption and physisorption. Chemisorption requires the formation of a chemical bond between the substrate and the adsorbate along with any suitable activation energy to fuel the chemical reaction. Physisorption, however, relies on the weaker attractive van der Waals forces between the adsorbate and the substrate and does not result in any sharing of electrons. Physisorption can occur in any gas-solid system, as long as the proper temperatures and pressures occur, similar to condensation (Young and Crowell 1962). It is most likely to occur when the gas is near its condensation point, but can occur under warmer, lower pressure conditions. Chemisorption can occur at virtually any temperature and pressure, as long as the activation energy of the reaction is present. Because chemical bonds are present, chemisorbed molecules are limited to one molecular layer thick. Physisorbed molecules, however, can form multiple layers on a substrate, which can amplify the effect of physisorption. While all molecules can encounter physisorption, polar molecules are more prone to it, especially when the substrates are conductors. One analogy is a molecule electromagnetically interacting with its image in the plane of the conductor.

When adsorbed molecules are returned to the gas phase, this is known as desorption. The most effective ways to cause desorption of physisorbed molecules are to

decrease the partial pressure of the gas or to warm the substrate to provide the molecules enough energy to overcome the attractive forces holding them in place. This is true for ammonia physisorbed to activated carbon, where adsorption was measured to decrease with increasing temperature or decreasing concentration (Rodrigues and Moraes 2002). In the case of chemisorbed molecules, desorption can be a difficult and elaborate process to retrieve the adsorbed molecules in their original form, if even possible.

Adsorbed molecules have limited degrees of freedom and therefore do not absorb incident electromagnetic energy to the extent they would in the gaseous phase. Adsorbed molecules, however, do change the electrical conductivity of the surfaces, to which they adsorb (Young and Crowell 1962). The extent to which this affects good conductors depends on the thickness of the conductor, its porosity, and its surface area. For the sake of the cylindrical cavity and Fabry-Perot measurement systems described in this document, the effect of adsorbed ammonia or water vapor has been measured to have a negligible effect on the conductivity and resulting Q's of the resonators.

Adsorption is very difficult to quantify or exactly predict due to its dependence on the fine molecular structure of the substrate. This means that extra precautions must be made to account or compensate for adsorption in laboratory measurements anytime a mixture of gases is used where some components will adsorb more than others. One solution would be to cover every material the gas mixture could contact with an anti-adsorption coating. This could lessen the overall effect of adsorption, although it would not completely eliminate physisorption. The other approach, the one used in this work, involves the use of spectroscopic techniques to determine the extent of adsorption occurring in any experiment and repeated gas cycling to saturate its effects.

Chemisorption is critical to the Haber-Bosch process used in the synthesis of ammonia since the early 1900's. Both molecular hydrogen and nitrogen chemisorb and dissociate onto the surface of a catalyst, mainly iron (Fe), at temperatures around 400°C. The hydrogen atoms are highly mobile on the surface of the catalyst at that temperature, while the nitrogen atoms are usually trapped in the crystal lattice structure of the iron (Ertl 1983). As the hydrogen atoms transit the surface they react with nitrogen atoms forming NH, NH_2 and eventually NH_3. Upon their formation, the NH_3 molecules desorb due to the exothermic reaction. As with all chemical reactions, equilibrium exists between the reactants and the products. In the case of ammonia synthesis, only about 15% of the reactants form NH_3 at 400°C, so to increase production, the reaction is typically performed at pressures of 100 atmospheres or greater. The Haber-Bosch process is responsible for the majority of the world's production of ammonia and is perhaps the most famous application of adsorption and surface chemistry.

APPENDIX B: MATLAB® SOFTWARE IMPLEMENTATIONS

The software written as a part of this work can be divided into two main areas: data retrieval and data processing. The software in each area is further separated by the instrument which was used to measure the data. Since the spectrum analyzer and network analyzer utilize different control commands, separate scripts exist for controlling each device to take measurements. Even the higher-frequency network analyzer (40 GHz) that was temporarily used for some experiments requires different commands. Measurements below 8.5 GHz are exclusively taken by the Agilent E5071C-ENA network analyzer and for measurements above 8.5 GHz, the HP 8564E spectrum analyzer and the HP 83650B swept signal generator are utilized. Several codes have been written for each device that perform various tasks of controlling the instruments and retrieving the data. All of the data taken by the codes is plotted on the computer screen in real-time for the user to identify that the full amount of data was retrieved and that no excess noise was measured. All of the functionality of these codes is documented here and the commented, electronic versions of this software can also be found online at:

http://users.ece.gatech.edu/~psteffes/palpapers/hanley_data/software

B.1 Data Retrieval

There are four types of Matlab® codes that are used for these experiments. The first type does not directly factor into measuring the opacity or refractivity of a gas mixture, but is necessary for ensuring equal mixing and thermal stabilization. These Q-tracking scripts are used to monitor both the center frequency and Q of multiple resonances in each

resonator. A code named *Qtrack_bigres.m* is used for the large cylindrical cavity resonator, while *Qtrack_smallres.m* and *Qtrack_ka* are used for the small cylindrical cavity and Fabry-Perot resonators respectively. These codes are designed to be used immediately following the admission of gas(es) into the resonators. The quality factor data is best used for determining the concentration and mixing of the gases, while the center frequency data also provides information on the temperature stability of the system.

After the gas mixture has stabilized and is ready for characterization, two other codes are executed to retrieve the measurement data: *findandgetdata_NA.m* for measurements in the large cavity resonator below 8.5 GHz and *findandgetdata_Slow.m* for all measurements above 8.5 GHz. The goal of each of these codes is to locate the exact center frequencies of the resonances and to do perform a number of measurements or sweeps of each resonance. The measurement frequency span is set to twice the approximate, quickly measured, half-power bandwidth of each resonance as calculated by *quickprocess_sync.m* for measurements using the spectrum analyzer and three times the half-power bandwidth for measurements using the network analyzer, calculated by *quickprocessNA.m*. The user chooses a file name extension for the type of data to be measured, typically "*vacX*" for the *X*-numbered vacuum measurement or "*mol_Xbars*" where mol is the type of microwave-absorbing molecule and X is the target pressure of the experiment. The measurement codes run an iterated loop through the resonances to be measured, each resonance being assigned a number. The string of the file name extension is then appended to the number of that resonance and the data for each resonance along with the instrumental configurations are saved under that file name. The

user is prompted to enter the exact pressure (P) and temperature (T) readings at the beginning and end of the measurement of each resonance, although this can be changed to prompt less frequently in the case of faster measurements where the P and T values do not measurably change.

The *findandgetdata_NA.m* code contains the vacuum center frequencies (at 295 K) of each of the resonances to be measured. Since the $TE_{(0,1,1)}$, $TE_{(0,1,2)}$, and $TE_{(0,1,3)}$ modes in the large cylindrical cavity resonator are easy to locate and have amplitudes well above nearby spectral features, the network analyzer quickly measures the peaks of these resonances and calculates the proportional amount of frequency shift from vacuum at room temperature in that resonator. This shift is a result both of the expansion or contraction of the resonator when operating at a different temperature and the refractivity of the gas(es) inside it. The frequency shift is used to calculate the new center frequency of each resonance and zoom in to the correct span without the assistance of the user. In cases where there are several nearly spaced resonances, the user can input the number of the resonance in the code and be prompted to manually identify the correct resonance to be measured. The *findandgetdata_NA.m* code takes measurements of all four scattering parameters at the zoomed-in span and at a span of 50 MHz, the latter used to identify any nearby corrupting resonances.

The *findandgetdata_Slow.m* code utilizes the synchronization of the swept signal generator with the spectrum analyzer to locate and zoom in to the resonances of the small cavity and Fabry-Perot resonators. The values of the center frequencies of these resonances are stored in an external file (*ResList.mat*) along with the large spans, nominal zoomed-in spans, signal generator power levels and resolution bandwidths to be used for

each resonance. The resonances in the small cylindrical cavity resonator cannot be measured as quickly as those in the large resonator and therefore, the frequency shift factor is typically calculated manually and incorporated into the code for each experiment. The *findandgetdata_Slow.m* code measures both the zoomed-out and zoomed-in spectra of each resonance.

After all the spectral data on the gas mixtures have been taken for a string of experiments, the dielectrically matched measurements must be performed. These involve adding lossless gas to the resonators to cause the same frequency shift as the test gases. Since the refractivity of each test gas is rarely constant across the entire frequency range of all the resonances, slightly different amounts of lossless matching gas must be added for the measurement of each resonance. This requires the ability to control the amount of gas in the system to within 0.5 mbar of pressure. To calculate the center frequency of each resonance when loaded with the test gas, the main resonance processing codes *NAprocess.m*, *resprocessSA.m* and *resprocessSAsync.m* are used. These codes will be described in greater detail in the next section. The functionality of the dielectric matching codes for each resonator are practically identical, with the added ability to more accurately track resonances with the network analyzer due to its greater resolution. Once the target frequencies to which each resonance must be shifted are calculated, the code configures the measurement instruments under the same conditions as the test gas (center frequency, span, power, etc.) and places a marker at that frequency, displaying a wider span, and prompting the user to add or remove the appropriate amount of gas to shift the resonance close to its target frequency. Once this has been performed, the user allows the program to further zoom in to the correct span and assess the closeness of the resonance

center frequency to its target. A series of audible tones is used to assist the user in the event that he or she cannot see the computer screen and instrument screens while opening and closing the valves of the gas-handling system. This approach involves generating either one or two short-duration "beeps" to notify the user if they need to add or remove gas respectively followed by a higher-pitch tone indicating the closeness of the resonance to its target frequency. Once the resonance center frequency is within the tolerable range of the target ($1/300^{th}$ of the span for the network analyzer and $1/150^{th}$ of the span for the spectrum analyzer) a distinctive tone is generated to alert the user.

Quickly adding or removing gas from the system slightly shifts the temperature of the system due to the heat of expansion of the gas. In the case of the network analyzer, the target tone must be generated three times before the dielectric matching measurement is started to allow for the resonance to stabilize. The dielectric matching code for the spectrum analyzer only requires one confirmation tone since its sweep times are longer. Due to time constraints, the center frequencies of the resonances measured by the spectrum analyzer are compared to their values taken using the synchronized mode. This allows the user much faster confirmation that the resonance has been shifted to the correct position. The 40-second-long sweeps that make up the more accurate data of the test gas measurements are used for comparison after one 40-second-long sweep of the dielectric matching gas has been completed and after all of the sweeps of the dielectric matching gas have been completed. If at any time, the center frequency of the dielectric matched measurement falls outside of the target range, the user is prompted to rectify the situation by adding or removing additional gas and the measurement is restarted.

Once the resonance has been shifted to the correct frequency, the user is prompted to enter the temperature ($T1$) and pressure ($P1$) of the matching gas before starting the measurement of that resonance. After the resonance has been measured, the user enters the final temperature ($T2$) and pressure ($P2$) of the matching gas. The software confirms that the newly measured dielectrically-matched resonance has a center frequency value within the specified tolerance, and if it does not, the program restarts, prompting the user to add or remove gas. The dielectric matching code for the network analyzer is designated *ARmatch.m* and for the spectrum analyzer, *ARmatch_sync.m*, with the only inputs being the file name extension and resonance numbers to be measured.

The last step in retrieving data for an experiment, after the final vacuum measurement has been completed, is to measure the transmissivity of the cables used for each resonator at all the resonant frequencies. The user specifies the names of the files where the test gas data resides and the code iterates through the files reading the pertinent states (center frequency, span, power, etc.) of the instruments from each measurement and configuring the instruments identically. In the case of the swept signal generator, the device's maximum amount of leveled output power is used during the test gas measurements to optimize the S/N at the spectrum analyzer. This same level of power would saturate the spectrum analyzer's detector when the insertion loss of the resonator is not included. Therefore the power level used in the transmissivities on the signal generator is set to –10dBm, the maximum detectable power at the spectrum analyzer. The transmissivity code for the spectrum analyzer measurements, *findandgettransSmallRes.m* or *findandgettranska.m*, then adds back the difference in original output power from –10dBm to give the transmissivity values of the cables under

the appropriate conditions. This does add some additional uncertainty, which is discussed in section 3.4.1. The transmissivity code for the network analyzer is named *findandgettransNA.m*. The transmissivity measurements are typically repeated three times with the user specifying the number of the transmissivity measurement, which is added to the file name where the transmissivity data is stored.

B.2 Data Processing

A completely measured set of data for each resonance at each pressure/temperature consists of 8 files, three vacuum measurements, three transmissivity measurements, a test gas measurement and a dielectrically matched measurement. From these files, the opacity and refractivity of the measured gas mixture at that resonant frequency can be calculated. A script is typically written to calculate these values for all the resonances of a particular experiment for a given resonator. The script uses the resonant mode numbers of each resonance (for the cavity resonators) along with the file name extensions as inputs to the calculation code *Acalc.m*. Other inputs that must be specified are the type of instrument used for the measurements, the configuration of the resonator (described in section 3.4.2), and for network analyzer measurements, whether to use S(2,1) or S(1,2) in the calculations. The ability to utilize synchronized measurements from the spectrum analyzer is also included, but rarely used.

The *Acalc.m* code relies on several other codes to calculate the overall opacity and refractivity for each resonance. Firstly, the test-gas measurement sweeps are smoothed with the cubic spline described in section 3.2.3. In the case of unsynchronized spectrum analyzer measurements the sweep-on-span nulls are also corrected in the *resprocessSA.m*

code. The network analyzer measurements are smoothed using the *NAprocess.m* code and synchronized spectrum analyzer measurements with the *resprocessSAsync.m* code. Each of these codes returns the mean values of Q, center frequency, bandwidth, asymmetry and amplitude from all the sweeps for each resonance along with their respective standard deviations. Additionally, Q values calculated using the bandwidths of equations 3.44 and 3.45 are returned. These three codes also have the built-in capability of processing a resonance to deconvolve the effect of any frequency slope due to cable transmissivity. They require as an input the value of the transmissivity across the measurement span as generated by *transdeconvolve.m*, which further relies on the smoothing of the transmissivity measurements by *transmoothNA.m*, *transmooth.m* or *transmoothsync.m* for the network analyzer, unsynchronized spectrum analyzer and synchronized spectrum analyzer respectively. The amplitudes of the transmissivity values used in equation 3.17 for calculating opacity, which is implemented in *Acalc.m*, are generated by *trancalNA.m*, *trancal.m* or *trancalsync.m*. The calculations of Err_{inst} are performed by *insterror.m* which is also called in the execution of *Acalc.m*. All other uncertainty calculations for both refractivity and opacity are calculated in *Acalc.m*, with the exception of the uncertainty due to asymmetry which is performed in the script that calls *Acalc.m*. This script is typically named *OpacityPlot_NA.m* for network analyzer measurements of the large cavity resonator, *OpacityPlot_smallres.m* for spectrum analyzer measurements of the small cavity resonator, or *OpacityPlot_ka.m* for measurements of the Fabry-Perot resonator. These codes calculate the measurement temperatures, pressures, center frequencies, opacities, and refractivities along with all

their respective uncertainties and save them in a file for later use in data fitting or comparing to various models.

References

Anders, E. and N. Grevesse (1989), Abundances of the elements: meteoritic and solar, *Geochimica et Cosmochimica Acta*, *53*, 197-214.

Anderson, P. W. (1949), Pressure broadening in the microwave and infra-red regions, *Physical Review*, *76*, 647-661.

Anderson, P. W. (1950), Pressure broadening of the ammonia inversion line by foreign gases: quadrupole-induced dipole interactions, *Physical Review*, *80*, 511-513.

Atreya, S. K., P. R. Mahaffy, H. B. Niemann, M. H. Wong and T. C. Owen (2003), Composition and origin of the atmosphere of Jupiter - an update, and implications for the extrasolar giant planets, *Planetary and Space Science*, *51*, 105-112.

Baldacchini, G., G. Buffa, F. D'Amato, O. Tarrini, M. De Rosa and F. Pelagalli (2000), New results for the temperature dependence of self-broadening and shift in the v_2 ammonia band, *Journal of Quantitative Spectroscopy and Radiative Transfer*, *67*, 365-374.

Baranger, M. (1958), General impact theory of pressure broadening, *Physical Review*, *112*, 855-865.

Becker, G. E. and S. H. Autler (1946), Water vapor absorption of electromagnetic radiation in the centimeter wave-length range, *Physical Review*, *70*, 300-307.

Ben-Reuven, A. (1966), Impact broadening of microwave spectra, *Physical Review*, *145*, 7-22.

Berge, G. L. and S. Gulkis (1976), Earth-based radio observations of Jupiter: millimeter to meter wavelengths, in *Jupiter*, edited by T. Gehrels, pp. 621-692, Univ. of Arizona Press, Tucson.

Birnbaum, G. (1950), A recording microwave refractometer, *Review of Scientific Instruments*, *21*, 169-176.

Birnbaum, G. and A. A. Maryott (1953), Absorption in the low-frequency wing of the NH_3 inversion spectrum, *The Journal of Chemical Physics*, *21*, 1774-1777.

Birnbaum, G. (1966), Theory of microwave nonresonant absorption and relaxation in gases, *Physical Review*, *150*, 101-109.

Bleaney, B. and R. P. Penrose (1946a), Ammonia spectrum in the 1 cm. wave-length region, *Nature*, *157*, 339-340.

Bleaney, B. and R. P. Penrose (1946b), The inversion spectrum of ammonia, *Physical Review*, *70*, 775-776.

Bleaney, B., J. H. N. Loubser and R. P. Penrose (1947), Cavity resonators for measurements with centimetre electromagnetic waves, *Proceedings of the Physical Society*, *59*, 185-199.

Bleaney, B. and R. P. Penrose (1947), The inversion spectrum of ammonia at centimetre wave-lengths, *Proceedings of the Royal Society of London, Series A: Mathematical and Physical Sciences*, *189*, 358-371.

Bleaney, B. and R. P. Penrose (1948), Collision broadening of the inversion spectrum of ammonia: III. The collision cross-sections for self-broadening and for mixtures with non-polar gases, *Proceedings of the Physical Society*, *60*, 540-549.

Bleaney, B. and J. H. N. Loubser (1950), The inversion spectra of NH_3, CH_3Cl and CH_3Br at high pressures, *Proceedings of the Physical Society: Section A*, *63*, 483-493.

Borysow, J., L. Trafton, L. Frommhold and G. Birnbaum (1985), Modeling of pressure-induced far-infrared absorption spectra: molecular hydrogen pairs, *The Astrophysical Journal*, *296*, 644-654.

Buffa, G., M. Martinelli, O. Tarrini and C. Umeton (1979), Ammonia inversion spectrum: detailed measurements and theoretical calculations of pressure shift, *Journal of Physics B (Atomic and Molecular Physics)*, *12*, 743-753.

Burke, B. F. and K. L. Franklin (1955), Observations of a variable radio source associated with the planet Jupiter, *Journal of Geophysical Research*, *60*, 213-217.

Bussey, H. E. and G. Birnbaum (1959), Cavity resonators for dielectric spectroscopy of compressed gases, *The Review of Scientific Instruments*, *30*, 800-804.

Butler, R. P., J. T. Wright, G. W. Marcy, D. A. Fischer, S. S. Vogt, C. G. Tinney, H. R. A. Jones, B. D. Carter, J. A. Johnson, C. McCarthy and A. J. Penny (2006), Catalog of nearby exoplanets, *The Astrophysical Journal*, *646*, 505-522.

Chen, P., J. C. Pearson, H. M. Pickett, S. Matsuura and G. A. Blake (2006), Measurements of $^{14}NH_3$ in the v_2=1 state by a solid-state, photomixing, THz spectrometer, and a simultaneous analysis of the microwave, terahertz, and infrared transitions between the ground and v_2 inversion-rotation levels, *Journal of Molecular Spectroscopy*, *236*, 116-126.

Chu, F. Y. and S. M. Freund (1973), Millimeterwave rotation-inversion transition of $^{14}NH_3$ and $^{15}NH_3$ in the v_2-state, *Journal of Molecular Spectroscopy*, *48*, 183-184.

Cleeton, C. E. and N. H. Williams (1934), Electromagnetic waves of 1.1 cm. wave-length and the absorption spectrum of ammonia, *Physical Review*, *45*, 234-237.

Crain, C. M. (1948), The dielectric constant of several gases at a wave-length of 3.2 centimeters, *Physical Review*, *74*, 691-693.

de Boor, C. (2001), *A Practical Guide to Splines*, Revised ed., Springer-Verlag, New York.

de Pater, I. and S. T. Massie (1985), Models of the millimeter-centimeter spectra of the giant planets, *Icarus*, *62*, 143-171.

de Pater, I., D. R. DeBoer, M. Marley, R. Freedman and R. Young (2005), Retrieval of water in Jupiter's deep atmosphere using microwave spectra of its brightness temperature, *Icarus*, *173*, 425–438.

DeBoer, D. R. and P. G. Steffes (1994), Laboratory measurements of the microwave properties of H_2S under simulated Jovian conditions with an application to Neptune, *Icarus*, *109*, 352-366.

DeBoer, D. R. (1995), The microwave opacity of H_2S with application to the tropospheric vertical structure of the Jovian planets, Ph.D. thesis, Georgia Institute of Technology, Atlanta.

DeBoer, D. R. and P. G. Steffes (1996), The Georgia Tech high sensitivity microwave measurement system, *Astrophysics and Space Science*, *236*, 111-124.

Debye, P. (1929), *Polar Molecules.*, 172 pp., The Chemical Catalog Company, Inc., New York.

Dennison, D. M. and G. E. Uhlenbeck (1932), The two-minima problem and the ammonia molecule, *Physical Review*, *41*, 313-321.

Devaraj, K. and P. G. Steffes (2007), Preliminary results for the 2-4 millimeter wavelength continuum opacity of ammonia based on new laboratory measurements under simulated Jovian conditions, *Bulletin of the American Astronomical Society*, *39*(3), 447.

Dicke, R. H., R. Beringer, R. L. Kyhl and A. B. Vane (1946), Atmospheric absorption measurements with a microwave radiometer, *Physical Review*, *70*, 340-348.

Dutta, J. M., C. R. Jones, T. M. Goyette and F. C. De Lucia (1993), The hydrogen and helium pressure broadening at planetary temperatures of the 183 and 380 GHz transitions of water vapor, *Icarus*, *102*, 232-239.

Ertl, G. (1983), Primary steps in catalytic synthesis of ammonia, *Journal of Vacuum Science & Technology A (Vacuum, Surfaces, and Films)*, *1*, 1247-1253.

Essen, L. (1953), The refractive indices of water vapour, air, oxygen, nitrogen, hydrogen, deuterium and helium, *Proceedings of the Physical Society B*, *66*, 189-193.

Fano, U. (1981), Unified treatment of collisions, *Physical Review A*, *24*, 2402-2415.

Folkner, W. M., R. Woo and S. Nandi (1998), Ammonia abundance in Jupiter's atmosphere derived from the attenuation of the Galileo probe's radio signal, *Journal of Geophysical Research*, *103*, 22,847-822,855.

Frenkel, L. and D. Woods (1966), The microwave absorption by H_2O vapor and its mixtures with other gases between 100 and 300 Gc/s, *Proceedings of the IEEE*, *54*, 498-505.

Fröhlich, H. (1946), Shape of collisional-broadened spectral lines, *Nature*, *157*, 478.

Gaut, N. E. and E. C. Reifenstein, III (1971), Interaction model of microwave energy and atmospheric variables, Huntsville: NASA, Contract nr NAS8-26275, 232 pp, Available from: NASA Technical Report Server, NASA-CR-61348.

Godon, M. and A. Bauer (1988), Helium-broadened widths of the 183 and 380 GHz lines of water vapor, *Chemical Physics Letters*, *147*, 189-191.

Golubiatnikov, G. Y. (2005), Shifting and broadening parameters of the water vapor 183-GHz line (3_{13}–2_{20}) by H_2O, O_2, N_2, CO_2, H_2, He, Ne, Ar, and Kr at room temperature, *Journal of Molecular Spectroscopy*, *230*, 196–198.

Good, W. E. (1946a), The inversion spectrum of ammonia, *Physical Review*, *69*, 539.

Good, W. E. (1946b), The inversion spectrum of ammonia, *Physical Review*, *70*, 213-218.

Goodman, G. C. (1969), Models of Jupiter's atmosphere, Ph.D. thesis, University of Illinois, Urbana.

Goyette, T. M. and F. C. De Lucia (1990), The pressure broadening of the $3_{1,3}$-$2_{2,0}$ transition of water between 80 and 600 K, *Journal of Molecular Spectroscopy*, *143*, 346-358.

Grevesse, N., M. Asplund and A. J. Sauval (2005), The new solar chemical composition, in *Element Stratification in Stars: 40 Years of Atomic Diffusion*, edited by G. Alecian*, et al.*, pp. 21-30, EDP Sciences.

Gross, E. P. (1955), Shape of collision-broadened spectral lines, *Physical Review*, *97*, 395-403.

Hanley, T. R. and P. G. Steffes (2005), Laboratory measurements of the microwave opacity of hydrochloric acid vapor in a carbon dioxide atmosphere, *Icarus*, *177*, 286-290.

Hanley, T. R. and P. G. Steffes (2007), A high-sensitivity laboratory system for measuring the microwave properties of gases under simulated conditions for planetary atmospheres, *Radio Science*, *42*, RS6010.

Herbauts, I. M. and D. J. Dunstan (2007), Quantum molecular dynamics study of the pressure dependence of the ammonia inversion transition, *Physical Review A*, *76*, 062506.

Hewitt, P. L. (1977), Width and shift measurements in the microwave spectra of NH_3, CH_3Cl and OCS, *Journal of Quantitative Spectroscopy and Radiative Transfer*, *17*, 227-232.

Hewlett-Packard (1997), *HP 8560 E-Series Spectrum Analyzer User's Guide*, Hewlett-Packard Company.

Hill, R. J. (1986), Water vapor-absorption line shape comparison using the 22-GHz line: The Van Vleck-Weisskopf shape affirmed, *Radio Science*, *21*, 447-451.

Ho, W., I. A. Kaufman and P. Thaddeus (1966), Laboratory measurements of microwave absorption in models of the atmosphere of Venus, *Journal of Geophysical Research*, *71*, 5091-5108.

Hoffman, J. P., P. G. Steffes and D. R. DeBoer (2001), Laboratory measurements of the microwave opacity of phosphine: opacity formalism and application to the atmospheres of the outer planets, *Icarus*, *152*, 172-184.

Janssen, M. A., M. D. Hofstadter, S. Gulkis, A. P. Ingersoll, M. Allison, S. J. Bolton, S. M. Levin and L. W. Kamp (2005), Microwave remote sensing of Jupiter's atmosphere from an orbiting spacecraft, *Icarus*, *173*, 447-453.

Johnson, R. H. and M. W. P. Strandberg (1952), Broadening of microwave absorption lines by collisions with the cell walls, *Physical Review*, *86*, 811-812.

Joiner, J., P. G. Steffes and J. M. Jenkins (1989), Laboratory measurements of the 7.5-9.38-mm absorption of gaseous ammonia (NH_3) under simulated Jovian conditions, *Icarus*, *81*, 386-395.

Joiner, J. (1991), Millimeter-wave spectra of the Jovian planets, Ph.D. thesis, Georgia Institute of Technology, Atlanta.

Joiner, J. and P. G. Steffes (1991), Modeling of Jupiter's millimeter wave emission utilizing laboratory measurements of ammonia (NH_3) opacity, *Journal of Geophysical Research*, *96*, 17463-17470.

Karpowicz, B. M., P. G. Steffes and J. P. Hoffman (2007), A view of outer planet composition from orbiting spacecraft via microwave emission: results from a new hybrid ray-tracing radiative transfer model, *Bulletin of the American Astronomical Society*, *39*(3), 414.

Karpowicz, B. M. and P. G. Steffes (2008), From modeling to laboratory measurements: simulated microwave radiometer sensitivity to water vapor abundance and a new high pressure system to measure water vapor under Jovian conditions, *Proceedings of the 2008 URSI National Radio Science Meeting*, p12.

King, W. C. and W. Gordy (1954), One-to-two millimeter wave spectroscopy. IV. Experimental methods and results for OCS, CH_3F and H_2O, *Physical Review*, *93*, 407-412.

Kolodner, M. A. and P. G. Steffes (1998), The microwave absorption and abundance of sulfuric acid vapor in the Venus atmosphere based on new laboratory measurements, *Icarus*, *132*, 151-169.

Kumar, M. J., N. D. Kataria and G. P. Srivastava (1994), 10 GHz cylindrical cavity resonator for characterization of surface resistance of High T_c superconducting bulk and thin films, *IEEE Transactions on Magnetics*, *30*, 4605-4607.

Kunde, V., R. Hanel, W. Maguire, D. Gautier, J. P. Baluteau, A. Marten, A. Chedin, N. Husson and N. Scott (1982), The tropospheric gas composition of Jupiter's north equatorial belt (NH_3, PH_3, CH_3D, GeH_4, H_2O) and the Jovian D/H isotopic ratio, *The Astrophysical Journal*, *263*, 443-467.

Kyhl, R. L., R. H. Dicke and R. Beringer (1946), The absorption of 1-cm electromagnetic waves by atmospheric water vapor, *Physical Review*, *69*, 694.

Larson, H. P., U. Fink, R. Treffers and T. N. Gautier, III (1975), Detection of water vapor on Jupiter, *The Astrophysical Journal*, *197*, L137-140.

Law, S. E. and D. H. Staelin (1968), Measurements of Venus and Jupiter near 1-cm wavelength, *The Astrophysical Journal*, *154*, 1077-1086.

Legan, R. L., J. A. Roberts, E. A. Rinehart and C. C. Lin (1965), Linewidths of the microwave inversion spectrum of ammonia, *The Journal of Chemical Physics*, *43*(12), 4337-4345.

Lichtenstein, M., V. E. Derr and J. J. Gallagher (1966), Millimeter wave rotational transitions and the Stark effect of the water molecule, *Journal of Molecular Spectroscopy*, *20*, 391-401.

Liebe, H. J. and T. A. Dillon (1969), Accurate foreign-gas-broadening parameters of the 22-GHz H_2O line from refraction spectroscopy, *The Journal of Chemical Physics*, *50*, 727-732.

Lorentz, H. A. (1906), The absoption and emission lines of gaseous bodies, *Proceedings of the Royal Netherlands Academy of Arts and Sciences*, *8*, 591-611.

Lorentz, H. A. (1915), The width of spectral lines, *Proceedings of the Royal Netherlands Academy of Arts and Sciences*, *18*, 134-150.

Margenau, H. (1951), Statistical theory of pressure broadening, *Physical Review*, *82*, 156-158.

Matthaei, G. L., L. Young and E. Jones (1980), *Microwave Filters, Impedance Matching Networks and Coupling Structures*, McGraw-Hill, New York.

Mayer, C. H., T. P. McCullough and R. M. Sloanaker (1958), Measurements of planetary radiation at centimeter wavelengths, *Proceedings of the Institute of Radio Engineers*, *46*, 260-266.

McMahon, D. R. A. and I. L. McLaughlin (1974), On the classical microwave and infrared pressure broadening theory for ammonia, *The Journal of Chemical Physics*, *60*, 1966-1975.

Mizushima, M. (1951), The theory of pressure broadening and its application to microwave spectra, *Physical Review*, *83*, 94-103.

Mohammed, P. N. and P. G. Steffes (2003), Laboratory measurements of the Ka-band (7.5 to 9.2 mm) opacity of phosphine (PH_3) and ammonia (NH_3) under simulated conditions for the Cassini-Saturn encounter, *Icarus*, *166*, 425-435.

Mohammed, P. N. and P. G. Steffes (2004), Laboratory measurements of the W band (3.2 mm) properties of phosphine (PH_3) and ammonia (NH_3) under simulated conditions for the outer planets, *Journal of Geophysical Research*, *109*, E07S13.

Mohammed, P. N. (2005), Laboratory measurements of the millimeter wavelength opacity of phosphine (PH_3) and ammonia (NH_3) under simulated conditions for the Cassini-Saturn encounter, Ph.D. thesis, Georgia Institute of Technology, Atlanta.

Morris, E. C. and R. W. Parsons (1970), Microwave absorption by gas mixtures at pressures up to several hundred bars. I. Experimental technique and results, *Australian Journal of Physics*, *23*, 335-349.

Morris, E. C. (1971), Microwave absorption by gas mixtures at pressures up to several hundred bars. II. Discussion of results, *Australian Journal of Physics*, *24*, 157-175.

Murphy, J. S. and J. E. Boggs (1967), Collision broadening of rotational absorption lines. I. Theoretical formulation, *The Journal of Chemical Physics*, *47*, 691-702.

Nethercot, A. H., J. A. Klein, J. H. N. Loubser and C. H. Townes (1952), Spectroscopy near the boundary between the microwave and infrared regions, *Nuovo Cimento*, *9*, 358-363.

Newell, A. C. and R. C. Baird (1965), Absolute determination of refractive indices of gases at 47.7 gigahertz, *Journal of Applied Physics*, *36*, 3751-3759.

Niemann, H. B., S. K. Atreya, G. R. Carignan, T. M. Donahue, J. A. Haberman, D. N. Harpold, R. E. Hartle, D. M. Hunten, W. T. Kasprzak, P. R. Mahaffy, T. C. Owen, N. W. Spencer and S. H. Way (1996), The Galileo probe mass spectrometer: composition of Jupiter's atmosphere, *Science*, *272*, 846-849.

Nouri, S., J. Orphal, H. Aroui and J.-M. Hartmann (2004), Temperature dependence of pressure broadening of NH_3 perturbed by H_2 and N_2, *Journal of Molecular Spectroscopy*, *227*, 60-66.

Orton, G. S., M. Gustafsson, M. Burgdorf and V. Meadows (2007), Revised ab initio models for H_2-H_2 collision-induced absorption at low temperatures, *Icarus*, *189*, 544-549.

Pearson, J. C., T. Anderson, E. Herbst, F. C. De Lucia and P. Helminger (1991), Millimeter- and submillimeter-wave spectrum of highly excited states of water, *The Astrophysical Journal*, *379*, L41-L43.

Pickett, H. M., R. L. Poynter, E. A. Cohen, M. L. Delitsky, J. C. Pearson and H. S. P. Müller (1998), Submillimeter, millimeter, and microwave spectral line catalog, *Journal of Quantitative Spectroscopy & Radiative Transfer*, *60*, 883-890.

Pickett, H. M., J. C. Pearson and C. E. Miller (2005), Use of Euler series to fit spectra with application to water, *Journal of Molecular Spectroscopy*, *233*, 174-179.

Potter, C. A., A. V. Bushkovitch and A. G. Rouse (1951), Pressure broadening in the microwave spectrum of ammonia, *Physical Review*, *83*, 987-989.

Poynter, R. L. and R. K. Kakar (1975), The microwave frequencies, line parameters, and spectral constants for 14NH3, *The Astrophysical Journal Supplement Series*, *29*, 87-96.

Pozar, D. M. (1998), *Microwave Engineering*, 2nd ed., 716 pp., John Wiley & Sons, Inc., New York.

Ramo, S., J. R. Whinnery and T. Van Duzer (1994), *Fields and Waves in Communication Electronics*, 3rd ed., 844 pp., John Wiley & Sons, Inc., New York.

Redlich, O. and J. N. S. Kwong (1949), On the thermodynamics of solutions. V An equation of state. Fugacities of gaseous solutions, *Chemical Reviews*, *44*, 233-244.

Rodrigues, C. C. and D. Moraes, Jr. (2002), Control of the emission of ammonia through adsorption in a fixed bed of activated carbon, *Adsorption Science & Technology*, *20*, 1013-1022.

Rusk, J. R. (1965), Line-breadth study of the 1.64-mm absorption in water vapor, *The Journal of Chemical Physics*, *42*, 493-500.

Scott, M. M., G. L. Wilson and J. A. Berrie (2005), Kramers-Kronig analysis of RF polymers and composites, *IEEE Antennas and Propagation Magazine*, *47*, 156-163.

Seiff, A., D. B. Kirk, T. C. D. Knight, R. E. Young, J. D. Mihalov, L. A. Young, F. S. Milos, G. Schubert, R. C. Blanchard and D. Atkinson (1998), Thermal structure of Jupiter's atmosphere near the edge of a 5-μm hot spot in the north equatorial belt, *Journal of Geophysical Research*, *103*, 22,857-822,889.

Shimizu, F. (1969), Dipole moment of NH_3 in the v_2 excited state, *The Journal of Chemical Physics*, *51*, 2754-2755.

Showman, A. P. and A. P. Ingersoll (1998), Interpretation of Galileo probe data and implications for Jupiter's dry downdrafts, *Icarus*, *132*, 205-220.

Smith, W. V. and R. Howard (1950), Microwave collision diameters II. Theory and correlation with molecular quadrupole moments, *Physical Review*, *79*, 132-136.

Spilker, T. R. (1990), Laboratory measurements of the microwave absorptivity and refractivity spectra of gas mixtures applicable to giant planet atmospheres, Ph.D. thesis, Stanford University, CA.

Spilker, T. R. (1993), New laboratory measurements on ammonia's inversion spectrum, with implications for planetary atmospheres, *Journal of Geophysical Research*, *98*, 5539-5548.

Steffes, P. G. and V. R. Eshleman (1981), Laboratory measurements of the microwave opacity of sulfur dioxide and other cloud-related gases under simulated conditions for the middle atmosphere of Venus, *Icarus*, *48*, 180-187.

Steffes, P. G. and J. M. Jenkins (1987), Laboratory measurements of the microwave opacity of gaseous ammonia (NH_3) under simulated conditions for the Jovian atmosphere, *Icarus*, *72*, 35-47.

Story, I. C., V. I. Metchnik and R. W. Parsons (1971), The measurement of the widths and pressure-induced shifts of microwave spectra lines, *Journal of Physics B (Atomic and Molecular Physics)*, *4*, 593-608.

Student (1908), The probable error of a mean, *Biometrika*, *6*, 1-25.

Townes, C. H. and F. R. Merritt (1946), Water spectrum near one-centimeter wave-length, *Physical Review*, *70*, 558-559.

Townes, C. H. and A. L. Schawlow (1955), *Microwave Spectroscopy*, Dover Publications Inc, New York.

Trafton, L. (1973), On the He-H_2 thermal opacity in planetary atmospheres, *The Astrophysical Journal*, *179*, 971-976.

Tsao, C. J. and B. Curnutte (1962), Line-widths of pressure-broadened spectral lines, *Journal of Quantitative Spectroscopy and Radiative Transfer*, *2*, 41-91.

Tyler, G. L. and H. T. Howard (1969), Refractivity of carbon dioxide under simulated Martian conditions, *Radio Science*, *4*, 899-904.

Ulaby, F. T., R. K. Moore and A. K. Fung (1981), *Microwave Remote Sensing: Active and Passive. Volume 1: Microwave Remote Sensing Fundamentals and Radiometry*, 456 pp., Addison-Wesley, Reading, MA.

Van Vleck, J. H. and V. F. Weisskopf (1945), On the shape of collision-broadened lines, *Reviews of Modern Physics*, *17*, 227-236.

Van Vleck, J. H. (1947), Absorption of microwaves by uncondensed water vapor, *Physical Review*, *71*, 425-433.

Van Vleck, J. H. and H. Margenau (1949), Collision theories of pressure broadening of spectral lines, *Physical Review*, *76*, 1211-1214.

von Zahn, U., D. M. Hunten and G. Lehmacher (1998), Helium in Jupiter's atmosphere: results from the Galileo probe Helium Interferometer Experiment, *Journal of Geophysical Research*, *103*, 22,815-822,829.

Waters, J. W. (1976), Absorption and emission by atmospheric gases, in *Astrophysics*, edited by M. L. Meeks, Academic Press, New York.

Wildt, R. (1932), Absorption spectra and atmospheres of the major planets, *Nachrichten von der Koniglicher Gesellschaft der Wissenschaften zu Göttingen*, *II, Math. Physik. Kl.*, 87.

Woolfson, M. M. (1960), Origin of the solar system, *Nature*, *187*, 47-48.

Wrixon, G. T., W. J. Welch and D. D. Thornton (1971), The spectrum of Jupiter at millimeter wavelengths, *The Astrophysical Journal*, *169*, 171-183.

Young, D. M. and A. D. Crowell (1962), *Physical Adsorption of Gases*, 426 pp., Butterworths, Washington.

Young, W. C. and R. G. Budynas (2002), *Roark's formulas for stress and strain*, 7th ed., 852 pp., McGraw-Hill, New York.

VITA

Thomas Ryan Hanley was born in August of 1981 in Milwaukee, Wisconsin. He was raised in Wauwatosa, WI and attended Marquette University High School. He graduated *cum laude* from the University of Notre Dame in May 2003 with a Bachelor's Degree in Electrical Engineering. While enrolled at Notre Dame, he was inducted into Eta Kappa Nu and met his fiancée Casey Korecki. In August of 2003, he enrolled at the Georgia Institute of Technology and earned a Master's Degree in Electrical and Computer Engineering in May 2005, followed by a doctorate in August 2008.

As a Ph.D. student of Dr. Paul Steffes, he studied the microwave properties of various gases in support of planetary atmospheres research through remote sensing. His dissertation focused on the properties of gaseous ammonia and water vapor under simulated conditions of the planet Jupiter in support of the Microwave Radiometer (MWR) as part of the NASA Juno mission. As a graduate student at Georgia Tech, he initiated a program through Eta Kappa Nu of selling discounted electronics lab supplies to undergraduate students. Throughout his tenure at Georgia Tech, this Lab Supplies Project saved students over $35,000 and raised over $25,000 to endow a scholarship for Electrical and Computer Engineering students in financial need. He received the ECE Faculty Award in the spring of 2008 for these efforts.

Thomas Hanley is a junior member of the American Astronomical Society's Division for Planetary Science, IEEE and Eta Kappa Nu. Following the completion of his doctorate, he will be joining the Air Defense Radar Analysis & Phenomenology Group at The Johns Hopkins University Applied Physics Lab in Laurel, MD. He and his fiancée, Casey, plan to be married in July of 2009.